



## NRC Publications Archive Archives des publications du CNRC

### Direct detection of nitrogen-14 in solid-state NMR spectroscopy

O'Dell, Luke A.

This publication could be one of several versions: author's original, accepted manuscript or the publisher's version. / La version de cette publication peut être l'une des suivantes : la version prépublication de l'auteur, la version acceptée du manuscrit ou la version de l'éditeur.

For the publisher's version, please access the DOI link below. / Pour consulter la version de l'éditeur, utilisez le lien DOI ci-dessous.

#### **Publisher's version / Version de l'éditeur:**

<https://doi.org/10.1016/j.pnmrs.2011.04.001>

*Progress in Nuclear Magnetic Resonance Spectroscopy*, 59, 4, pp. 295-318, 2011-04-20

#### **NRC Publications Record / Notice d'Archives des publications de CNRC:**

<https://nrc-publications.canada.ca/eng/view/object/?id=06ab1108-dc29-44b0-9cff-8f143af1bc27>

<https://publications-cnrc.canada.ca/fra/voir/objet/?id=06ab1108-dc29-44b0-9cff-8f143af1bc27>

Access and use of this website and the material on it are subject to the Terms and Conditions set forth at

<https://nrc-publications.canada.ca/eng/copyright>

READ THESE TERMS AND CONDITIONS CAREFULLY BEFORE USING THIS WEBSITE.

L'accès à ce site Web et l'utilisation de son contenu sont assujettis aux conditions présentées dans le site

<https://publications-cnrc.canada.ca/fra/droits>

LISEZ CES CONDITIONS ATTENTIVEMENT AVANT D'UTILISER CE SITE WEB.

**Questions?** Contact the NRC Publications Archive team at

PublicationsArchive-ArchivesPublications@nrc-cnrc.gc.ca. If you wish to email the authors directly, please see the first page of the publication for their contact information.

**Vous avez des questions?** Nous pouvons vous aider. Pour communiquer directement avec un auteur, consultez la première page de la revue dans laquelle son article a été publié afin de trouver ses coordonnées. Si vous n'arrivez pas à les repérer, communiquez avec nous à PublicationsArchive-ArchivesPublications@nrc-cnrc.gc.ca.



# Direct Detection of Nitrogen-14 in Solid-State NMR Spectroscopy

Luke A. O'Dell

Steacie Institute for Molecular Sciences, National Research Council,  
100 Sussex Drive, Ottawa, K1A 0R6, Ontario, Canada

Email: [luke.odell@nrc-cnrc.gc.ca](mailto:luke.odell@nrc-cnrc.gc.ca)

Telephone: 1-613-990-1566

Received: February 10<sup>th</sup> 2011

**Keywords:** Solid-state  $^{14}\text{N}$  NMR, integer spin, first-order quadrupolar interaction, ultra-wideline, magic angle spinning, overtone spectroscopy

## **Contents**

1. Introduction	3
2. Interactions and definitions	5
3. Single-crystal samples	11
4. Stationary powder samples	17
4.1 Symmetric environments	17
4.2 Piecewise acquisition	22
4.3 Fixed frequency techniques	25
4.4 Frequency-swept pulses	28
5. Magic angle spinning	32
5.1 Narrowband excitation	32
5.2 Broadband excitation	36
6. Overtone spectroscopy	40
7. Aligned systems	49
8. Summary	56
References	60

## 1. Introduction

Nitrogen is the seventh most abundant element in our solar system and is of the utmost importance in chemistry, biology and materials science. It is therefore unfortunate that both NMR-active isotopes of nitrogen have rather unfavorable NMR properties (Table 1).  $^{15}\text{N}$  is a spin-1/2 nucleus and thus can be studied with relatively high resolution even in the solid state, but it suffers from a low natural abundance (0.37 %), which translates to a poor sensitivity. While this trait allows for the useful possibility of selective labeling, isotopic enrichment can be difficult and expensive, and there are far fewer  $^{15}\text{N}$  NMR studies reported than for  $^{13}\text{C}$ , which has both a higher natural abundance (1.07 %) and gyromagnetic ratio, making it several orders of magnitude more receptive. While the number of published  $^{15}\text{N}$  NMR papers is disproportionately small relative to the importance of nitrogen, studies utilizing the 99.6 % natural abundance  $^{14}\text{N}$  isotope are even scarcer. The difficulty of  $^{14}\text{N}$  NMR stems from two main factors. First, the nucleus has a very low gyromagnetic ratio ( $\gamma_{\text{N}} = 1.934 \times 10^7 \text{ rad T}^{-1} \text{ s}^{-1}$ ), meaning that it is inherently less sensitive than other nuclei (having a receptivity of 0.001 relative to  $^1\text{H}$ ), and also suffers from equipment-related issues such as acoustic ringing and limited radio frequency (RF) pulse powers. Secondly, and more importantly, it is a spin-1 nucleus, and while its electric quadrupole moment is not particularly large ( $Q = 20.44 \text{ mbarn}$ ), both of its Zeeman transitions experience significant perturbations due to the quadrupolar interaction (see Section 2). This interaction will be present for all but the most spherically-symmetric nitrogen environments, resulting in rapid relaxation in solution and significant heterogeneous broadening of spectral lineshapes in the solid state. Ideally, the quadrupolar nature of  $^{14}\text{N}$

should be considered as an advantage, as it potentially allows the retrieval of structural and dynamic information that could not be accessed with  $^{15}\text{N}$ , but, pragmatically, it is more often a hindrance, prohibiting (or at least making extremely difficult) the use of standard NMR experiments, and reducing the overall sensitivity and spectral resolution.

The combination of the importance of nitrogen and the high natural abundance of  $^{14}\text{N}$  has spurred much effort to develop solid-state NMR techniques that can make use of this isotope in the characterization of materials. Notably, the last few years have seen the establishment of a variety of methods for the indirect detection of  $^{14}\text{N}$  using more amenable nuclei such as  $^1\text{H}$  or  $^{13}\text{C}$ , offering a route to heteronuclear correlation experiments that can provide both structural and dynamic information with a potentially very high resolution. These techniques have recently been reviewed by Cavadini [1]. The purpose of this article is to provide a summary of solid-state NMR techniques that detect the signal *directly* from the  $^{14}\text{N}$  nuclei. A wide range of approaches have been proposed and utilized, with each method offering unique advantages and limitations in terms of the systems that can be studied and the information that can be extracted. The article will concentrate on a qualitative description of the techniques, with the aim of highlighting the numerous, diverse and interesting ways in which the  $^{14}\text{N}$  nucleus can be exploited. In the following section, a minimal amount of theory is presented in order to provide a basic understanding of the effects of the most common NMR interactions on solid-state  $^{14}\text{N}$  spectra.

## 2. Interactions and definitions

Being a spin-1 nucleus,  $^{14}\text{N}$  has three energy levels which are split by the Zeeman interaction in the presence of an external magnetic field  $B_0$ , giving rise to two single-quantum transitions and one double-quantum transition. In the majority of cases, the secular approximation can be applied and the various interactions experienced by the nucleus can be considered as perturbations to the Zeeman transition energies. In such cases, only the single-quantum transitions,  $+1 \leftrightarrow 0$  and  $0 \leftrightarrow -1$ , are observed. Whilst there are situations when this approximation breaks down and the axis of quantization is tilted away from  $B_0$ , a treatment of this has been provided elsewhere (see, for example, references in Section 6), and most of the experiments described in this article may be sufficiently understood using the straightforward perturbation approach. Fig. 1 shows schematically the perturbations caused by the most common interactions experienced by the  $^{14}\text{N}$  nucleus. To further simplify the discussion throughout this article, these perturbations are described as frequencies ( $\nu$ , in units of Hz) rather than energies, allowing for a direct comparison with the spectral features to which they give rise.

The Zeeman splitting results in two single-quantum (or fundamental) transitions whose frequencies are given by:

$$\nu_0 = \frac{\gamma_{\text{N}} B_0}{2\pi} \quad (1)$$

In the absence of other interactions, this frequency is identical for both transitions, and the NMR spectrum will feature a single resonance line at  $\nu_0$  (the Larmor frequency). In most instances, however, an electric field gradient (EFG) will exist at the nitrogen site

and thus the quadrupolar interaction will be present. The  $^{14}\text{N}$  EFG can be described as a traceless, symmetric, second-rank tensor quantity and is conventionally reported using two parameters, the quadrupolar coupling constant  $C_Q$  (in Hz) and the asymmetry parameter  $\eta_Q$  (dimensionless, and ranging between 0 and 1):

$$C_Q = \frac{eQV_{33}}{h}; \quad (2)$$

$$\eta_Q = \frac{V_{11} - V_{22}}{V_{33}}, \quad (3)$$

where  $e$  is the charge of the electron,  $Q$  is the  $^{14}\text{N}$  quadrupole moment,  $h$  is the Planck constant and  $V_{mn}$  are the principal components of the EFG tensor in its diagonalized form, ordered such that  $|V_{33}| \geq |V_{22}| \geq |V_{11}|$ . The orientation of this tensor with respect to  $B_0$  is specified by the polar angles  $\theta$  and  $\varphi$ .

The description of the quadrupolar interaction derived from perturbation theory involves an expansion in terms of increasing order, each of which can be considered separately. While third-order effects can play an important role in indirectly-detected  $^{14}\text{N}$  experiments [1], in most cases only the first- and second-order quadrupolar interactions (FOQI and SOQI) need to be considered. The first-order quadrupolar perturbation to the single-quantum  $^{14}\text{N}$  transition frequencies is given by:

$$\nu_Q^{(1)} = \frac{3}{8} C_Q (3 \cos^2 \theta - 1 + \eta_Q \sin^2 \theta \cos 2\varphi) \quad (4)$$

The FOQI is directly proportional to  $C_Q$ , and is usually the dominant perturbing interaction in solid-state  $^{14}\text{N}$  NMR. The  $C_Q$  is therefore the most important parameter in determining both the nature of the  $^{14}\text{N}$  NMR spectrum and the appropriate acquisition methods. Typical values of  $C_Q$  for  $^{14}\text{N}$  range up to *ca.* 7 MHz, but in most cases fall between 1 and 4 MHz [2] (Fig. 2). From Eq. (4) it can be seen that the largest possible value of  $\nu_Q^{(1)}$  is  $3C_Q/4$ , thus for a powder sample containing every value of  $\theta$  and  $\phi$ , the first-order  $^{14}\text{N}$  resonances will form a powder pattern spanning a range of  $3C_Q/2$ . Since the two fundamental transitions are perturbed by  $\nu_Q^{(1)}$  in opposite directions, such powder patterns are (to first order, and in the absence of chemical shift anisotropy) mirror symmetric about  $\nu_0$ . Example  $^{14}\text{N}$  powder patterns are shown in Fig. 3 for values of  $\eta_Q$  from 0 to 1. Discontinuities are present in the lineshapes at frequencies  $\nu_m$ , and these correspond to crystallite orientations in which the principal EFG axis  $V_m$  is parallel to  $B_0$ . The frequencies of these discontinuities (to first order) are given by:

$$\nu_{11} = \nu_0 \pm \frac{3}{8}C_Q(1 - \eta_Q) \quad (5)$$

$$\nu_{22} = \nu_0 \pm \frac{3}{8}C_Q(1 + \eta_Q) \quad (6)$$

$$\nu_{33} = \nu_0 \pm \frac{3}{4}C_Q. \quad (7)$$

The second-order quadrupolar perturbation  $\nu_Q^{(2)}$  for a spin-1 nucleus is [3]:

$$v_Q^{(2)} = \frac{C_Q^2}{16\nu_0} \left\{ \begin{array}{l} \frac{1}{5}(3 + \eta_Q^2) \\ + \frac{1}{28} [(\eta_Q^2 - 3)(3 \cos^2 \theta - 1) + 6\eta_Q \sin^2 \theta \cos 2\varphi] \\ - \frac{3}{1120} (18 + \eta_Q^2)(35 \cos^4 \theta - 30 \cos^2 \theta + 3) \\ - \frac{9}{56} \eta_Q \sin^2 \theta (7 \cos^2 \theta - 1) \cos 2\varphi \\ - \frac{3}{32} \eta_Q^2 \sin^4 \theta \cos 4\varphi \end{array} \right\} \quad (8)$$

which also varies with EFG orientation but scales inversely with  $B_0$ . At moderate magnetic field strengths  $v_Q^{(2)}$  will be far smaller than  $v_Q^{(1)}$  (on the order of a few kHz when  $C_Q$  is a few MHz). While a perturbation of this size may often be small enough to ignore, some experimental techniques can be used to remove the effects of the FOQI, in which case the SOQI (and other interactions) must then be considered. Unlike the FOQI, the SOQI perturbs both  $^{14}\text{N}$  transitions in the same direction. Thus, the centre of gravity of the powder pattern is shifted to a lower frequency by an amount on the order of kHz (referred to here as the isotropic SOQI shift). This also has the effect of breaking the mirror-symmetry of the first-order powder pattern, as shown in Fig. 4b.

It is worth noting here that  $V_{33}$  can be positive or negative, and therefore  $C_Q$  has an associated sign. However, this sign has no effect on the  $^{14}\text{N}$  NMR spectrum, since  $v_Q^{(1)}$  is proportional to  $C_Q$  but affects both fundamental transitions in an equal and opposite sense, while  $v_Q^{(2)}$  is proportional to  $C_Q^2$ . It is therefore the absolute value of  $C_Q$  that is most commonly determined by  $^{14}\text{N}$  NMR. The sign may be ascertained either *via* its effect on other nuclei that are coupled to  $^{14}\text{N}$  [1], by other experimental techniques

such as nuclear quadrupole resonance, or by computation from the molecular or crystal structure. All subsequent mentions of  $^{14}\text{N } C_Q$  in this article refer to the absolute value.

The chemical shift (CS) can also cause a net perturbation to the frequency of the  $^{14}\text{N}$  transitions. Like the EFG, the symmetric component of this interaction can be described as a second-rank CS tensor with principal components  $\delta_{11} \geq \delta_{22} \geq \delta_{33}$  (the anti-symmetric component, which does not usually affect the NMR spectrum, will not be discussed further here). Unlike the EFG, the trace of the CS tensor can be non-zero, and this interaction therefore has both an isotropic part (usually denoted as  $\delta_{\text{iso}}$ , the isotropic chemical shift, and given in ppm relative to a reference frequency) and an anisotropic part. The perturbation  $\nu_{\text{CS}}$  due to this interaction therefore also has both isotropic and anisotropic components:

$$\nu_{\text{CS}} = \nu_0 \delta_{\text{iso}} + \nu_0 \Delta_{\text{CS}} (3 \cos^2 \alpha - 1 + \eta_{\text{CS}} \sin^2 \alpha \cos 2\beta) \quad (9)$$

where the angles  $\alpha$  and  $\beta$  describe the orientation of the CS tensor with respect to the magnetic field, and  $\delta_{\text{iso}}$ ,  $\Delta_{\text{CS}}$  (the chemical shift anisotropy, or CSA) and  $\eta_{\text{CS}}$  (the chemical shift asymmetry) are defined from the principal components of the CS tensor as follows:

$$\delta_{\text{iso}} = \frac{\delta_{11} + \delta_{22} + \delta_{33}}{3}; \quad (10)$$

$$\Delta_{\text{CS}} = \delta_{33} - \delta_{\text{iso}}; \quad (11)$$

$$\eta_{\text{CS}} = \frac{\delta_{11} - \delta_{22}}{\Delta_{\text{CS}}}. \quad (12)$$

Both the isotropic and anisotropic parts of  $\nu_{CS}$  increase proportionally to  $B_0$ , and the typical size of this perturbation is of the order of kHz (often comparable in size to  $\nu_Q^{(2)}$ ). Like the SOQI, the anisotropic part of  $\nu_{CS}$  can break the mirror symmetry of the first-order powder pattern (Fig. 4c), and is important to consider when the FOQI is removed. However, nitrogen CS tensors are far more easily studied using the  $^{15}\text{N}$  isotope due to the absence of the quadrupolar interaction, and CS parameters determined using  $^{14}\text{N}$  are therefore far less frequently reported than EFG parameters. The most commonly used chemical shift reference in the solid-state  $^{14}\text{N}$  NMR literature is solid ammonium chloride, and  $\delta_{iso}$  values mentioned in this article are given relative to the  $^{14}\text{N}$  signal from this compound at 0 ppm.

Additional perturbations to the  $^{14}\text{N}$  transition frequencies can be caused by dipolar couplings (both homo- and heteronuclear). By far the most frequently observed example is  $^1\text{H}$ - $^{14}\text{N}$  dipolar coupling. A  $^{14}\text{N}$  spin coupled to a single  $^1\text{H}$  nucleus will experience a splitting of each of its transitions  $\nu_d$ , given by:

$$\nu_d = \frac{\mu_0 h \gamma_N \gamma_H}{8\pi^3 r_{\text{NH}}^3} (3 \cos^2 \xi - 1) \quad (13)$$

where  $\mu_0$  is the permeability of free space,  $\gamma_H$  is the gyromagnetic ratio of  $^1\text{H}$ ,  $r_{\text{NH}}$  is the N-H distance and  $\xi$  is the angle between the N-H vector and  $B_0$ . This splitting is typically of the order of 10 kHz for a directly bonded proton, and the inverse-cubed dependence on the N-H distance makes this quantity extremely useful in determining bond lengths in

systems with “isolated”  $^1\text{H}$ - $^{14}\text{N}$  spin pairs. In samples with multiple hydrogen sites, the interaction will be present for all  $^1\text{H}$ - $^{14}\text{N}$  spin pairs, and homonuclear  $^1\text{H}$ - $^1\text{H}$  couplings can further complicate matters. The primary effect of this interaction on a first-order  $^{14}\text{N}$  powder pattern will be analogous to line-broadening, and will generally only be noticeable for small  $C_Q$  values. However, the dipolar interaction can also contribute strongly to  $^{14}\text{N}$  relaxation, which can dramatically affect the shape of the pattern in certain instances (see Section 4.4).

### 3. Single-crystal samples

In a single crystal, each set of magnetically distinct  $^{14}\text{N}$  spins will have a common EFG (and CS) tensor orientation, and will therefore give rise to two resonance lines, one for each of the fundamental transitions. The separation of these resonances is determined primarily by the FOQI, and is therefore commonly on the order of MHz. Their mean frequency is also altered, typically by several kHz, by both the SOQI and CS. Experimentally, the distribution of these resonances over such wide frequency ranges, combined with limitations in RF pulse excitation bandwidths, means that a number of experiments may have to be performed with an incremented transmitter frequency in order to locate the signals. Once found, however, the linewidths are relatively narrow (on the order of a few kHz), depending primarily on heteronuclear dipolar couplings present in the sample (broadening due to  $^{14}\text{N}$  homonuclear couplings is usually minimal due to the low value of  $\gamma_N$  and the relatively large separation between nitrogen sites in most systems). These narrow linewidths allow simple, transition-selective, one-pulse excitation or cross-polarization (CP) [4] schemes to be used, and spectra of high signal-

to-noise ratio (S/N) and high resolution can be obtained relatively easily from nitrogen sites of arbitrary  $C_Q$ .

Since the perturbations due to the quadrupolar interaction and CSA are dependent on the orientations of the EFG and CS tensors with respect to  $B_0$ , changing the orientation of the crystal will alter the positions of the resonance lines. By recording their frequencies as a function of the rotation angle about two orthogonal axes and fitting these to derived expressions [5],  $^{14}\text{N}$  NMR can be used to determine not only the principal components of the interaction tensors, but also their relative orientations in the molecular frame (provided that the orientations of the crystallographic axes are known). Assignment of parameters to the correct sites can often be facilitated by a consideration of site symmetry; for example, a nitrogen atom located on an axis of  $C_3$  symmetry or higher will necessarily have axially symmetric interaction tensors, and principal components will be aligned within, or perpendicular to, mirror-planes if present.

Several early continuous wave (CW)  $^{14}\text{N}$  NMR experiments were carried out on single crystals. Linzer and Forman recorded a  $^{14}\text{N}$  NMR spectrum from a single crystal of  $\text{ND}_4\text{Cl}$ , which has cubic symmetry and therefore no quadrupolar interaction [6], while DeReggi *et al.* studied relaxation in the  $\alpha$ - and  $\beta$ -phases of  $\text{N}_2$  [7]. Whitehouse *et al.* were the first to report a single-crystal rotation study on a sample with a sizeable  $C_Q$  (*ca.* 600 kHz) [5]. They carried out CW NMR experiments on large single-crystals of uranyl nitrate hexahydrate (Fig. 5) and rubidium uranyl nitrate, observing four and six pairs of  $^{14}\text{N}$  resonances respectively and discussing the results in light of the crystal structures. Griffin and coworkers subsequently published several papers using pulsed Fourier transform NMR (hereafter referred to simply as “NMR”), and in particular they discussed

the effects of  $^1\text{H}$ - $^{14}\text{N}$  dipolar couplings on the  $^{14}\text{N}$  NMR spectra, demonstrating the advantages of  $^1\text{H}$  decoupling [8] as well as selective cross-polarization from the protons to the fundamental  $^{14}\text{N}$  transitions [9,10]. For example, a single-crystal of *N*-acetylvaline (NAV) shows two pairs of quadrupolar-split  $^{14}\text{N}$  resonances corresponding to the two magnetically distinct nitrogen sites (Fig. 6). Each of these lines are further split into doublets with the size of the splitting corresponding to  $\nu_d$ , the  $^1\text{H}$ - $^{14}\text{N}$  dipolar coupling perturbation given in Eq. (13). The application of a  $^1\text{H}$  decoupling field removes this interaction and eliminates the splitting, also narrowing the linewidths and improving the S/N. However, since  $\nu_d$  is dependent both on  $r_{\text{NH}}$  and  $\xi$ , an analysis of the dipolar splitting as a function of crystal orientation can allow a measurement of both the N-H bond length and the orientation of this bond in the crystal frame. Griffin and coworkers were therefore able to use single-crystal  $^{14}\text{N}$  NMR to determine not only the nitrogen EFG parameters of NAV ( $C_Q = 3.21$  MHz and  $\eta_Q = 0.32$ ), but also the N-H distance (1.06 Å) [9].

Aside from the favorable natural abundance of  $^{14}\text{N}$ , an advantage of measuring dipolar couplings using this nucleus, as opposed to, say,  $^{13}\text{C}$ , is the improved resolution afforded by the quadrupolar interaction, which results in doublets that are well-separated in the frequency domain. However, for certain crystal orientations the dipolar couplings may cause broadened or overlapping lineshapes from which the splittings cannot be resolved. In this case, while  $^1\text{H}$  decoupling can narrow the linewidths, the dipolar coupling information is lost. To resolve this issue, Bodenhausen *et al.* proposed a two-dimensional, separated local field (SLF) type pulse sequence [11,12] to separate the effects of the quadrupolar and dipolar splittings into different dimensions [13]. After

cross polarization from  $^1\text{H}$  to  $^{14}\text{N}$ , refocusing pulses are applied simultaneously to both spins during the evolution period, retaining the effects of the dipolar couplings while the quadrupolar interaction is refocused. Subsequently, the dipolar couplings are eliminated during the acquisition period by  $^1\text{H}$  decoupling and the observed  $^{14}\text{N}$  signal evolves under the quadrupolar interaction. The resultant DISQUO (DIpolar Splittings, QUadrupolar Offset) spectrum shows the quadrupolar-split  $^{14}\text{N}$  spectrum in the direct dimension, correlated with  $^1\text{H}$ - $^{14}\text{N}$  dipolar splittings in the indirect dimension (Fig. 7).

More recently, an alternative method for correlating  $^1\text{H}$ - $^{14}\text{N}$  dipolar couplings with  $^{14}\text{N}$  quadrupolar-split spectra has been reported. The PISEMA experiment (Polarization Inversion Spin Exchange at Magic Angle) was originally used to obtain correlations between dipolar couplings and chemical shifts using the  $^{15}\text{N}$  nucleus [14], and subsequently Qian *et al.* developed a version for single-crystal  $^{14}\text{N}$  experiments [15]. The pulse sequence provides narrower linewidths in the indirect (dipolar) dimension than SLF-type experiments due to the use of Lee-Goldburg homonuclear decoupling [16], which is applied to the protons during the evolution period. Such decoupling has a considerable line-narrowing effect with minimal scaling of the dipolar spectral range (0.82). The authors demonstrated this experiment on a single-crystal of NAV, with separate experiments run for each  $^{14}\text{N}$  resonance (Fig. 8). Nitrogen sites with smaller quadrupolar splittings gave broader dipolar-split peaks due to the breakdown of  $^{14}\text{N}$  transition selectivity, though this problem can be remedied by simply adjusting the crystal orientation to increase the quadrupolar splitting. Optimal proton decoupling frequencies were shown to be dependent on the size of the dipolar splitting, and were found to be different for each  $^{14}\text{N}$  resonance.

While  $^1\text{H}$ - $^{14}\text{N}$  dipolar couplings are dominant in most cases, homonuclear  $^{14}\text{N}$ - $^{14}\text{N}$  dipolar couplings can also be observed and utilized. Suter and Ernst used two-dimensional  $^{14}\text{N}$  experiments to study a single crystal of ammonium sulfate ( $C_{\text{QS}} \leq 155$  kHz), observing cross-peaks between non-equivalent nitrogen sites (Fig. 9) and discussing the importance of the dipolar coupled proton network in determining the spin-diffusion rates [17]. Subsequently, by varying the crystal orientation, they observed an increase in the spin diffusion time between two sites that was proportional to the square of the frequency difference between the resonance lines, and showed that this was in agreement with expressions derived from perturbation theory [18]. The authors were then able to assign the two pairs of resonances to distinct crystallographic sites by measuring the homonuclear dipolar coupling constants and comparing these with values calculated from the crystal structure.

McDowell and co-workers applied  $^1\text{H}$ - $^{14}\text{N}$  cross-polarization with  $^1\text{H}$  decoupling to study a series of single-crystal amino acids (L-serine-monohydrate [19], L-asparagine monohydrate [20] and L-histidine hydrochloride monohydrate [21]) using a probe specially designed to reduce acoustic ringing and featuring an accurate goniometer for adjustment of the crystal orientation [22]. In addition to a determination of the  $^{14}\text{N}$  EFG parameters, they also studied the effects of  $^{14}\text{N}$ - $^{13}\text{C}$  dipolar couplings on the  $^{13}\text{C}$  spectra, an analysis of which allows a determination of the sign of the  $^{14}\text{N}$   $C_{\text{Q}}$  as mentioned in Section 2 (such phenomena are discussed in more detail elsewhere [1]). They also quantified the SOQI by plotting the mean position of the  $^{14}\text{N}$  resonance pairs as a function of crystal orientation (Fig. 10). Remarkably good agreement with the simulations was demonstrated, confirming the high accuracy of the measured EFG

parameters, with small deviations in the fits attributed to the effects of the  $^{14}\text{N}$  CSA. In fact,  $^{14}\text{N}$  CS parameters have also been quantified by this method in lithium nitride by Differt and Messer [23], and in potassium nitrate by Bastow and Stuart [24]. The latter authors subtracted the second-order quadrupolar shifts from the mean frequencies of the  $^{14}\text{N}$  resonances to obtain a chemical shift rotation pattern, from which the principal components and orientation of the  $^{14}\text{N}$  CS tensor were determined ( $\Delta_{\text{CS}} = 150$  ppm and  $\eta_{\text{CS}} = 0.01$ ).

Liechti and Kind used single-crystal  $^{14}\text{N}$  NMR to study a solid solution in which translational disorder causes a distribution in EFGs, leading to an inhomogeneous broadening of the linewidths [25]. The authors developed a formalism by which the variation and covariation in  $^{14}\text{N}$  linewidths with crystal orientation can be used to extract variances in EFG distributions in disordered systems. The  $((\text{CH}_3)_4\text{N})_2\text{CuBr}_x\text{Cl}_{4-x}$  system that they chose to study has two inequivalent nitrogen sites, and as the composition  $x$  is varied, one site experiences a change in  $C_Q$ , and the other a change in  $\eta_Q$ . A Gaussian distribution in these parameters was modeled and the experimental data accurately fitted to obtain mean EFG parameters and their standard deviations, a useful approach for the study of defects, impurities or substitutions in single-crystal samples. Zalar *et al.* would later study substitutionally-disordered cyanide crystals featuring extremely broad  $^{14}\text{N}$  frequency distributions [26], and this work is discussed in Section 4.2.

Harbison and co-workers have carried out  $^{14}\text{N}$  single-crystal experiments on a diverse range of materials, including silver, barium and lead nitrates [27], the Schiff base *N*-9-anthrylmethylidene [28], the heterocyclic compound hexamethylenetetramine (HMT) [29], and sulfamic acid [30]. For the nitrates, whose crystal structures were at the

time a matter of controversy, eight resonance lines were observed, arising from a single set of EFG parameters rotated by  $2_1$  symmetry around three orthogonal axes. This allowed the symmetry space groups of the structures to be identified as *Pbca* for silver nitrate and *Pa3* for barium and lead nitrates [27]. In the  $^{14}\text{N}$  spectra of sulfamic acid, dipolar couplings between the nitrogen and three attached protons were observed at certain orientations as a 1:3:3:1 quartet. In another notable single-crystal  $^{14}\text{N}$  NMR study, Mangum and Utton investigated cerous magnesium nitrate ( $\text{Ce}_2\text{Mg}_3(\text{NO}_3)_{12}\cdot 24\text{H}_2\text{O}$ ) at a temperature of 1K, in which the paramagnetic  $\text{Ce}^{3+}$  ions align with  $B_0$  causing orientation-dependent dipolar contributions to the field at the nitrogen nuclei [31]. Baviera *et al.* observed the  $^{14}\text{N}$  chemical shift and  $C_Q$  as a function of temperature in tetramethylammonium manganese chloride to study a structural phase transition at *ca.* 125 K [32]. Single-crystal  $^{14}\text{N}$  NMR has also been used to study other ammonium and tetramethylammonium salts [33-36], various phases of ammonium tetrachlorozincates [37], and gallium nitride films [38].

## 4. Stationary powder samples

### 4.1 Symmetric environments

In a powder sample, all EFG orientations will be present for each nitrogen site, resulting in characteristic powder patterns such as those shown in Fig. 3. Provided that such patterns can be acquired, the frequencies of the discontinuities (Eq. (5), (6) and (7)) can be used to determine the EFG parameters. For nitrogen sites with small EFGs ( $C_Q < ca.$  200 kHz), it is possible to excite the full width of the  $^{14}\text{N}$  powder pattern using standard (rectangular, monochromatic) RF pulses and to acquire the complete pattern in a

single experiment. The quadrupolar echo pulse sequence ( $\pi/2_x - \tau - \pi/2_y - \tau - \text{acquire}$ ) is most commonly used, allowing the acquisition of the free induction decay (FID) to begin at the echo-top and thus eliminating distortions due to receiver dead time or acoustic ringing. Broad powder patterns that can be obtained in a single experiment are commonly referred to as “wideline”. While  $C_Q$  values of *ca.* 200 kHz or less are much lower than average for  $^{14}\text{N}$  (Fig. 2), they are often observed for sites of relatively high spherical symmetry. For example, nitrogen sites that are tetrahedrally coordinated to four identical species, such as those found in ammonium or tetraalkylammonium salts, tend to have small EFGs and correspondingly low  $C_Q$  values.

There are some early studies reporting  $^{14}\text{N}$  CW NMR results from powder samples, some with spherically-symmetric nitrogen environments [39-41], and others with sizeable  $C_Q$  values such as metal nitrates [5]. In uranium nitride, which has a cubic NaCl-type structure, narrow linewidths were observed, allowing the Knight shift [42] (a perturbation caused by the presence of conduction electrons) to be measured as a function of temperature [41]. For the metal nitrates, only two relatively broad, weak discontinuities could be observed, allowing a determination of the  $C_Q$ - $\eta_Q$  relationship but not the specific values [5]. Segel subsequently used CW NMR to determine the  $^{14}\text{N}$   $C_Q$  values in ammonium perrhenate [43] and metaperiodate [44] as 50 kHz and 13 kHz respectively.

The advantages of pulsed Fourier transform methods, and particularly the quadrupolar echo pulse sequence, were first highlighted by Siminovitch *et al.*, who acquired motionally-averaged  $^{14}\text{N}$  powder patterns from lipid bilayers composed of dipalmitoyl phosphatidylcholine (DPPC) [45]. This work, along with that of Rothgeb

and Oldfield [46], spurred much interest in  $^{14}\text{N}$  NMR as a tool for the study of model membrane systems, and this application is treated separately in Section 7. More recently, MacKenzie *et al.* recorded  $^{14}\text{N}$  spectra from a series of cubic titanium nitrides and carbonitrides [47], while Ono *et al.* observed narrow lineshapes from both ions in cubic piperidinium nitrate [48].  $^{14}\text{N}$  relaxation studies have also been carried out on a range of powder samples featuring highly symmetric nitrogen sites in order to probe phase transitions [49-54], molecular dynamics [55-60] and incommensurate systems that lack translational symmetry [61-64].

Punkkinen and co-workers studied the  $^{14}\text{N}$  powder pattern arising from ammonium perchlorate ( $C_Q = 27$  kHz) after a general echo sequence and compared the resultant lineshapes with simulations taking into account finite RF powers and pulse durations [65]. They also used the same system to acquire a  $^{14}\text{N}$  double-quantum spectrum [66]. Three RF pulses were used to excite  $^{14}\text{N}$  double-quantum coherence, convert it to observable single-quantum coherence and then to refocus this coherence. This allowed the spin-echo amplitude to be monitored as a function of the double-quantum evolution time, a modulation which can be Fourier transformed to obtain the double-quantum spectrum (Fig. 11). Such an approach was originally proposed by Vega for applications to  $^2\text{H}$  NMR [67], and can be applied to  $^{14}\text{N}$  NMR of systems with small  $C_Q$ s in which the double-quantum excitation and conversion is relatively efficient. Since the +1 and -1 energy levels of a spin-1 nucleus are perturbed identically by the FOQI (Fig. 1), the double-quantum spectrum shows vastly reduced linewidths due to the absence of first-order quadrupolar broadening.

Pratum and Klein used both direct excitation and CP methods to obtain  $^{14}\text{N}$  powder patterns from a variety of tetraalkylammonium and choline salts, measuring  $C_{\text{QS}}$  of up to *ca.* 200 kHz [68-70]. As mentioned in the previous section, selective cross-polarization from  $^1\text{H}$  to one of the fundamental  $^{14}\text{N}$  transitions in a single-crystal sample is relatively straightforward due to the narrow  $^{14}\text{N}$  linewidths and the large quadrupolar splitting, which allow selective spin-locking of the  $^{14}\text{N}$  magnetization. For wide-line  $^{14}\text{N}$  powder patterns, a large distribution in resonance frequencies is present, thus the ability to select a single transition is lost and the behavior of the  $^{14}\text{N}$  spin ensemble under RF irradiation is complex. In addition, the  $^1\text{H}$ - $^{14}\text{N}$  dipolar couplings which facilitate the polarization transfer are orientation dependent and therefore vary in strength across the  $^{14}\text{N}$  powder pattern. Pratum and Klein derived expressions describing two distinct Hartman-Hahn match conditions and deduced the  $^{14}\text{N}$  coherences generated by each of them [69]. Using both spin-lock and “adiabatic demagnetization in the rotating frame” (ADRF) methods [4], they observed the resulting single-quantum  $^{14}\text{N}$  signals, as well as the double-quantum coherences (converted to single-quantum coherences using RF pulses). For a relatively wide  $^{14}\text{N}$  pattern (ammonium sulfate, total width *ca.* 230 kHz), these cross-polarization schemes resulted in  $^{14}\text{N}$  spectra consisting of two broad “lobes” at equal offsets from  $\nu_0$ , with the offsets dependent on the RF power applied. While these lobes were insufficient in breadth to cover the complete  $^{14}\text{N}$  powder pattern of ammonium sulfate itself, they were broad enough to span the full patterns of several tetraalkylammonium salts with only minor distortions resulting (Fig. 12). Cross-polarization for these particular samples was particularly advantageous given the relatively long  $^{14}\text{N}$   $T_1$  values in these samples ( $> 60$  s).

The same authors also observed non-zero  $\eta_Q$  values, which would not normally be expected from the axially-symmetric nitrogen sites in the systems studied, indicating the presence of fast molecular dynamics that lead to the observation of motionally-averaged EFG tensors [70]. Temperature dependent distortions in the observed lineshapes also provided evidence for intermediate-regime motions with correlation times on the order of  $C_Q^{-1}$ . Any motions on this timescale which alter the magnitude or orientation of the EFG tensor principal components will cause anisotropic transverse relaxation, resulting in powder patterns whose shapes are highly sensitive to the correlation time of the dynamics, the motional geometry, and the inter-pulse delay times in the echo experiment used. This phenomenon was already well-known from  $^2\text{H}$  NMR [71-73], which is a commonly used probe of molecular dynamics. Like  $^{14}\text{N}$ ,  $^2\text{H}$  is a spin  $I = 1$  nucleus in which the FOQI dominates, thus the theoretical framework developed for the study of dynamics using  $^2\text{H}$  is easily extended to  $^{14}\text{N}$ . The primary advantage of  $^2\text{H}$  is its much smaller quadrupole moment ( $Q = 2.86$  mbarn), which results in narrow powder patterns even for asymmetric environments. In the samples studied by Pratum and Klein, the small  $C_Q$  values ( $\leq 100$  kHz) allowed the  $^{14}\text{N}$  powder patterns to be obtained relatively easily [70], and Fig. 13 shows spectra obtained from choline chloride, along with simulations taking into account a  $180^\circ$  flipping of the choline cation.

Fechtelkord *et al.* later showed that dynamics could also affect  $^{14}\text{N}$  powder patterns *via* the motional averaging of heteronuclear dipolar couplings [74]. They observed that the  $^{14}\text{N}$  spectrum of letovicite  $((\text{NH}_4)_3\text{H}(\text{SO}_4)_2)$  was featureless at temperatures below 400 K due to  $^1\text{H}$ - $^{14}\text{N}$  couplings. As the temperature was raised, the quadrupolar pattern ( $C_Q = 68$  kHz) became visible, indicating the onset of motional

averaging of the heteronuclear couplings. Motional averaging of EFG tensors and dipolar couplings would also later be observed in samples with much larger  $^{14}\text{N}$   $C_Q$  values (see Section 4.3).

Thangaraj *et al.* also exploited the tetrahedral symmetry of tetraalkylammonium ions, this time in order to study the Brønsted acid sites in various catalytic zeolite systems [75]. They compared  $^{14}\text{N}$  spectra obtained from the  $\text{Me}_4\text{N}^+$  ion in the bromide salt and in the zeolite ZK-4. In the salt, a single quadrupolar pattern is present ( $C_Q = 25$  kHz, Fig. 14a), while in the zeolite three distinct lines were observed (Fig. 14e): (1) a narrow component from mobile species in the  $\alpha$  cage, (2) a broader component from species with restricted mobility in the  $\alpha$  cage (postulated to be interacting with the framework), and (3) a component with visible quadrupolar splitting ( $C_Q = ca. 25$  kHz) arising from motionally restricted ions in the smaller  $\beta$  cage. For the larger  $\text{Et}_4\text{N}^+$  ion in ZSM-20, only a narrow line was observed (Fig. 14c), suggesting that this ion is mobile within the larger cages and is not present within the smaller cages. The authors also recorded a  $^{14}\text{N}$  spectrum from zeolite H-Y after saturation with ammonia gas. Since the  $^{14}\text{N}$  signal from free  $\text{NH}_3$  species would be too broad to observe with a quadrupolar echo sequence ( $C_Q = 3.16$  MHz), they concluded that the observed  $^{14}\text{N}$  signal must arise from  $\text{NH}_4^+$  ions formed at the Brønsted acid sites.  $^{14}\text{N}$  NMR has also been used to study zeolite formation using amphiphilic templates, and this is discussed in Section 7.

## 4.2 Piecewise acquisition

For powder samples featuring  $^{14}\text{N}$   $C_{Qs} > ca. 200$  kHz, the widths of the  $^{14}\text{N}$  powder patterns are too large to be uniformly excited by standard RF pulses. It is

becoming common to refer to such powder patterns as "ultra-wideline". These spectra can be acquired in a number of separate pieces, or "sub-spectra", whose individual widths are determined by the excitation and refocusing bandwidths of the RF pulses used. Sub-spectra can be acquired over the full width of the powder pattern either by adjusting  $B_0$  (field sweeping/stepping), or by incrementing the RF transmitter frequency (frequency stepping). Since the adjustment of  $B_0$  requires specialized hardware, the latter approach is far more common. The full powder pattern can then be obtained by co-adding the sub-spectra or using a skyline projection, the latter option reducing the effects of spectral distortions arising from non-uniform overlap of sub-spectra at a cost of reducing the overall S/N ratio. Several acronyms have been suggested for this simple approach to ultra-wideline NMR [76,77], but the general term "piecewise" is sufficient. Prior to this method, it was common to plot the amplitudes of time-domain signal intensities (*e.g.*, spin-echo heights) versus frequency as a histogram, but such an approach is less efficient and results in poor resolution in the frequency domain.

Hill and Yesinowski were the first to report a piecewise, ultra-wideline  $^{14}\text{N}$  powder pattern (Fig. 15), acquiring the spectrum from potassium nitrate ( $C_Q = 751$  kHz,  $\eta_Q = 0.022$ ) at 7.05 T [78]. The total width of this  $^{14}\text{N}$  pattern is *ca.* 1.1 MHz, which at the time was far wider than any previously recorded. In addition to the piecewise acquisition method, the authors took advantage of the mirror-symmetry of first-order  $^{14}\text{N}$  powder patterns. Since  $\nu_Q^{(1)} \gg \nu_Q^{(2)}$  and  $\nu_{CS}$ , the latter perturbations can be neglected and only the high-frequency half of the pattern is acquired, the other half being reconstructed by reflection. As a corollary, such an approach rules out the possibility of studying the CS tensor, and is only suitable for determining the EFG parameters.

Although CS parameters can in principle be measured from a full, high-resolution, ultra-wideline  $^{14}\text{N}$  powder pattern (ideally at a high field where the effects of this interaction are more pronounced), they are far more easily ascertained from  $^{15}\text{N}$  experiments conducted on isotopically-enriched samples.

In order to boost the signal obtained from each sub-spectrum, Hill and Yesinowski employed the quadrupolar Carr Purcell Meiboom Gill (QCPMG) protocol [79]. This is now a widely-used signal enhancement technique in solid-state NMR, and has been reviewed elsewhere [80]. The defining feature of QCPMG is an excitation pulse followed by a repeating loop containing both a refocusing pulse and an acquisition period. This allows the spin-echo to be continuously refocused and recorded multiple times in each scan (potentially over the full timescale of the transverse relaxation). The resultant train of echoes can be Fourier transformed in its entirety, producing a spectrum that consists of a series of narrow lines, or "spikelets", whose manifold reproduces the powder pattern that would be obtained using a regular spin-echo experiment. Alternatively, the echoes can be co-added before processing, resulting in a spectrum of standard appearance such as that in Fig. 15. S/N enhancements of several orders of magnitude are commonly obtained using this approach, and  $^{14}\text{N}$  echo trains have also been obtained from solid samples under magnetic field gradients for imaging applications [81]. The  $^{14}\text{N}$  nuclei in potassium nitrate show relatively slow transverse relaxation, and Hill and Yesinowski acquired 512 echoes for each sub-spectrum, resulting in a considerable S/N enhancement of *ca.* 20. The width of each sub-spectrum was 40 kHz, necessitating the acquisition of 33 sub-spectra for the high-frequency half of the pattern.

This relatively small excitation bandwidth is due to the low gyromagnetic ratio of  $^{14}\text{N}$ , which results in long  $\pi/2$  and  $\pi$  pulse lengths even at high RF powers.

Zalar *et al.* used a frequency-stepped spin-echo experiment to map out  $^{14}\text{N}$  spectra several MHz in width from crystals of  $\text{Na}_{1-x}\text{K}_x\text{CN}$  in a point-by-point fashion (Fig. 16) [26]. Such spectra arise from the crystals due to orientational distributions of the  $\text{CN}^-$  ions, each of which has a  $^{14}\text{N}$   $C_Q$  of *ca.* 4 MHz. These spectra were compared with simulations, which revealed that the  $\text{CN}^-$  ions predominantly align along the [100], [010] and [001] crystallographic axes (*i.e.*, pointing towards the surrounding alkali ions), with an angular dispersion of *ca.*  $8^\circ$ . As with the work of Hill and Yesinowski mentioned above, the small excitation bandwidth of the RF pulses used resulted in very long acquisition times for each of these spectra (up to several weeks). In Section 4.4, the use of frequency-swept RF pulses to improve the excitation bandwidth and provide broader sub-spectra is described.

### 4.3 Fixed frequency techniques

To reduce the experimental times required to record individual  $^{14}\text{N}$  sub-spectra, Hill and Yesinowski introduced the "RotIsseRIe" technique (Reorientation-Induced Redistribution of Isochromats) [78]. This technique takes advantage of the fact that only a very small section of the powder pattern is observed at any one time. By slowly rotating the sample (*ca.* 1 rpm) about an axis perpendicular to  $B_0$ , the value of  $\nu_Q^{(1)}$  is modulated and thus the  $^{14}\text{N}$  resonances of each individual crystallite are swept over wide frequency ranges just like in the single-crystal rotation experiments discussed in Section 3. After each scan, the excited spins are therefore moved out of the observation window

to be replaced by a “fresh” set at thermal equilibrium that can be excited immediately. The initial spin set then has time to fully relax before the sample rotation brings them back into the observation window. The recycle delay needs to be long enough to allow the saturated set of crystallites to move outside of the detection window, and the sample rotation period should ideally be set to a value longer than  $T_1$  so that this set of crystallites has relaxed by the time the sample returns to its initial position. Using RotIsseRIe, Hill and Yesinowski were able to record a sub-spectrum from potassium nitrate using a recycle delay of just 2 s, despite a  $^{14}\text{N}$  spin-lattice relaxation time of  $T_1 = 40$  s [78], and this approach was subsequently used to record one half of the  $^{14}\text{N}$  spectrum from silicon nitride ( $C_Q \approx 2.1$  MHz) [2].

The same authors also observed that the modulation of  $\nu_Q^{(1)}$  by slow sample rotation causes a variation in spin-echo amplitudes, and realized that this could be used to deduce quantitative information on the interaction itself [82]. After the excitation pulse of a Hahn echo experiment ( $\pi/2 - \tau - \pi - \tau - \text{acquire}$ ), the changes in the resonance frequencies of the excited spins due to the rotation means that the  $\pi$  pulse will fail to completely refocus the transverse magnetization. The spin-echo therefore experiences an attenuation that will vary with  $\tau$  in a way that depends on the rotation speed, the orientation of the rotation axis relative to  $B_0$ , and the quadrupolar interaction itself (*i.e.*,  $C_Q$  and  $\eta_Q$ ). Hill and Yesinowski named this effect STEAMER (Slow Turning for Echo Amplitude Modulation and Echo Reduction) [82], and derived simple, numerical and analytical expressions describing the echo attenuation for the case of an axially symmetric  $^{14}\text{N}$  EFG tensor and a rotation axis perpendicular to  $B_0$ . Experimentally measured echo decay values from potassium nitrate matched the simulated STEAMER

curve very closely (Fig. 17), thus providing a method for determining the  $C_Q$  value at a fixed transmitter frequency. This curve was, however, modeled with the *a priori* knowledge that  $\eta_Q = 0$ . For samples with non-zero asymmetry parameters, two further variables are introduced ( $\eta_Q$ , and the rotation angle about the EFG principal axis  $V_{33}$ ), necessitating the simultaneous fitting of multiple STEAMER curves obtained at different frequency offsets or different rotation rates. The relatively fast echo attenuation caused by the STEAMER effect also highlights an important point regarding the RotIsseRIe experiment: the possibility of using QCPMG enhancement is eliminated by continuous sample rotation because of STEAMER dephasing. In order to take advantage of both RotIsseRIe and QCPMG enhancement, the sample orientation must be stepped incrementally between each scan, rather than rotated continuously [2].

Finally, Hill and Yesinowski also noted that dynamic processes can also dephase the  $^{14}\text{N}$  coherences, and went on to report a “hole-burning” approach that can allow dynamics to be studied using  $^{14}\text{N}$  NMR in powder samples with very large  $C_Q$  values [83]. They considered the hexamethylenetetramine (HMT) molecule ( $C_Q = 4.41$  MHz,  $\eta_Q = 0$ ), which in its crystalline form undergoes tetrahedral jumps at a rate of *ca.*  $10\text{ s}^{-1}$  at room temperature, thus moving the  $^{14}\text{N}$  EFG tensor between four orientations. Such a rate is too slow to be observed as a change in the shape of the  $^{14}\text{N}$  powder pattern, but is accessible *via* its effect on the  $^{14}\text{N}$  spin-lattice relaxation ( $T_1 \approx 1$  s). Hill and Yesinowski applied trains of transition selective pulses (Delays Alternating with Nutation for Tailored Excitation, or “DANTE” trains [84]) to saturate a 4 kHz wide region of the observed spectral piece and then monitored the relaxation of this “hole” over time using a conventional Hahn echo (Fig. 18). After a single DANTE train, a set of  $^{14}\text{N}$  spins

corresponding to a specific set of EFG orientations is saturated. These saturated EFG orientations are then altered by the molecular reorientation, which brings unsaturated magnetization (*i.e.*,  $^{14}\text{N}$  spins previously at other EFG orientations) into the hole region, a process analogous to RotIsseRIe. Thus, for the four-site jump process, three quarters of the magnetization is quickly recovered due to the dynamics alone. This is followed by a much slower recovery of the remaining magnetization due to ordinary spin-lattice relaxation (Fig. 18a). Over the course of 16 DANTE trains (separated by a duration similar to the correlation time of the dynamics), the reorientation causes all four sets of EFG orientations to saturate, thus the recovery of magnetization occurs only by spin-lattice relaxation (Fig. 18b). An advantage of this approach is that it allows an immediate quantification of the number of jump sites involved. The authors derived expressions to model these phenomena and also considered “whole-burning” approaches where the entire observed sub-spectrum is saturated.

#### 4.4 Frequency-swept pulses

The relatively small excitation bandwidths associated with standard RF pulses, which can make the piecewise acquisition of ultra-wideline  $^{14}\text{N}$  powder patterns very inefficient, can be improved by using amplitude- and phase-modulated pulses whose frequencies are swept across the powder patterns at a constant rate, exciting the isochromats sequentially. This concept was first proposed by Bhattacharyya and Frydman [85], who showed that WURST pulses (Wideband, Uniform Rate, Smooth Truncation, sometimes also referred to as “chirp” pulses) [86], could be used to both excite and refocus a broad range of frequencies even at relatively low RF powers. O’Dell

and Schurko subsequently extended the concept to a WURST-QCPMG sequence [87], which can allow the very rapid acquisition of ultra-wideline  $^{14}\text{N}$  powder patterns [88]. When applying this pulse sequence to a powder pattern whose width is comparable to the bandwidth of the WURST pulse, a signal enhancement mechanism can be also exploited to provide a moderate gain in S/N. Since the effective frequency of the WURST pulses is swept across the powder pattern, they will excite the fundamental transitions of each crystallite in turn (Fig. 19a). The excitation of the first transition results in an increase in the Zeeman polarization of the second, thus the coherences resulting from the excitation of the second transition are enhanced, boosting the signal for the second half of the powder pattern (*i.e.*, in the direction of the sweep of the WURST pulses, Fig. 19b and c). This “population transfer” effect is analogous to other experiments used to enhance the central transition polarization of half-integer quadrupolar nuclei by irradiating the satellite transitions [89], with two main differences. First, rather than being a preparatory pulse sequence applied before a regular experiment, it is the excitation and refocusing pulses themselves that achieve the population transfer. The effect was therefore given the name DEISM (Direct Enhancement of Integer Spin Magnetization) [88]. Secondly, the enhancement is not applied to a particular transition, but rather to specific crystallite orientations of each transition. This effect also causes distortions to the other side of the powder pattern (Fig. 19b and c). However, when acquiring ultra-wideline patterns in a piecewise fashion, the sweep direction of the WURST pulses can be set to low-to-high frequency for pieces acquired on the high frequency side, and *vice versa*. Using this approach, the signal enhancement can be obtained across the entire pattern and the distortions are not observed in the resultant spectrum. Alternatively, the other half of the

pattern can be reconstructed by reflection as mentioned above. O'Dell and co-workers have used this strategy to acquire  $^{14}\text{N}$  spectra from several amino acids at moderate magnetic field strengths and relatively short experimental times compared with other techniques [90,91]. The limitation of this approach is that, in order for the DEISM enhancement to occur over the complete pattern, the effective sweep range of the WURST pulses must exceed the full pattern width. This restricts the utility of this enhancement mechanism to samples with  $C_Q$ s of *ca.* 1 MHz or less.

Despite the limitations associated with the DEISM effect, the broad excitation bandwidth and QCPMG enhancement of the WURST-QCPMG pulse sequence still provide an efficient way of acquiring ultra-wideline powder patterns from samples with large  $C_Q$  values. O'Dell and Ratcliffe used the sequence to record the powder pattern from a sample of deuterated urea ( $C_Q = 3.47$  MHz,  $\eta_Q = 0.31$ ), and noted the effects of molecular dynamics on the lineshape (Fig. 20) [92]. Using the EXPRESS software [93] to model the effects of the  $180^\circ$  flipping around the carbonyl bond, they noted that the outermost edges of the powder patterns exhibited the strongest  $T_2$  anisotropy, allowing the flip rate to be quantified from this region of the pattern alone. To simulate the WURST-QCPMG experiment in the presence of dynamics would be highly computationally demanding due to the complex nature of the pulse shapes, the long acquisition times, and the large number of crystallite orientations over which the simulations must be averaged. The authors therefore simulated simple quadrupolar echo spectra with specific inter-pulse delays, and matched these to experimental spectra obtained over a range of timescales from a single WURST-QCPMG experiment by processing individual echoes extracted from the QCPMG train. This approach allowed

the measurement of the urea flip rate at several temperatures and subsequent extraction of the activation energy, which was found to be in good agreement with values determined by other techniques [92].

Further effects of dynamics and relaxation on ultra-wideline  $^{14}\text{N}$  powder patterns were subsequently reported by O'Dell *et al.* [94]. They demonstrated that variations in  $^1\text{H}$ - $^{14}\text{N}$  dipolar couplings can give rise to  $^{14}\text{N}$  relaxation/dephasing anisotropies, resulting in variations in QCPMG enhancement across the  $^{14}\text{N}$  powder pattern. In particular, significant differences in the transverse relaxation time ( $T_2$ ) for the two types of nitrogen site in 2,4,6-triamino-s-triazine (melamine) were observed. The molecule has three C-N-C (ring) nitrogen sites and three C-NH<sub>2</sub> (amine) sites, totaling six crystallographically distinct sites overall. While these six sites could not be individually resolved, a simulation of the  $^{14}\text{N}$  WURST-echo spectrum (reconstructed from the first echo of each QCPMG train only) could be simulated with two powder patterns of equal intensity, one for each site type (Fig. 21). The WURST-QCPMG spectrum, however, resembled only the simulation corresponding to the ring sites, which undergo much slower transverse relaxation ( $T_2 = 8 \pm 1$  ms) than the amine sites ( $T_2 = 0.6 \pm 0.1$ ) due to a lack of proximate protons, and thus are selectively enhanced by the QCPMG protocol. Such large variations in  $T_2$  between different structural motifs of nitrogen opens up the possibility of relaxation-based spectral editing.

Finally, the largest  $^{14}\text{N}$   $C_Q$  value yet measured by solid-state NMR was reported by Persons and Harbison, who observed the two sharp discontinuities ( $\nu_{11}/\nu_{22}$ ) in the static powder pattern of the explosive hexamethylene triperoxide diamine [95]. The axial symmetry of the nitrogen site (fixed at  $\eta_Q = 0$  by the symmetry of the crystal structure)

allowed a very accurate determination of the  $C_Q$  from these two spectral features alone ( $C_Q = 5.334$  MHz), representing an example where the limited excitation bandwidth of standard RF pulses was not disadvantageous.

## 5. Magic angle spinning

### 5.1 Narrowband excitation

As outlined in Section 2, many interactions in NMR can be described as second-rank tensor quantities with orientational dependencies denoted by the second-order Legendre polynomial  $\frac{1}{2}(3\cos^2\theta - 1)$ . Such anisotropic interactions can therefore be averaged to zero by spinning the powder sample about an axis oriented at an angle of  $54.74^\circ$  with respect to  $B_0$ . Magic angle spinning (MAS) experiments are commonly used to eliminate heterogeneous broadening due to, for example, dipolar couplings and CSA, resulting in improved sensitivity and resolution. Interactions described by second-rank terms will be averaged to zero if the spinning frequency  $\nu_R$  is much greater than the size of the interaction, leaving a single, isotropic peak (which may itself be broadened by other interactions of higher rank). If  $\nu_R$  is comparable to, or smaller than, the interaction, the isotropic peak (centreband) will be flanked by a series of spinning sidebands separated by  $\nu_R$ , whose manifold reproduces the approximate shape of the static powder pattern [3].

In the case of  $^{14}\text{N}$ , the FOQI is dominant and is usually on the order of MHz. Since MAS speeds rarely exceed 30 kHz,  $^{14}\text{N}$  MAS NMR spectra inevitably consist of a large number of spinning sidebands, themselves broadened by the SOQI, which is only partially averaged by MAS due to fourth-rank terms. Under favorable conditions, such

spectra can provide dramatic improvements in sensitivity and resolution, allowing different nitrogen sites to be distinguished on the basis of differences in chemical and isotropic SOQI shifts, with each site giving rise to a separate sideband pattern. However, for samples with sizeable  $C_Q$ s, the limited bandwidth of the excitation pulse means that the shape of the sideband manifold will be determined by experimental limitations rather than the EFG parameters. Only a fraction of crystallite orientations will be excited, and quantitative spectra will not be possible to obtain from samples containing nitrogen sites with very different  $C_Q$  values. In addition to these issues, the presence of the FOQI means that the spinning sidebands (and centreband) are highly sensitive to the accuracy of the magic angle setting, and a mis-setting of less than  $0.01^\circ$  can cause an observable splitting or broadening. The spinning speed must also remain very stable to avoid the broadening of higher order sidebands. These factors make MAS NMR of  $^{14}\text{N}$  a far more technically challenging experiment than MAS NMR of abundant half-integer quadrupolar nuclei such as  $^{23}\text{Na}$  or  $^{27}\text{Al}$ , where the central transition is unaffected by the FOQI.

Jeschke and Jansen were the first authors to publish  $^{14}\text{N}$  MAS NMR spectra, reporting spinning sideband patterns for the cubic and hexagonal phases of boron nitride obtained at a reported MAS rate of 12 kHz (Fig. 22) [96]. The former phase shows an isotropic line at  $\delta_{\text{iso}} = -17.6$  ppm with a width of just 90 Hz due to its highly symmetric environment (Fig. 22a). The small sidebands were attributed to heteronuclear dipolar couplings with boron. For the hexagonal phase, a complete spinning sideband pattern with visible quadrupolar splittings was observed. This pattern was simulated, assuming axially symmetric and coincident tensors, to obtain the EFG and CS parameters (Fig. 22b and c). The relatively small  $C_Q$  (140 kHz) allowed the full sideband pattern to be excited

using a 2  $\mu$ s RF pulse. Interestingly, the CSA could be measured ( $\delta_{\text{iso}} = 63$  ppm and  $\Delta_{\text{CS}} = 160$  ppm) despite being smaller than the MAS rate, due to the observable effect it had on the sideband manifold (*i.e.*, breaking the mirror symmetry of the pattern). The capability of accurately measuring  $^{14}\text{N}$  CSA as well as EFG parameters is one of the primary advantages of  $^{14}\text{N}$  MAS NMR over static experiments. A second  $^{14}\text{N}$  MAS NMR study, published in the same year, included spectra obtained from hexagonal boron nitride as well as aluminium nitride [97]. In the latter, the  $C_Q$  is very small ( $< 10$  kHz), and the 1.5 kHz MAS spectrum gave a Gaussian-like manifold of sharp sidebands.

Fung and co-workers subsequently proposed various experimental and processing strategies for  $^{14}\text{N}$  MAS NMR, testing these methods on mixtures of ammonium chloride, potassium nitrate and lead nitrate to provide a range of chemical shifts and  $C_Q$  values [98]. They noted that MAS spectra can be split into sections of width  $\nu_R$ , which can then be co-added such that sideband intensities are added onto the centrebands. This not only increases the S/N of the centrebands but also makes their intensities more quantitative (rotor-synchronized acquisition could potentially be used to achieve the same goal). For samples with large  $C_Q$ s where the identity of the centreband may not be obvious, the spectra can be acquired at multiple spinning rates and then combined by co-addition or multiplication. Since the centreband position is invariant to changes in  $\nu_R$ , it will be selectively enhanced (varying the MAS rate is a common strategy used to identify the isotropic shifts in MAS NMR of spin-1/2 nuclei with large CSAs). The authors also discussed various processing strategies involving digital filters to suppress spinning sideband intensities. In a follow-up paper, they described the narrowband excitation of large- $C_Q$  samples, demonstrating the extreme sensitivity of the sideband lineshapes to the

spinning angle [99]. It was noted that the various interaction parameters can in principle be ascertained directly from these sideband shapes if the spinning angle is known precisely. The effects of the SOQI on the MAS linewidths and positions were also considered. For samples spinning at the exact magic angle, this interaction causes the isotropic SOQI shift as well as a broadening of the sidebands. The latter effect can actually be reduced by the narrow excitation bandwidth of RF pulses applied near the centreband, since only crystallite orientations with  $V_{33}$  aligned at or near the magic angle (*i.e.*, with small quadrupolar perturbations) are excited. Consequently, while the use of long, low power pulses can enhance the intensity of the centreband/sideband to which they are applied, that peak will also experience more SOQI broadening due to the wider range of crystallite orientations excited. The effects of the isotropic SOQI shift prompted the authors to suggest a strategy for measuring EFG parameters from samples whose full spinning sideband patterns are too broad to observe. Using previously determined isotropic chemical shifts (from  $^{15}\text{N}$  NMR), the term  $C_Q^2(3 + \eta_Q^2)$  can be measured directly from the SOQI shift. In a subsequent study of a range of nitrates, Marburger *et al.* showed that both chemical shifts and EFG parameters can be ascertained by observing only the  $^{14}\text{N}$  MAS centreband at two fields (as outlined in Section 2, shielding contributions to the shift are proportional to  $B_0$ , while the SOQI shift is inversely proportional to  $B_0$  and is  $C_Q$ -dependent) [100]. Such an approach does not require the observation of any sidebands, thereby overcoming experimental bandwidth limitations. However, as well as the loss in sensitivity due to the narrowband excitation, this approach requires the ratio between the MAS-averaged and maximum SOQI shift to be known, and

the authors determined this for their nitrate samples using  $C_Q$  values previously obtained by other techniques.

Most other reported  $^{14}\text{N}$  MAS NMR studies are of nitrogen environments with high symmetry and correspondingly small  $C_Q$  values. Bräuniger *et al.* studied impurity phases in sialon ceramics [101]. In most ceramics, nitrogen sites feature relatively large  $C_Q$ s, but in these samples a highly symmetric nitrogen site was observed, identified as belonging to aluminum nitride, which was used as one of the precursor materials.  $^{14}\text{N}$  MAS NMR has also been used to study oxygen substitution by nitrogen in barium titanate [102], while Yesinowski and co-workers studied various gallium nitride samples [103,104]. In both cases the cubic structure of the samples resulted in very narrow linewidths. Finally,  $^{14}\text{N}$  MAS NMR has also been used to study oriented systems such as lipid membranes, and this application is discussed in Section 7.

## 5.2 Broadband excitation

Jakobsen and co-workers took a different approach to  $^{14}\text{N}$  MAS NMR, focusing on technological improvements to provide highly stable MAS settings and increased excitation and detection bandwidths. In particular, they used a system wherein the air used for the MAS drive and bearing gas is first cleaned by filters, then dried, then passed through ballast tanks to provide a very stable final pressure [105]. This set-up allows for MAS rates that remain stable to within 0.1 Hz. Their first publication presented a spectrum obtained from potassium nitrate (Fig. 23), which consisted of a very broad manifold of spinning sidebands spanning a frequency range of over 600 kHz [106]. An extremely high S/N was achieved in an experiment time of 33 hours using single-pulse

excitation, allowing an accurate simulation not just of the spinning sideband intensities but also their individual lineshapes (Fig. 24). This simulation was carried out with a modified version of the STARS software developed previously to analyze satellite transition MAS spectra from half-integer quadrupolar nuclei [107]. In addition to the quadrupolar interaction and CSA (known from  $^{15}\text{N}$  experiments), second-order cross terms [108] between these interactions were included, as well as the effects of various experimental factors such as the limited probe bandwidth and small deviations from the magic angle. Thus, by fitting the simulation to this single spectrum, the authors could measure the isotropic chemical shift ( $\delta_{\text{iso}} = 342.7$  ppm), the EFG parameters ( $C_Q = 746$  kHz,  $\eta_Q = 0.02$ ) and also the precise spinning angle (a  $-0.009^\circ$  deviation from the exact magic angle).

This general approach proved to be a robust method for probing nitrogen sites with  $C_Q$  values  $\leq ca.$  1.2 MHz, and Jakobsen and co-workers subsequently published a series of  $^{14}\text{N}$  MAS NMR papers on a range of systems. For example, using the variation in frictional heating of the MAS rotor at various spinning rates, they studied a phase transition in ammonium nitrate (phase IV to III at  $35^\circ\text{C}$ ) [109]. Both the  $\text{NH}_4^+$  and  $\text{NO}_3^-$  ions were observed, and the authors made use of a fully  $^{15}\text{NH}_4^+$  enriched sample to resolve the individual sites, since the sidebands for each species overlap. Changes in the EFG parameters and isotropic shifts occurred for both species at the phase transition, and a hysteresis in the transition was observed. Elsewhere,  $^{14}\text{N}$  CS parameters for some tetralkylammonium halides were measured from the MAS spectra, with  $^1\text{H}$  decoupling applied [110]. The relatively small CSAs (a few tens of ppm) caused significant asymmetries in the  $^{14}\text{N}$  spinning sideband manifolds, and careful experimental

optimization proved that such asymmetries were not experimental artifacts. Natural abundance  $^{15}\text{N}$  CP MAS experiments were also carried out to confirm these findings. Such small CSAs can be observed in  $^{14}\text{N}$  MAS spectra at spinning speeds where they would be unobservable by  $^{15}\text{N}$  MAS. This is because the anisotropic CS interaction affects the two  $^{14}\text{N}$  transitions differently, resulting in a difference in transition widths described by a factor of  $3\Delta_{\text{CS}v_0}$  (see Eq. (9) and Fig. 4c). This effectively amplifies the effects of the CSA on the  $^{14}\text{N}$  spectrum [110]. The nitrogen CSA in lead nitrate could also be extracted from the individual sideband lineshapes in its  $^{14}\text{N}$  MAS spectrum [111]. In this case, the sideband shapes were very sensitive to the second-order quadrupolar-CSA cross-terms, which have time-independent parts not averaged by MAS (Fig. 25). Deviations in spinning angles of the order of  $0.002^\circ$  also showed visible differences in the sideband shapes (Fig. 25).

In applying this method to study various amino acids, the authors chose not to apply  $^1\text{H}$  decoupling since they noted that the removal of the low-pass filters on the  $^{14}\text{N}$  channel lowered the apparent quality factor of the probe, effectively increasing its bandwidth and reducing the attenuation of higher order spinning sidebands [112]. Thus, sideband manifolds with widths well in excess of 1 MHz were obtained from these samples, allowing  $C_{\text{QS}}$  of up to 1.2 MHz to be measured (Fig. 26). For several of the amino acids, simulations of the two distinct nitrogen environments in the crystal structures could be fitted simultaneously despite significant overlap of the sidebands, allowing the extraction of individual sets of isotropic shifts and EFG parameters. The authors also discussed the optimization of equipment such as RF cable lengths to maximize the bandwidth and eliminate tilts in the sideband manifolds.

In a study of caesium nitrate, the authors used density functional theory (DFT) calculations to refine the crystal structure in light of the measured  $^{14}\text{N}$  EFG parameters [113]. The three different nitrate ions in the asymmetric unit cell give rise to three sets of overlapping sidebands, which were fitted to a simulation using a single set of (average)  $^{14}\text{N}$  parameters. These parameters compared poorly with values calculated from a crystal structure, but after optimization of the atomic positions using DFT (with fixed lattice parameters), the predicted values matched the experimental parameters far more closely, thereby confirming the accuracy of the newly optimized structure. In a further  $^{14}\text{N}$  MAS NMR study of tetraalkylammonium salts, this time with multiple sites and larger  $C_Q$  values, the importance of the spinning rate was highlighted [114]. A MAS spectrum of trimethylbenzylammonium chloride recorded at a spinning rate of 6 kHz could be fitted accurately with a single site, but at 1 kHz the presence of two distinct sites became clear, and was subsequently confirmed by X-ray diffraction (XRD). The use of slower MAS rates results in a larger number of sidebands, and is therefore preferable to distinguish different sites with similar EFG parameters, although this obviously comes at a cost of a reduced S/N. Jakobsen's group has also published  $^{14}\text{N}$  MAS NMR studies of ammonium molybdates [115], including a study of the decomposition pathway of  $(\text{NH}_4)_2\text{MoO}_4$ , and of solid solutions of ammonium and alkali metal tetrathiotungstates [116]. In the latter system, a Gaussian distribution in EFG parameters was used in the simulations to account for translational disorder, and it was shown that the ammonium ions sit preferentially on one of the two crystallographic alkali metal sites, the specific sites being identified with the aid of DFT calculations.

Finally, Larsen has carried out numerical simulations of the effects of various types of molecular dynamics on  $^{14}\text{N}$  MAS NMR spectra of samples with large  $C_Q$  values [117]. The author noted that, just as with  $^{14}\text{N}$  MAS spectra in the absence of dynamics, the second-order quadrupolar interaction, CSA and magic angle setting can each play a crucial role in determining the nature of dynamically-averaged spectra. The advantages of rotor-synchronized acquisition were also highlighted.

## 6. Overtone spectroscopy

While both of the fundamental  $^{14}\text{N}$  transitions are susceptible to first-order quadrupolar broadening, the  $+1 \leftrightarrow -1$ , or “overtone” transition is not (Fig. 1). The idea behind overtone spectroscopy is therefore to observe the spectrum arising from this  $\Delta m = 2$  transition, which, since it is only affected by the quadrupolar interaction to second order, will result in far narrower lineshapes, thus improving the spectral resolution and decreasing the overall spectral width. These advantages are analogous to those of the double-quantum  $^{14}\text{N}$  experiment mentioned in Section 4.1, however, in overtone spectroscopy the  $+1 \leftrightarrow -1$  transition is observed *directly*. The frequency of the overtone resonance occurs at approximately  $2\nu_0$  (with an additional shift due to the SOQI and chemical shifts), which also reduces the effects of acoustic ringing.

An overtone NMR signal was first observed from  $^{14}\text{N}$  by Creel *et al.*, who studied a sample of hexamethylenetetramine (HMT) using CW NMR [118]. They showed that the overtone signal frequency was equal to the sum of the individual fundamental frequencies as would be expected. In most NMR applications, any  $\Delta m > 1$  transitions are usually forbidden, but Bloom and LeGros noted that the  $^{14}\text{N}$  overtone transition is

allowed when the FOQI becomes comparable in size to  $\nu_0$ . In such a situation, the large non-secular terms of the quadrupolar Hamiltonian cause the high field approximation to break down and result in a tilting of the spin quantization axis away from  $B_0$  [119]. Bloom and LeGros proposed a pulsed experiment to observe the overtone signal using transverse radiation applied at  $\nu_0$  and detection of the longitudinal signal at  $2\nu_0$ . They showed that the observed signal comprises a fraction  $f$  of the equilibrium magnetization, where  $f$  is proportional to  $C_Q/\nu_0$  and is also a function of the orientation of the EFG relative to  $B_0$ . The authors noted that despite the decrease in  $f$  with increasing  $B_0$ , both the equilibrium polarization and the voltage induced in the detection coil increase with  $B_0$ , so the experiment is best conducted at the highest possible field. They applied the experiment to a single crystal of sodium nitrite, observing both the single-quantum and overtone FIDs. The overtone FID showed a decay time approximately three orders of magnitude longer than that of the fundamental transitions due to the absence of the FOQI.

Aside from requiring two channels (tuned at  $\nu_0$  and  $2\nu_0$ ), the main limitation of the method proposed by Bloom and LeGros is that the net overtone signal from a powder sample is zero due to the cancellation of signals from all EFG orientations [119]. However, the authors noted that overtone spectroscopy from powder samples should be possible using direct excitation at  $2\nu_0$ , and very soon afterwards this was demonstrated by Tycko and Opella, who presented both single-crystal and powder overtone  $^{14}\text{N}$  spectra from *N*-acetylvaline (NAV) [120]. These spectra were obtained using Jeener-Broekaert cross-polarization [121] from  $^1\text{H}$  directly to the  $^{14}\text{N}$  overtone transition, with  $^1\text{H}$  decoupling applied and experimental configurations with the RF coil oriented both perpendicular and parallel to  $B_0$ . The resultant single-crystal overtone spectra showed

linewidths of *ca.* 200 Hz, and the powder pattern widths were of the order of 50 kHz. In comparison with spectra obtained from the fundamental  $^{14}\text{N}$  transitions, such linewidths correspond to reductions of one and two orders of magnitude respectively. The powder patterns were shown to be sensitive to the SOQI, the CSA and the configuration of the RF coil (Fig. 27).

The same authors subsequently presented a more detailed discussion of their methods, including a theoretical treatment of overtone spectroscopy using perturbation theory [122]. They compared various cross-polarization schemes including Jeener-Broekaert, ADRF and pulsed spin-locking. The first two methods achieve cross polarization from  $^1\text{H}$  dipolar order rather than spin-locked magnetization, have less strict Hartman-Hahn match requirements and require a smaller  $B_1$  on the  $^{14}\text{N}$  channel. This latter factor is important because overtone nutation frequencies are relatively slow (effective RF fields applied to the overtone transition are scaled down from those applied to fundamental transitions by a factor of  $C_Q/\nu_0$ ). Cross-polarization signal enhancements of up to 5.9 were achieved, with additional phase-shifted “postpulses” used to compensate for off-resonance effects, increasing the cross-polarization bandwidth. The authors also discussed two-dimensional pulse sequences in which the overtone transition moments and heteronuclear dipolar splittings (which are twice as large in overtone spectroscopy due to the doubled gyromagnetic ratio of the overtone transition) can be correlated with the overtone spectra in the second dimension. The latter experiment is similar to the SLF experiments mentioned in Section 3. Each of these techniques was demonstrated on a single-crystal of L-alanyl-glycylglycine, which features four distinct overtone resonances [122].

In the same article, the authors also discussed overtone powder patterns [122]. Crucially, the orientation dependence of the overtone excitation is dependent on the experimental set-up, the specifics of the pulse sequence, and also on the dipolar coupling network if cross-polarization is used, all factors that can make overtone powder patterns difficult to model. The authors showed examples of "ideal" lineshapes (assuming uniform excitation, which in practice is not achieved), and gave expressions relating the frequencies of the discontinuities to the EFG parameters. Simulations that more closely match the experimental lineshapes can be reproduced from these ideal lineshapes by weighting the signals from the various crystallite orientations by their transition moments. More discontinuities are observed when the RF coil is parallel to  $B_0$  than when it is perpendicular, and the former configuration also tends to increase the pattern width, thus complicating spectra if multiple sites are present. Some preliminary overtone experiments on samples spinning at various angles with respect to  $B_0$  were also presented. No MAS-like reduction in linewidths was observed, but the lineshapes and discontinuity positions were shown to be sensitive to the spinning conditions.

Tycko, Opella and co-workers went on to develop strategies employing  $^{14}\text{N}$  overtone spectroscopy in the determination of plane orientations and torsion angles in peptides [123]. Studying a single crystal of NAV at an arbitrary orientation with respect to  $B_0$ , the authors measured first-order quadrupolar splittings, "overtone shifts" (the combination of the isotropic SOQI shift and chemical shift with respect to  $2\nu_0$ ) and dipolar splittings for the two sites from both the fundamental and overtone spectra. The overtone nutation frequencies were also measured by calibrating the RF field strengths on single-quantum  $^2\text{H}$  signals, which are close in frequency to the  $^{14}\text{N}$  overtone transition.

Each of these quantities has a distinct dependence on the peptide plane orientation, defined by the polar angles  $\chi$  and  $\psi$ . By plotting the restraints on these angles imposed by the various experimental measurements, the  $\chi$  and  $\psi$  values were narrowed down to eight absolute orientations for each molecule (the symmetry of the interactions resulting in multiple solutions). The correct values were then chosen from these by a consideration of the symmetry of the crystal structure. Such an analysis requires a knowledge of the  $^{14}\text{N}$  EFG tensor parameters and its orientation in the peptide plane, which can be ascertained using the methods outlined in Section 3, or also by overtone spectroscopy [124]. In this way the authors determined peptide plane orientations for the two molecules in the NAV crystal that were in excellent agreement with the XRD structure.

Opella and co-workers subsequently used overtone spectroscopy to study other model peptides [125] and to determine torsion angles between peptide planes [126]. They reported specifications for a low-temperature double-resonance  $^1\text{H}$ - $^{14}\text{N}$  probe designed specifically for such experiments, showing that cryogenic temperatures can give a considerable signal boost for overtone experiments on both powder and single crystal samples [127]. In addition, they described several other interesting applications of  $^{14}\text{N}$  overtone irradiation. For example, they showed that the irradiation of  $^{14}\text{N}$  overtone resonances can lead to line-narrowing in  $^{13}\text{C}$  spectra by eliminating  $^{14}\text{N}$ - $^{13}\text{C}$  dipolar couplings. This results in  $^{13}\text{C}$  doublets, since the  $^{13}\text{C}$  nuclei remain coupled to spins on the central level of  $^{14}\text{N}$  [128]. Since the  $^{14}\text{N}$  overtone resonances in single crystals are narrow, they can be selectively irradiated using low powers and  $^{13}\text{C}$  sites can therefore be selectively decoupled, aiding spectral assignment. A homonuclear  $^{14}\text{N}$  overtone spin exchange experiment was also presented, allowing measurement of nitrogen-nitrogen

distances [129]. The pulse sequence used in the latter experiment involves the excitation and storage of the overtone magnetization parallel to  $B_0$ , where spin exchange occurs between nitrogen sites *via* homonuclear dipolar couplings. Cross-peaks intensities then depend on the spin exchange efficiency (*i.e.*, the strength of the dipolar coupling), which is orientation dependent. The experiment was demonstrated on a single crystal of NAV at 90K, the low temperature providing long spin-lattice relaxation times, thereby allowing a very long mixing time (30 s). Correlations between nitrogen sites at distances of over 5 Å were observed, which is longer than typical nitrogen-nitrogen distances in proteins. Finally, heteronuclear correlation experiments in which the  $^1\text{H}$  spectra are detected indirectly *via* the  $^{14}\text{N}$  overtone signals were described, allowing asymmetric  $^1\text{H}$  triplets (caused by dipolar couplings to  $^{14}\text{N}$ ) to be resolved and correlated with the  $^{14}\text{N}$  signals [130]. Homonuclear Lee-Goldburg proton decoupling is used during the evolution period, with heteronuclear decoupling applied during detection on the  $^{14}\text{N}$  channel. The asymmetric  $^1\text{H}$  triplets are resolved (Fig. 28), from which the  $^1\text{H}$  chemical shifts and  $^1\text{H}$ - $^{14}\text{N}$  dipolar couplings can be measured.

Because of the slow nutation rates of overtone transitions, the RF excitation pulses generally need to be long and thus have narrow excitation bandwidths. Lee and Ramamoorthy therefore investigated the use of composite  $\pi/2$  excitation pulses for overtone excitation [131]. Composite pulses can offer broad excitation bandwidths at relatively low RF powers [132], and were shown to provide approximately double the excitation bandwidth of regular pulses in  $^{14}\text{N}$  overtone experiments. They are also less sensitive to RF power miscalibrations than standard pulses. The same authors also carried out an extensive investigation of an overtone cross-polarization scheme (a Jeener-

Broekaert sequence with a postpulse, as previously used by Opella and co-workers) [133]. They determined the optimal values for the Jeener-Broekaert inter-pulse delay time, the  $^{14}\text{N}$  spin-lock power and duration, and the postpulse length, and showed that a ramped-amplitude spin-lock field on  $^{14}\text{N}$  is advantageous. Finally, they investigated the use of off-resonance proton decoupling for measuring  $^1\text{H}$ - $^{14}\text{N}$  dipolar couplings in a single-crystal sample of NAV [134]. After selective cross-polarization to one of the overtone resonances, a Lee-Goldburg homonuclear decoupling field is applied to the protons at the magic angle, which has the effect of scaling the heteronuclear dipolar couplings by a factor of 0.58. This allows the dipolar splittings to be resolved in the  $^{14}\text{N}$  overtone spectrum with a resolution similar to SLF experiments (Fig. 29), but with the advantage of a faster experiment time (since the experiment is one-dimensional). The authors named the experiment DIPOTSHIFT (dipolar overtone shift) [134].

Frydman and co-workers presented a detailed theoretical description of overtone spectroscopy for both static and spinning samples using a density matrix formalism [135]. Treatment of the Liouville-von Neumann equation is complicated by the fact that non-secular terms play a crucial role in overtone spectroscopy, so cannot be neglected, necessitating the use of a tilted reference frame in which the quadrupolar-perturbed Hamiltonian can be diagonalized. This frame is dependent on the EFG orientation and the relative sizes of  $C_Q$  and  $\nu_0$ , a dependency which carries over into the Hamiltonian describing the RF excitation, and results in a scaling down and orientation dependency of the effective RF field (hence the slow overtone nutation rates). The authors used this treatment to determine the optimum settings for overtone excitation pulses, showing that the signal intensities from powder samples can be increased by offsetting the transmitter

frequency from  $2\nu_0$ , and that a high RF field strength is desirable. They also discussed the overall relative sensitivity of overtone spectroscopy, estimating that under optimal excitation conditions the signal that can be obtained in an overtone experiment is of the order of 1 or 2 % of that which would be obtained from a single-quantum experiment in which the quadrupolar interaction was absent.

In the same paper, sample rotation strategies to reduce or remove the SOQI broadening from overtone powder patterns were also investigated [135]. Previous experimental [122] and theoretical [136] investigations had suggested that the use of sample spinning to reduce overtone powder pattern widths was far from straightforward. Frydman's density matrix analysis predicts that sample spinning at any angle will not remove this broadening and can actually increase linewidths and complicate spectra by giving rise to overlapping sideband features at  $\pm n\nu_R$  [135]. An exception occurs when the spinning axis is parallel to  $B_0$ , wherein sidebands are absent and the powder pattern has the same shape as the static case but is shifted by  $\nu_R$ . The possibility of dynamic angle spinning (DAS) [137] overtone spectroscopy was also considered, with the overtone signal stored parallel to  $B_0$  while the spinning angle is altered. The complementary DAS angles of  $63^\circ$  and  $0^\circ$  were shown to be the only feasible combination of angles ( $0^\circ$  for the direct acquisition dimension, for which sideband features do not occur), with other angles producing complex sideband patterns in both dimensions.

In a second paper, Frydman and co-workers considered the possibility of recoupling dipolar interactions under MAS using overtone irradiation [138]. Since the  $^{14}\text{N}$  overtone nutation frequencies can be in the kHz regime, they can interfere with the MAS averaging of dipolar couplings. Sidebands in the overtone nutation frequencies that

are spaced at intervals equal to the rotor frequency can further boost the recoupling efficiency. These schemes were therefore referred to as overtone rotary recoupling (ORR), and various pulse sequences in which this can be implemented were considered, with dephasing curves simulated for a range of experimental conditions. The authors noted that the dephasing fractions (observed *via*  $^{13}\text{C}$  nuclei) map out the  $^{14}\text{N}$  overtone powder pattern lineshapes as a function of overtone radiation offset. Two-dimensional experiments can then be carried out to correlate  $^{13}\text{C}$  chemical shifts with  $^{14}\text{N}$  overtone powder patterns of proximate nitrogen sites. Since different types of nitrogen sites have different EFG parameters and thus different overtone patterns, selective recoupling of specific nitrogen environments is possible, and such indirect detection of overtone spectra can also improve the overall sensitivity. The detection of  $^{14}\text{N}$  overtone signals using  $^1\text{H}$  nuclei was demonstrated experimentally by Garroway and Miller [139], while Takegoshi and co-workers successfully demonstrated  $^{13}\text{C}$ -detected  $^{14}\text{N}$  overtone spectroscopy on powder samples of NAV and L-alanine [140]. The latter authors went on to use this approach to study amide nitrogen  $C_{\text{QS}}$  in alpha helices and beta sheets [141], showing that  $C_{\text{QS}}$  in the former environments are a few hundred kHz larger than in the latter.

Elsewhere, Grandinetti discussed phase cycling in overtone experiments (and other situations involving a tilted reference frame), concluding that standard phase cycling schemes are applicable [142]. Trease and Grandinetti also developed improved theoretical methods for calculating overtone spectra [143], observing that lower  $B_0$  values result in faster overtone nutation frequencies (improving excitation bandwidths), while higher values of  $B_0$  result in a larger maximum attainable signal at a given RF field strength. They also noted that sample spinning results in a decrease in overall sensitivity,

with faster spinning rates not providing any improvement. Kuwahara reported a method for recoupling  $^{14}\text{N}$  under MAS using WURST pulses applied at the overtone frequency, which show a more uniform recoupling capability with respect to offset frequency than a standard overtone pulse [144]. The same author also presented a theoretical investigation into the feasibility of overtone spectroscopy for half-integer quadrupolar nuclei [145]. Finally, Jayanthi and Ramanathan have discussed the use of a dipolar assisted polarization transfer (DAPT) pulse sequence as a means of  $^{14}\text{N}$  overtone signal enhancement in single crystals with relatively low RF power requirements on the  $^{14}\text{N}$  channel [146].

## **7. Aligned systems**

This section describes  $^{14}\text{N}$  NMR experiments carried out on samples that are neither crystalline solids nor isotropic liquids, but consist of molecules that are preferentially aligned. In an isotropic solution,  $^{14}\text{N}$  lineshapes for samples with non-zero EFGs are broadened due to relaxation induced by the rapid modulation of the quadrupolar interaction. Since Brownian motion causes all EFG orientations to be sampled with equal probability, the lineshapes are featureless and quadrupolar splittings are absent. However, if certain EFG orientations are preferentially sampled, either due to the nature of the molecule or due to externally-imposed conditions, an observable quadrupolar splitting can arise. Even for nitrogen sites with relatively large  $C_Q$  values, the size of this splitting will often be reduced to the order of kHz by dynamical averaging, and thus the spectra can be observed relatively easily. Since the extent of this averaging

will depend on the exact rate and geometry of the motion, the quadrupolar splitting can be used as a direct probe of the dynamics of the system.

The first observation of such dynamically-averaged quadrupolar splittings in  $^{14}\text{N}$  spectra was reported by MacLean and co-workers, who studied polar liquids that were partially aligned under an applied electric field (the quadrupolar electric field effect). The splittings were observed using CW NMR in liquid nitrobenzene and nitromethane [147], and later in other solutions [148] and their mixtures [149]. Partial alignment of small molecules can also be induced using a liquid crystal (LC) solvent. Yannoni indirectly measured the  $^{14}\text{N}$   $C_Q$  and CSA from methylisocyanide dissolved in a nematic LC *via* the  $^1\text{H}$  nuclei using the “spin-tickling” method [150]. Other authors later directly observed  $^{14}\text{N}$  quadrupolar splittings from various small molecules in different LC phases [151-156]. Studies of tetrahedral ions such as ammonium and tetramethylammonium dissolved in lyotropic mesophases resulted in observable quadrupolar splittings of several hundred Hz, indicating both a distortion of the ion and contributions to the EFG from surrounding ionic charges and molecular dipoles [157-159]. Moran and co-workers have observed  $^{14}\text{N}$  quadrupolar splittings from  $\text{NH}_4^+$  and  $\text{NO}_3^-$  ions in cation-exchange membranes [160,161], and more recently, Pellizer and Asaro carried out  $^{14}\text{N}$  NMR experiments on  $\text{N}_2$  dissolved in a lyotropic mesophase [162], observing a quadrupolar splitting which allowed a measurement of the lyotropic order parameter as a function of sample composition.

Liquid crystal mesophases themselves, and related systems such as lipid bilayers, are commonly studied using nuclei such as  $^1\text{H}$ ,  $^2\text{H}$  and  $^{13}\text{C}$ .  $^{14}\text{N}$ , however, can offer specific advantages over each of these nuclei. While  $^{14}\text{N}$  has a much weaker inherent

signal than that of  $^1\text{H}$ , it has the advantage of having far fewer unique sites in each molecule, as well as having relaxation and spectral characteristics that are dominated by the quadrupolar interaction, thus making results easier to model and interpret. It also has advantages over  $^2\text{H}$  and  $^{13}\text{C}$  in terms of natural abundance, which is especially significant for the study of samples of biological origin. Cabane and Clark were the first authors to employ  $^{14}\text{N}$  NMR to study liquid crystal molecules, observing quadrupolar splittings in the nematic phase of para-azoxyanisole [163]. The splittings for the two different nitrogen sites in the molecule were shown to be proportional to the order parameter  $S = \langle \frac{1}{2}(3\cos^2\theta_s - 1) \rangle$  (where  $\theta_s$  is the angle between the molecular axis and the director). The same authors subsequently investigated the smectic-A to nematic phase transition in 4-nitrile-benzilidene-*p*-N-octyloxyaniline [164]. By observing the temperature dependence of the order parameter, they showed that this was a second-order phase transition.

In addition to dynamically-averaged quadrupolar splittings,  $^{14}\text{N}$  relaxation times can also provide information on ordering and dynamics in mesophases, and  $^{14}\text{N}$  relaxation experiments have been used to study isotropic LC phases [165]. Henriksson *et al.* carried out a  $^{14}\text{N}$  relaxation study of surfactant molecules in a micellar solution of *n*-hexadecyltrimethylammonium bromide ( $\text{C}_{16}\text{TAB}$ ) and chloride, also providing a theoretical description of relaxation in such systems [166]. The authors observed two motional regimes: fast reorientation about the molecular axis, and a much slower diffusion of the molecule around the micelle. They derived explicit expressions for the relaxation rates, allowing the fast and slow correlation times to be estimated. The formation of rod-shaped micelles in  $\text{C}_{16}\text{TAB}$  was inferred by the observation of a rapid

increase in correlation time for the molecular diffusion with increasing surfactant concentration. Eriksson, Lindblom and co-workers used this approach to study other LC systems [167-171]. Meanwhile, Koga and Kanazawa studied sonicated DPPC and egg yolk phosphatidylcholine (EPC) bilayer vesicles, which gave relatively narrow Lorentzian  $^{14}\text{N}$  lineshapes caused by fast motional narrowing due to the reorientation of the vesicles (Fig. 30) [172,173].  $T_1$  and  $T_2$  relaxation times were measured and used to characterize the slow (vesicle rotation/lateral molecular diffusion) and fast (intramolecular motion) regime dynamics, including an estimation of the lateral diffusion coefficient. They also studied EPC headgroup dynamics in various solvents using the same methods [174,175].

Lipid bilayers formed by amphiphilic molecules such as those mentioned above are commonly used as model systems that mimic naturally-occurring biological membranes. Siminovitch *et al.* also studied DPPC using  $^{14}\text{N}$  NMR, and observed a first-order quadrupolar powder pattern (Fig. 31) [45], in sharp contrast to the narrow Lorentzian lineshapes observed by Koga and Kanazawa (Fig. 30). The reason for this dramatic difference in spectra lies in the macroscopic organization of the DPPC molecules. In Koga and Kanazawa's study, the DPPC had been sonicated, forming spherical micelles which undergo rapid isotropic rotation and average out the quadrupolar splittings entirely. Siminovitch's unsonicated DPPC sample instead formed lamellar bilayers in which the molecules exhibit a preferential orientation and the quadrupolar splittings are retained. The latter work therefore provided a powerful demonstration of the potential of wide-line  $^{14}\text{N}$  NMR as a probe of membranes. Nitrogen is present in the headgroups of many phospholipids, which undergo fast rotational diffusion about an axis

normal to the bilayer plane, hence  $^{14}\text{N}$  splittings are significantly motionally averaged and can be narrow enough to observe easily, with the quadrupolar splitting providing a direct measure of the order parameter for the  $^{14}\text{N}$  EFG principal axis. Siminovitch *et al.* found splittings on the order of 10 kHz in DPPC, indicating a very small order parameter for the headgroups. Since the quadrupole splitting is dependent on both the order parameter  $S$  and the  $C_Q$  in the static molecule, it is important that the latter quantity be accurately estimated (in this case it was deduced as *ca.* 135 kHz by a consideration of  $^2\text{H}$  NMR data, and is relatively low due to the almost tetrahedral nature of the  $\text{C-N}(\text{CH}_3)_3$  group). The authors also observed the gel-to-LC phase transition as a decrease in the quadrupolar splitting at  $41^\circ\text{C}$ . In a follow-up study, Siminovitch and Jeffery used a similar approach to study bovine sphingomyelin [176]. The quadrupolar splitting in the LC phase of sphingomyelin is less than in DPPC, indicating a difference in orientational ordering (a smaller order parameter in the former). The amide nitrogen in sphingomyelin has a much larger  $C_Q$  (*ca.* 3 MHz) than the choline nitrogen, thus was too large to be excited by the quadrupolar echo pulse sequence, making the experiment choline-selective.

Rothgeb and Oldfield published a similar study investigating the incorporation of various species into dimyristoyl phosphatidylcholine (DMPC) bilayers, interpreting changes in the observed quadrupolar splittings as changes in headgroup conformation and mobility [46]. For example, the incorporation of the drug desipramine, which carries a positive charge and intercalates into the headgroup region, had the effect of reducing the quadrupolar splitting, interpreted as a disordering of the bilayer. The addition of the  $\text{Eu}^{3+}$  cation appeared to cause a gel phase-like spectrum, though this result was subsequently better explained by Siminovitch (*vide infra*). The presence of high levels of the antibiotic

polypeptide gramicidin led to the formation of a broad anisotropic feature, while the incorporation of large proteins only slightly perturbed the bilayer. The authors also showed that the addition of cholesterol to various lipid bilayers had the effect of preventing the LC-to-gel phase transition.

Subsequently, Siminovitch and co-workers carried out further  $^{14}\text{N}$  studies of bilayers. They observed changes in both the orientation and dynamics of the headgroups in DPPC as the N-P distance was varied by incorporating additional  $\text{CH}_2$  groups [177]. In an investigation of the effects of ions and anesthetics, they found that paramagnetic ions such as  $\text{Eu}^{3+}$  led to significant asymmetries in the  $^{14}\text{N}$  patterns [178]. Such asymmetries were not observed by Rothgeb and Oldfield because of their use of single phase (rather than quadrature) detection [46]. Siminovitch *et al.* published a detailed discussion of these asymmetric spin-1 NMR patterns, which result from the coupling of the quadrupolar nucleus with the paramagnetic moment of the ions, a dipolar interaction that can be similar in size to the FOQI [179]. They used a density matrix approach to derive expressions for this interaction, allowing simulation of the distorted lineshapes and determination of paramagnetic shifts, and also discussed a pulse sequence capable of refocusing the dipolar terms.

The above publications spurred an increase in the use of  $^{14}\text{N}$  NMR as a probe of LCs, lipid bilayers and related systems, with a number of reports studying  $^{14}\text{N}$  linewidths and relaxation [180-191], and others investigating quadrupolar splittings [192-210]. More recently, Ramamoorthy and coworkers have studied transmembrane, channel-forming peptides, as well as antimicrobial peptides which locate on the bilayer surface, and showed that the latter peptides decreased the observed quadrupolar splittings

(indicating a change in the membrane surface potential) while the channel-forming peptides did not, opening up the possibility of using this approach to probe the location and orientation of proteins with respect to the membrane [211].

The first application of  $^{14}\text{N}$  MAS experiments to membrane systems was reported by Lindström *et al.* as part of a multi-technique study of amyloid- $\beta$  (A- $\beta$ ) peptides in various membranes [212]. The authors used the quadrupolar splittings to probe the electrostatic potential of the membrane surface. Since the phosphatidylcholine headgroups are polar with a negatively charged phosphate group and positively charged choline group, they will tend to align if an electrostatic potential is present at the membrane surface (this is sometimes referred to as the “molecular voltmeter” effect). Since A- $\beta$  peptides do not bind to neutral membranes like pure DMPC, some cationic didodecyldimethylammonium bromide (DDAB) was also included.  $^{14}\text{N}$  signals from each of the amphiphilic species could be resolved in both the static and MAS spectra. Addition of the A- $\beta$  protein resulted in a reduction in the quadrupolar splitting, corresponding to a tilt in the  $\text{P}^-$ - $\text{N}^+$  vector away from the membrane surface due to partial compensation of the negative charge from the DDAB by the positive charge of the protein. The isotropic  $^{14}\text{N}$  MAS linewidths also increased due to a restriction in the headgroup dynamics. MAS spectra recorded at relatively slow spinning speeds (3 kHz) allowed both the quadrupolar splitting and isotropic linewidths to be monitored in a single experiment, as well as providing improved sensitivity and resolution in comparison to the static spectra (Fig. 32). Several other reports have also highlighted the advantages of  $^{14}\text{N}$  MAS NMR in studying lipid membranes [213-215].

In applications to materials science, amphiphilic mesophases can be used as templates for the synthesis of ordered mesoporous materials. Chen *et al.* used *in situ*  $^{14}\text{N}$  NMR to study the  $\text{C}_{16}\text{TAB}$  template phase during the formation of MCM-41 [216]. By comparing the results with  $^{14}\text{N}$  spectra obtained from the spherical micelle, rod-like micelle and hexagonal phases of  $\text{C}_{16}\text{TAB}$ , they were able to rule out the possibility of templating on the hexagonal phase and showed that the silicate precursors instead arrange around rod-shaped  $\text{C}_{16}\text{TAB}$  micelles. Steel *et al.* studied surfactant mesophases (cetyltrimethylammonium chloride) in the formation of M41S [217]. In this case the  $^{14}\text{N}$  spectrum showed the presence of both isotropic and hexagonal mesophases, which resulted in the formation of hexagonal and lamellar M41S phases at low and high silicate concentrations respectively. Fyfe *et al.* used  $^{14}\text{N}$  MAS NMR to study the tetrapropylammonium species in the formation of the zeolite ZSM-5 [218]. The formation of the zeolite from solution could be monitored by  $^{14}\text{N}$  NMR as the single narrow resonance of the mobile ions broadened over time to eventually match the spectrum obtained from the crystalline structure. ZSM-5 was also studied by Abraham *et al.* [219], while Alonso and co-workers have reported similar studies on other mesoporous systems [220-222].

## 8. Summary

A survey of solid-state NMR techniques that can be used to obtain structural and dynamic information directly from the  $^{14}\text{N}$  nucleus has been presented. Each method discussed offers specific advantages and limitations. Single-crystal experiments, if such a sample can be obtained, can provide very accurate measurements of EFG and CS tensor

parameters, dipolar couplings, and the orientations of these interactions in the crystal frame.  $^{14}\text{N}$  spectra from stationary powder samples can provide fast and simple determination of EFG parameters, as well as a direct and quantitative probe of molecular dynamics over a wide range of timescales. Such patterns are relatively straightforward to obtain for  $C_Q$  values  $< ca.$  200 kHz, while more advanced techniques can be used to record wider patterns. However, extensive overlap of patterns from different nitrogen sites means that the resolution is poor, and CS parameters are very difficult to extract from the static spectra due to the small size of this interaction relative to the first-order quadrupolar broadening.  $^{14}\text{N}$  MAS NMR experiments can be used to accurately quantify both the EFG and CS parameters from multiple sites in powder samples, although the sensitivity decreases significantly for large  $C_Q$  values ( $> ca.$  1 MHz), the experiments can be very technically demanding, and the spectral analysis complex. Overtone spectroscopy, in which the first-order quadrupolar broadening is absent, can be used to dramatically reduce spectral widths allowing a wide range of interactions to be probed, but unfortunately suffers from a low inherent sensitivity as well as complications arising from its complex nutation behavior.

This review, along with the recent article by Cavadini [1], has highlighted the fact that  $^{14}\text{N}$  can, in many situations, be a useful and informative nucleus. If the rich array of experimental and technological developments made over the last several decades is a continuing trend, then no doubt the future will see new, ever-more inventive approaches developed that can allow the vast potential of  $^{14}\text{N}$  NMR to be further realized.

## Acknowledgements

I am grateful to Prof. Robert Schurko and Dr. Christopher Ratcliffe for providing me with the opportunity to pursue the  $^{14}\text{N}$  project, and also for their comments on this article. Dr. Victor Terskikh, Dr. Igor Moudrakovski and Dr. Andreas Brinkmann are also acknowledged for various helpful comments and suggestions. Finally, I thank the numerous authors who contributed figures to this review.

## Abbreviations

A- $\beta$	amyloid- $\beta$
ADRF	adiabatic demagnetization in the rotating frame
C <sub>16</sub> TAB	<i>n</i> -hexadecyltrimethylammonium bromide
CP	cross polarization
CS	chemical shift
CSA	chemical shift anisotropy
CW	continuous wave
DANTE	delays alternating with nutation for tailored excitation
DAPT	dipolar assisted polarization transfer
DAS	dynamic angle spinning
DDAB	didodecyldimethylammonium bromide
DEISM	direct enhancement of integer spin magnetization
DFT	density functional theory
DIPOTSHIFT	dipolar overtone shift
DISQUO	dipolar splittings, quadrupolar offset

DMPC	dimyristoyl phosphatidylcholine
DPPC	dipalmitoyl phosphatidylcholine
EFG	electric field gradient
EPC	egg yolk phosphatidylcholine
EXPRESS	exchange program for relaxing spin systems
FID	free induction decay
FOQI	first-order quadrupolar interaction
HMT	hexamethylenetetramine
LC	liquid crystal
MAS	magic angle spinning
NAV	<i>N</i> -acetylvaline
ORR	overtone rotary recoupling
PISEMA	polarization inversion spin exchange at magic angle
QCPMG	quadrupolar Carr Purcell Meiboom Gill
RF	radio frequency
RotIsseRIe	reorientation-induced redistribution of isochromats
S/N	signal to noise ratio
SLF	separated local field
SOQI	second-order quadrupolar interaction
STARS	spectrum analysis for rotating solids
STEAMER	slow turning for echo amplitude modulation and echo reduction
WURST	wideband, uniform rate, smooth truncation
XRD	X-ray diffraction

## References

- [1] S. Cavadini, *Prog. Nucl. Magn. Reson. Spectrosc.* **56** (2010) 46-77
- [2] J.P. Yesinowski, E.A. Hill, *Solid-state NMR spectroscopy of inorganic materials*; Fitzgerald J.; ACS symposium series; American Chemical Society; Washington DC, 1999, Chapter 13, 358-376
- [3] M.J. Duer, *Solid-state NMR Spectroscopy*, Blackwell (2004), Chapter 5, 239-240
- [4] A. Pines, M.G. Gibby, J.S. Waugh, *J. Chem. Phys.* **59** (1973) 569-590
- [5] B.A. Whitehouse, J.D. Ray, D.J. Royer, *J. Magn. Reson.* **1** (1969) 311-326
- [6] M. Linzer, R.A. Forman, *J. Chem. Phys.* **46** (1967) 4690-4693
- [7] A.S. DeReggi, P.C. Canepa, T.A. Scott, *J. Magn. Reson.* **1** (1969) 144-168
- [8] E.K. Wolff, R.G. Griffin, C.J. Watson, *J. Chem. Phys.* **66** (1977) 5433-5438
- [9] R.E. Stark, R.A. Haberkorn, R.G. Griffin, *J. Chem. Phys.* **68** (1978) 1996-1997
- [10] R.A. Haberkorn, R.E. Stark, H. van Willigen, R.G. Griffin, *J. Am. Chem. Soc.* **103** (1981) 2534-2539
- [11] R.K. Hester, J.L. Ackerman, B.L. Neff, J.S. Waugh, *Phys. Rev. Lett.* **36** (1976) 1081-1083
- [12] M.E. Stoll, A.J. Vega, R.W. Vaughan, *J. Chem. Phys.* **65** (1976) 4093-4098
- [13] G. Bodenhausen, R.E. Stark, D.J. Ruben, R.G. Griffin, *Chem. Phys. Lett.* **67** (1979) 424-427
- [14] C.H. Wu, A. Ramamoorthy, S.J. Opella, *J. Magn. Reson. A* **109** (1994) 270-272
- [15] C. Qian, R. Fu, P. Gor'kov, W.W. Brey, T.A. Cross, Z. Gan, *J. Magn. Reson.* **196** (2009) 96-99
- [16] M. Lee, W.I. Goldberg, *Phys. Rev. A* **140** (1965) 1261-1271

- [17] D. Suter, R.R. Ernst, Phys. Rev. B **25** (1982) 6038-6041
- [18] D. Suter, R.R. Ernst, Phys. Rev. B **32** (1985) 5608-5627
- [19] A. Naito, S. Ganapathy, P. Raghunathan, C.A. McDowell, J. Chem. Phys. **79** (1983) 4173-4182
- [20] A. Naito, C.A. McDowell, J. Chem. Phys. **81** (1984) 4795-4803
- [21] C.A. McDowell, A. Naito, D.L. Sastry, K. Takegoshi, J. Magn. Reson. **69** (1986) 283-292
- [22] A. Naito, C.A. McDowell, Rev. Sci. Instrum. **60** (1989) 1037-1039
- [23] K. Differt, R. Messer, J. Phys. C: Solid State Phys. **13** (1980) 717-724
- [24] T.J. Bastow, S.N. Stuart, Chem. Phys. Lett. **180** (1991) 305-309
- [25] O. Liechti, R. Kind, J. Magn. Reson. **85** (1989) 480-491
- [26] B. Zalar, R. Blinc, W. Albert, J. Petersson, Phys. Rev. B **56** (1997) 5709-5712
- [27] R.A. Santos, P. Tang, W.-J. Chien, S. Kwan, G.S. Harbison, J. Phys Chem. **94** (1990) 2717-2721
- [28] R. Subramanian, S.A. Koch, G.S. Harbison, J. Phys. Chem. **97** (1993) 8625-8629
- [29] Y.-S. Kye, G.S. Harbison, Magn. Reson. Chem. **37** (1999) 299-302
- [30] G.S. Harbison, Y.-S. Kye, G.H. Penner, M. Grandin, M. Monette, J. Phys. Chem. B **106** (2002) 10285-10291
- [31] B.W. Mangum, D.B. Utton, Physica **60** (1972) 63-72
- [32] A. Baviera, G. Bonera, F. Borsa, Phys. Lett. A **51** (1975) 463-464
- [33] W.C. Bailey, H.S. Story, J. Chem. Phys. **60** (1974) 1952-1953
- [34] K. Yamada, N. Weiden, A. Weiss, J. Mol. Struct. **111** (1983) 217-226
- [35] T.J. Bastow, S.N. Stuart, J. Phys. Condens. Matter **1** (1989) 4649-4657

- [36] S. Mulla-Osman, D. Michel, Z. Czaplá, Phys. Stat. Sol. B **236** (2003) 173-181
- [37] D. Michel, B. Müller, J. Petersson, A. Trampert, R. Walisch, Phys. Rev. B **43** (1991) 7507-7518
- [38] J.P. Yesinowski, Phys. Stat. Sol. C **2** (2005) 2399-2402
- [39] R.G. Shulman, B.J. Wyluda, J. Phys. Chem. Solids **23** (1962) 166
- [40] M. Kuznietz, J. Chem. Phys. **49** (1968) 3731-3732
- [41] M. Kuznietz, Phys. Rev. **180** (1969) 476-481
- [42] W.D. Knight, Phys. Rev. **76** (1949) 1259-1261
- [43] S.L. Segel, J. Chem. Phys. **68** (1978) 330-331
- [44] S.L. Segel, J. Chem. Phys. **75** (1981) 4746-4747
- [45] D.J. Siminovitch, M. Rance, K.R. Jeffrey, FEBS Lett. **112** (1980) 79-82
- [46] T.M. Rothgeb, E. Oldfield, J. Bio. Chem. **256** (1981) 6004-6009
- [47] K.J.D. MacKenzie, R.H. Meinhold, D.G. McGavin, J.A. Ripmeester, I. Moudrakovski, Solid State Nucl. Magn. Reson. **4** (1995) 193-201
- [48] H. Ono, S. Ishimaru, R. Ikeda, H. Ishida, Chem. Phys. Lett. **275** (1997) 485-490
- [49] P.A. Speight, K.R. Jeffrey, J. Magn. Reson. **10** (1973) 195-202
- [50] D.F. Cooke, K.R. Jeffrey, J. Magn. Reson. **18** (1975) 455-470
- [51] R. Blinc, M. Burgar, V. Rutar, Solid State Commun. **27** (1978) 1021-1023
- [52] R. Blinc, V. Rutar, F. Milia, Phys. Rev. B **23** (1981) 4577-4581
- [53] R. Blinc, T. Apih, J. Dolinšek, M. Šprogar, B. Zalar, Phys. Rev. B **52** (1995) 15217-15222
- [54] A. Gregorovič, B. Zalar, R. Blinc, D.C. Ailion, Phys. Rev. B **60** (1999) 76-79
- [55] L.M. Ishol, T.A. Scott, M. Goldblatt, J. Magn. Reson. **23** (1976) 313-320

- [56] R.E. Wasylishen, B.A. Pettitt, K.R. Jeffrey, *J. Chem. Phys.* **74** (1981) 6022-6026
- [57] R.E. Wasylishen, O. Knop, J.B. Macdonald, *Solid State Commun.* **56** (1985) 581-582
- [58] E.K. Jeong, J.H. Walton, M.A. Doverspike, M.S. Conradi, *J. Magn. Reson.* **89** (1990) 381-385
- [59] R. Blinc, J. Seliger, V. Žagar, T. Apih, J. Dolinšek, H. Warhanek, A. Fuith, W. Schranz, *Phys. Rev. B* **42** (1990) 8125-8132
- [60] Y. Furukawa, *J. Mol. Struct.* **345** (1995) 119-122
- [61] R. Blinc, D.C. Ailion, J. Dolinšek, S. Zumer, *Phys. Rev. Lett.* **54** (1985) 79-81
- [62] R. Blinc, S. Žumer, D.C. Ailion, J. Nicponski, *J. Physique* **46** (1985) 1205-1209
- [63] R. Blinc, V. Rutar, J. Dolinšek, B. Topič, F. Milia, S. Žumer, *Ferroelectrics* **66** (1986) 57-71
- [64] A.M. Fajdiga, J. Dolinšek, R. Blinc, A.P. Levanyuk, R. Perret, H. Arend, R. Kind, *Z. Phys. B Condens. Mat.* **77** (1989) 329-332
- [65] M. Punkkinen, A.H. Vuorimäki, E.E. Ylinen, A. Kaikkonen, *J. Magn. Reson.* **130** (1998) 287-291
- [66] E.E. Ylinen, A. Kaikkonen, M. Punkkinen, *Solid State Nucl. Magn. Reson.* **10** (1997) 25-31
- [67] S. Vega, T.W. Shattuck, A. Pines, *Phys. Rev. Lett.* **37** (1976) 43-46
- [68] T.K. Pratum, M.P. Klein, *J. Magn. Reson.* **53** (1983) 473-485
- [69] T.K. Pratum, M.P. Klein, *J. Magn. Reson.* **55** (1983) 421-437
- [70] T.K. Pratum, M.P. Klein, *J. Magn. Reson.* **81** (1989) 350-370
- [71] E. Meirovitch, J.H. Freed, *Chem. Phys. Lett.* **64** (1979) 311-316

- [72] T.H. Huang, R.P. Skarjune, R.J. Wittebort, R.G. Griffin, E. Oldfield, *J. Am. Chem. Soc.* **102** (1980) 7377-7379
- [73] H.W. Spiess, H. Sillescu, *J. Magn. Reson.* **42** (1981) 381-389
- [74] M. Fechtelkord, A. Englehardt, J.-C. Buhl, L. Schwalowsky, U. Bismayer, *Solid State Nucl. Magn. Reson.* **17** (2000) 76-88
- [75] A. Thangaraj, P.R. Rajamohanan, P.M. Suryavanshi, S. Ganapathy, *J. Chem. Soc. Chem. Commun.* **7** (1991) 493-494
- [76] W.G. Clark, M.E. Hanson, F. Lefloch, P. Ségransan, *Rev. Sci. Instrum.* **66** (1995) 2453-2464
- [77] D. Massiot, I. Farnan, N. Gautier, D. Trumeau, A. Trokiner, J.P. Coutures, *Solid State Nucl. Magn. Reson.* **4** (1995) 241-248
- [78] E.A. Hill, J.P. Yesinowski, *J. Am. Chem. Soc.* **118** (1996) 6798-6799
- [79] F.H. Larsen, H.J. Jakobsen, P.D. Ellis, N.C. Nielsen, *J. Phys. Chem. A* **101** (1997) 8597-8606
- [80] R. Siegel, T.T. Nakashima, R.E. Wasylshen, *Concepts Mag. Reso. A* **26** (2005) 62-77
- [81] E.W. Randall, A.A. Samoilenko, R. Fu, *Solid State Nucl. Magn. Reson.* **14** (1999) 173-179
- [82] E.A. Hill, J.P. Yesinowski, *J. Chem. Phys.* **106** (1997) 8650-8659
- [83] E.A. Hill, J.P. Yesinowski, *J. Chem. Phys.* **107** (1997) 346-354
- [84] G. Bodenhausen, R. Freeman, G.A. Morris, *J. Mag. Reson.* **23** (1976) 171-175
- [85] R. Bhattacharyya, L. Frydman, *J. Chem. Phys.* **127** (2007) 194503
- [86] E. Kupče, R. Freeman, *J. Mag. Reson. A* **115** (1995) 273-276

- [87] L.A. O'Dell, R.W. Schurko, Chem. Phys. Lett. **464** (2008) 97-102
- [88] L.A. O'Dell, R.W. Schurko, J. Am. Chem. Soc. **131** (2009) 6658-6659
- [89] R. Siegel, T.T. Nakashima, R.E. Wasylshen, Concepts Magn. Reson. A **26** (2005) 47-61
- [90] L.A. O'Dell, R.W. Schurko, Phys. Chem. Chem. Phys. **11** (2009) 7069-7077
- [91] L.A. O'Dell, C.I. Ratcliffe, J. Phys. Chem. A **115** (2011) 747-752
- [92] L.A. O'Dell, C.I. Ratcliffe, Chem. Commun. **46** (2010) 6774-6776
- [93] R.L. Vold, G.L. Hoatson, J. Magn. Reson. **198** (2009) 57-72
- [94] L.A. O'Dell, R.W. Schurko, K.J. Harris, J. Autschbach, C.I. Ratcliffe, J. Am. Chem. Soc. **133** (2011) 527-546
- [95] J. Persons, G.S. Harbison, Magn. Reson. Chem. **45** (2007) 905-908
- [96] G. Jeschke, M. Jansen, Angew. Chem. Int. Ed. **37** (1998) 1282-1283
- [97] T.J. Bastow, D. Massiot, J.P. Coutures, Solid State Nucl. Magn. Reson. **10** (1998) 241-245
- [98] K. Ermolaev, B.M. Fung, J. Chem. Phys. **110** (1999) 7977-7982
- [99] A.K. Khitritin, B.M. Fung, J. Chem. Phys. **111** (1999) 8963-8969
- [100] S.P. Marburger, B.M. Fung, A.K. Khitritin, J. Magn. Reson. **154** (2002) 205-209
- [101] T. Bräuniger, P. Kempgens, R.K. Harris, A.P. Howes, K. Liddell, D.P. Thompson, Solid State Nucl. Magn. Reson. **23** (2003) 62-76
- [102] T. Bräuniger, T. Müller, A. Pampel, H.-P. Abicht, Chem. Mater. **17** (2005) 4114-4117
- [103] J.P. Yesinowski, A.P. Purdy, J. Am. Chem. Soc. **126** (2004) 9166-9167

- [104] A.P. Purdy, J.P. Yesinowski, A.T. Hanbicki, *Phys. Stat. Sol. C* **7** (2005) 2437-2440
- [105] H.J. Jakobsen, A.R. Hove, H. Bildsøe, J. Skibsted, M. Brorson, *J. Magn. Reson.* **185** (2007) 159-163
- [106] H.J. Jakobsen, H. Bildsøe, J. Skibsted, T. Giavani, *J. Am. Chem. Soc.* **123** (2001) 5098-5099
- [107] J. Skibsted, N.C. Nielsen, H. Bildsøe, H.J. Jakobsen, *J. Magn. Reson.* **95** (1991) 88-117
- [108] S.E. Ashbrook, J. McManus, M.J. Thrippleton, S. Wimperis, *Prog. Nucl. Magn. Reson. Spectrosc.* **55** (2009) 160-181
- [109] T. Giavani, H. Bildsøe, J. Skibsted, H.J. Jakobsen, *J. Phys. Chem. B* **106** (2002) 3026-3032
- [110] T. Giavani, K. Johannsen, C.J.H. Jacobsen, N. Blom, H. Bildsøe, J. Skibsted, H.J. Jakobsen, *Solid State Nucl. Magn. Reson.* **24** (2003) 218-235
- [111] T. Giavani, H. Bildsøe, J. Skibsted J., H.J. Jakobsen, *Chem. Phys. Lett.* **377** (2003) 426-432
- [112] T. Giavani, H. Bildsøe, J. Skibsted, H.J. Jakobsen, *J. Magn. Reson.* **166** (2004) 262-272
- [113] B. Zhou, T. Giavani, H. Bildsøe, J. Skibsted, H.J. Jakobsen, *Chem. Phys. Lett.* **402** (2005) 133-137
- [114] H.J. Jakobsen, A.R. Hove, R.G. Hazell, H. Bildsøe, H.J. Skibsted, *Magn. Reson. Chem.* **44** (2006) 348-356

- [115] A.R. Hove, H. Bildsøe, J. Skibsted, M. Brorson, H.J. Jakobsen, *Inorg. Chem.* **45** (2006) 10873-10881
- [116] H.J. Jakobsen, H. Bildsøe, J. Skibsted, M.R. Hansen, M. Brorson, B.R. Srinivasan, W. Bensch, *Inorg. Chem.* **48** (2009) 1787-1789
- [117] F.H. Larsen, *Solid State Nucl. Magn. Reson.* **31** (2007) 100-114
- [118] R.B. Creel, E.D. Von Meerwall, R.G. Barnes, *Chem. Phys. Lett.* **49** (1977) 501-503
- [119] M. Bloom, M.A. LeGros, *Can. J. Phys.* **64** (1986) 1522-1528
- [120] R. Tycko, S.J. Opella, *J. Am. Chem. Soc.* **108** (1986) 3531-3532
- [121] J. Jeener, P. Broekaert, *Phys. Rev.* **157** (1967) 232-240
- [122] R. Tycko, S.J. Opella, *J. Chem. Phys.* **86** (1987) 1761-1774
- [123] R. Tycko, P.L. Stewart, S.J. Opella, *J. Am. Chem. Soc.* **108** (1986) 5419-5425
- [124] K. Takegoshi, K. Hikichi, *Chem. Phys. Lett.* **206** (1993) 450-454
- [125] P.L. Stewart, R. Tycko, S.J. Opella, *J. Chem. Soc., Faraday Trans.* **84** (1988) 3803-3819
- [126] P.L. Stewart, K.G. Valentine, S.J. Opella, *J. Magn. Reson.* **71** (1987) 45-61
- [127] R. McNamara, C.H. Wu, S.J. Opella, *J. Magn. Reson.* **100** (1992) 559-566
- [128] K.V. Ramanathan, S.J. Opella, *J. Magn. Reson.* **78** (1988) 367-370
- [129] R. McNamara, C.H. Wu, S.J. Opella, *J. Magn. Reson. A* **103** (1993) 238-241
- [130] R. McNamara, C.H. Wu, L.E. Chirlian, S.J. Opella, *J. Am. Chem. Soc.* **117** (1995) 7805-7811
- [131] D.-K. Lee, A. Ramamoorthy, *Chem. Phys. Lett.* **280** (1997) 501-506
- [132] M.H. Levitt, *Prog. Nucl. Magn. Reson. Spectrosc.* **18** (1986) 61-122

- [133] D.-K. Lee, A. Ramamoorthy, Chem. Phys. Lett. **286** (1998) 398-402
- [134] D.-K. Lee, A. Ramamoorthy, Chem. Phys. Lett. **286** (1998) 403-407
- [135] L. Marinelli, S. Wi, L. Frydman, J. Chem. Phys. **110** (1999) 3100-3112
- [136] K. Takegoshi, K. Hikichi, Chem. Phys. Lett. **194** (1992) 359-362
- [137] A. Llor, J. Virlet, Chem. Phys. Lett. **152** (1988) 248-253
- [138] S. Wi, L. Frydman, J. Am. Chem. Soc. **123** (2001) 10354-10361
- [139] A.N. Garroway, J.B. Miller, J. Magn. Reson. **82** (1989) 591-596
- [140] K. Takegoshi, T. Yano, K. Takeda, T. Terao, J. Am. Chem. Soc. **123** (2001) 10786-10787
- [141] J. Fukazawa, S. Kato, T. Ozaki, A. Shoji, K. Takegoshi, J. Am. Chem. Soc. **132** (2010) 4290-4294
- [142] P.J. Grandinetti, Solid State Nucl. Magn. Reson. **23** (2003) 1-13
- [143] N.M. Trease, P.J. Grandinetti, J. Chem. Phys. **128** (2008) 052318
- [144] D. Kuwahara, Chem. Phys. Lett. **377** (2003) 20-26
- [145] D. Kuwahara, H. Okamoto, Y. Yamazaki, Chem. Phys. Lett. **414** (2005) 514-519
- [146] S. Jayanthi, K.V. Ramanathan, Chem. Phys. Lett. **502** (2011) 121-125
- [147] C.W. Hilbers, C. MacLean, Mol. Phys. **16** (1969) 275-284
- [148] C.W. Hilbers, C. MacLean, Mol. Phys. **17** (1969) 517-522
- [149] J. Biemond, C. MacLean, Mol. Phys. **26** (1973) 409-418
- [150] C.S. Yannoni, J. Chem. Phys. **52** (1970) 2005-2010
- [151] M.J. Gerace, B.M. Fung, J. Chem. Phys. **53** (1970) 2984-2986
- [152] A. Loewenstein, M. Brenman, J. Magn. Reson. **34** (1979) 193-198
- [153] A. Loewenstein, M. Brenman, J. Magn. Reson. **36** (1979) 419-424

- [154] A. Loewenstein, A.D. Goldsmith, *J. Magn. Reson.* **41** (1980) 222-228
- [155] P. Polatin, T. Barbara, B.P. Dailey, *J. Magn. Reson.* **47** (1982) 148-150
- [156] T.M. Barbara, *Mol. Phys.* **54** (1985) 651-656
- [157] D.M. Chen, J.D. Glickson, *J. Magn. Reson.* **28** (1977) 9-15
- [158] N.-O. Persson, B. Lindman, *Mol. Cryst. Liq. Cryst.* **38** (1977) 327-344
- [159] J. Charvolin, A. Loewenstein, J. Virlet, *J. Magn. Reson.* **26** (1977) 529-531
- [160] Haryadi, M. Rankothge, J. Hook, L. van Gorkom, G. Moran, *Magn. Reson. Chem.* **32** (1994) 446-451
- [161] M. Rankothge, J. Hook, L. van Gorkom, G. Moran, *Macromolecules* **30** (1997) 4357-4362
- [162] G. Pellizer, F. Asaro, *Magn. Reson. Chem.* **46** (2008) 80-85
- [163] B. Cabane, W.G. Clark, *Phys. Rev. Lett.* **25** (1970) 91-93
- [164] B. Cabane, W.G. Clark, *Solid State Commun.* **13** (1973) 129-132
- [165] R.Y. Dong, E. Tomchuk, J.J. Visintainer, E. Bock, *Mol. Cryst. Liq. Cryst.* **33** (1976) 101-111
- [166] U. Henriksson, L. Ödberg, J.C. Eriksson, L. Westman, *J. Phys. Chem.* **81** (1977) 76-82
- [167] A. Khan, K. Fontell, G. Lindblom, *J. Phys. Chem.* **86** (1982) 383-386
- [168] P.-O. Eriksson, A. Khan, G. Lindblom, *J. Phys. Chem.* **86** (1982) 387-393
- [169] P.-O. Eriksson, G. Lindblom, G. Arvidson, *J. Phys. Chem.* **89** (1985) 1050-1053
- [170] G. Arvidson, I. Brentel, A. Khan, G. Lindblom, K. Fontell, *Eur. J. Biochem.* **152** (1985) 753-759
- [171] P.-O. Eriksson, G. Lindblom, G. Arvidson, *J. Phys. Chem.* **91** (1987) 846-853

- [172] K. Koga, Y. Kanazawa, *Biochem.* **19** (1980) 2779-2783
- [173] Y. Kanazawa, K. Koga, *Biochem. Biophys. Res. Commun.* **95** (1980) 269-272
- [174] K. Koga, Y. Kanazawa, *Chem. Phys. Lipids* **36** (1984) 153-167
- [175] K. Koga, Y. Tanaka, Y. Kanazawa, *Chem. Phys. Lipids* **36** (1985) 285-295
- [176] D.J. Siminovitch, K.R. Jeffrey, *Biochim. Biophys. Acta* **645** (1981) 270-278
- [177] D.J. Siminovitch, K.R. Jeffrey, H. Eibl, *Biochim. Biophys. Acta* **727** (1983) 122-134
- [178] D.J. Siminovitch, M.F. Brown, K.R. Jeffrey, *Biochem.* **23** (1984) 2412-2420
- [179] D.J. Siminovitch, M. Rance, K.R. Jeffrey, M.F. Brown, *J. Magn. Reson.* **58** (1984) 62-75
- [180] O. Söderman, H. Walderhaug, U. Henriksson, P. Stilbs, *J. Phys. Chem.* **89** (1985) 3693-3701
- [181] L.B.-Å. Johansson, O. Söderman, *J. Phys. Chem.* **91** (1987) 5275-5278
- [182] O. Söderman, G. Carlström, M. Moduzzi, U. Olsson, *Langmuir* **4** (1988) 1029-1044
- [183] T.C. Wong, K. Ikeda, K. Meguro, O. Söderman, U. Olsson, B. Lindman, *J. Phys. Chem.* **93** (1989) 4861-4867
- [184] O. Söderman, U. Olsson, T.C. Wong, *J. Phys. Chem.* **93** (1989) 7474-7478
- [185] K. Ikeda, A. Khan, K. Meguro, B. Lindman, *J. Colloid Interf. Sci.* **133** (1989) 192-199
- [186] R. Skurtveit, U. Olsson, *J. Phys. Chem.* **96** (1992) 8640-8646
- [187] M. Moduzzi, U. Olsson, O. Söderman, *Langmuir* **9** (1993) 2914-2920
- [188] M. Moduzzi, F. Caboi, F. Larché, U. Olsson, *Langmuir* **13** (1997) 2184-2190

- [189] M. Olla, M. Moduzzi, *Langmuir* **16** (2000) 6141-6147
- [190] M. Moduzzi, S. Mele, *J. Phys. Chem. B* **105** (2001) 12579-12582
- [191] J.R.C. van der Maarel, D.E. Woessner, M.E. Merritt, *J. Phys. Chem. B* **106** (2002) 3864-3871
- [192] R. Deslauriers, I. Ekiel, R.A. Byrd, H.C. Jarrell, I.C.P. Smith, *Biochim. Biophys. Acta* **720** (1982) 329-337
- [193] L.K. Tamm, J. Seelig, *Biochem.* **22** (1983) 1474-1483
- [194] M.-D. Tsai, R.-T. Jiang, K. Bruzik, *J. Am. Chem. Soc.* **105** (1983) 2478-2480
- [195] R. Ghosh, *Biochem.* **27** (1988) 7750-7758
- [196] P.G. Scherer, J. Seelig, *Biochem.* **28** (1989) 7720-7728
- [197] E.S. Blackmore, G.J.T. Tiddy, *Liq. Cryst.* **8** (1990) 131-151
- [198] R. Smith, F. Separovic, F.C. Bennett, B.A. Cornell, *Biophys. J.* **63** (1992) 469-474
- [199] U. Henriksson, E.S. Blackmore, G.J.T. Tiddy, O. Söderman, *J. Phys. Chem.* **96** (1992) 3894-3902
- [200] M. Moduzzi, A. Chittofrati, V. Boselli, *J. Phys. Chem.* **98** (1994) 7591-7598
- [201] J.P. Dombroski, P.J.B. Edwards, K.W. Jolley, N. Boden, *Liq. Cryst.* **18** (1995) 51-60
- [202] M. Tansho, Y. Onoda, R. Kato, S. Kutsumizu, S. Yano, *Liq. Cryst.* **24** (1998) 525-529
- [203] F. Asaro, L. Liguori L., G. Pellizer, *Croatica Chemica Acta* **74** (2001) 877-885
- [204] R.Y. Dong, *Mol. Phys.* **99** (2001) 637-641

- [205] J.S. Santos, D.-K. Lee, A. Ramamoorthy, *Magn. Reson. Chem.* **42** (2004) 105-114
- [206] J.S. Clawson, G.P. Holland, T.M. Alam, *Phys. Chem. Chem. Phys.* **8** (2006) 2635-2641
- [207] S.V. Dvinskikh, K. Yamamoto, U.H.N. Dürr, A. Ramamoorthy, *J. Magn. Reson.* **184** (2007) 228-235
- [208] C. Loudet, S. Manet, S. Gineste, R. Oda, M.-F. Achard, E.J. Dufourc, *Biophys. J.* **92** (2007) 3949-3959
- [209] M.-A. Sani, S. Castano, E.J. Dufourc, G. Gröbner, *FEBS J.*, **275** (2008) 561-572
- [210] C. Li, M. Yi, J. Hu, H.-X. Zhou, T.A. Cross, *Biophys. J.* **94** (2008) 1295-1302
- [211] A. Ramamoorthy, D.-K. Lee, J.S. Santos, K.A. Henzler-Wildman, *J. Am. Chem. Soc.* **130** (2008) 11023-11029
- [212] F. Lindström, M. Bokvist, T. Sparrman, G. Gröbner, *Phys. Chem. Chem. Phys.* **4** (2002) 5524-5530
- [213] T. Sparrman, P.-O. Westlund, *Phys. Chem. Chem. Phys.* **5** (2003) 2114-2121
- [214] F. Lindström, P.T.F. Williamson, G. Gröbner, *J. Am. Chem. Soc.* **127** (2005) 6610-6616
- [215] C. Heuber, F. Formaggio, C. Baldini, C. Toniolo, K. Müller, *Chem. Biodivers.* **4** (2007) 1200-1218
- [216] C.-Y. Chen, S.L. Burkett, H.-X. Li, M.E. Davis, *Microporous Mater.* **2** (1993) 27-34
- [217] A. Steel, S.W. Carr, M.W. Anderson, *J. Chem. Soc. Chem. Commun.* **13** (1994) 1571-1572

- [218] C.A. Fyfe, R.J. Darton, C. Schneider, F. Scheffler, *J. Phys. Chem. C* **112** (2008) 80-88
- [219] A. Abraham, R. Prins, J.A. van Bokhoven, E.R.H. van Eck, A.P.M. Kentgens, *Solid State Nucl. Magn. Reson.* **35** (2009) 61-66
- [220] I.V. Melnyk, Y.L. Zub, E. Véron, D. Massiot, T. Cacciaguerra, B. Alonso, *J. Mater. Chem.* **18** (2008) 1368-1382
- [221] B. Alonso, D. Massiot, P. Florian, H.H. Paradies, P. Gaveau, T. Mineva, *J. Phys. Chem. B* **113** (2009) 11906-11920
- [222] B. Alonso, T. Mineva, P. Innocenzi, G. Trimmel, K. Stubenrauch, I. Melnyk, Y. Zub, F. Fayon, P. Florian, D. Massiot, *C.R. Chimie* **13** (2010) 431-442

**Table 1. Properties of the two NMR-active isotopes of nitrogen.**

		<b>Natural</b>	<b>Frequency</b>	<b>Gyromagnetic</b>	<b>Quadrupole</b>	
	<b>Spin</b>	<b>abundance</b>	<b><math>\nu_0</math> / MHz</b>	<b>ratio <math>\gamma</math></b>	<b>moment <math>Q</math></b>	<b>Receptivity</b>
	<b>number <math>I</math></b>	<b>/ %</b>	<b>(<math>^1\text{H} = 100</math> MHz)</b>	<b>/ <math>10^7</math> rad T<math>^{-1}</math> S<math>^{-1}</math></b>	<b>/ mbarn</b>	<b>(<math>^1\text{H} = 1.0</math>)</b>
$^{14}\text{N}$	1	99.632	7.226	1.934	20.44	$1.0 \times 10^{-3}$
$^{15}\text{N}$	1/2	0.368	10.137	-2.713	0	$3.8 \times 10^{-6}$

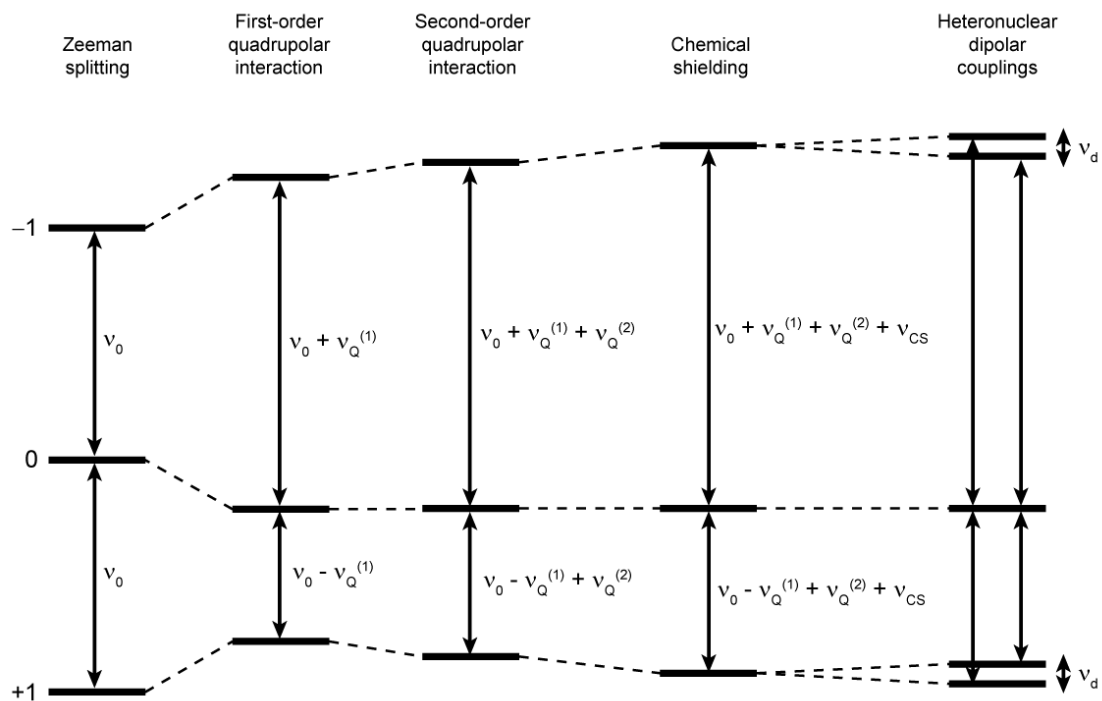


**Fig. 1.** Schematic representation of the perturbations to the  $^{14}\text{N}$  single-quantum transition frequencies caused by various interactions (see text for definitions).

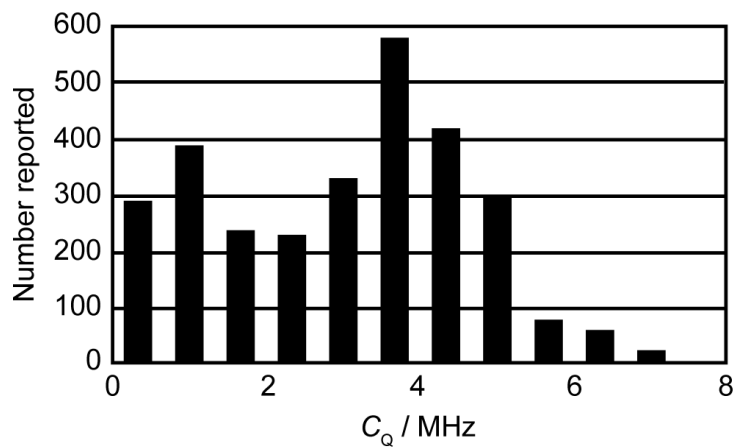


**Fig. 2.** Distribution of  $^{14}\text{N}$   $C_Q$  values measured by various techniques. Adapted from reference [2]. Published 1999 American Chemical Society (reproduced with permission).

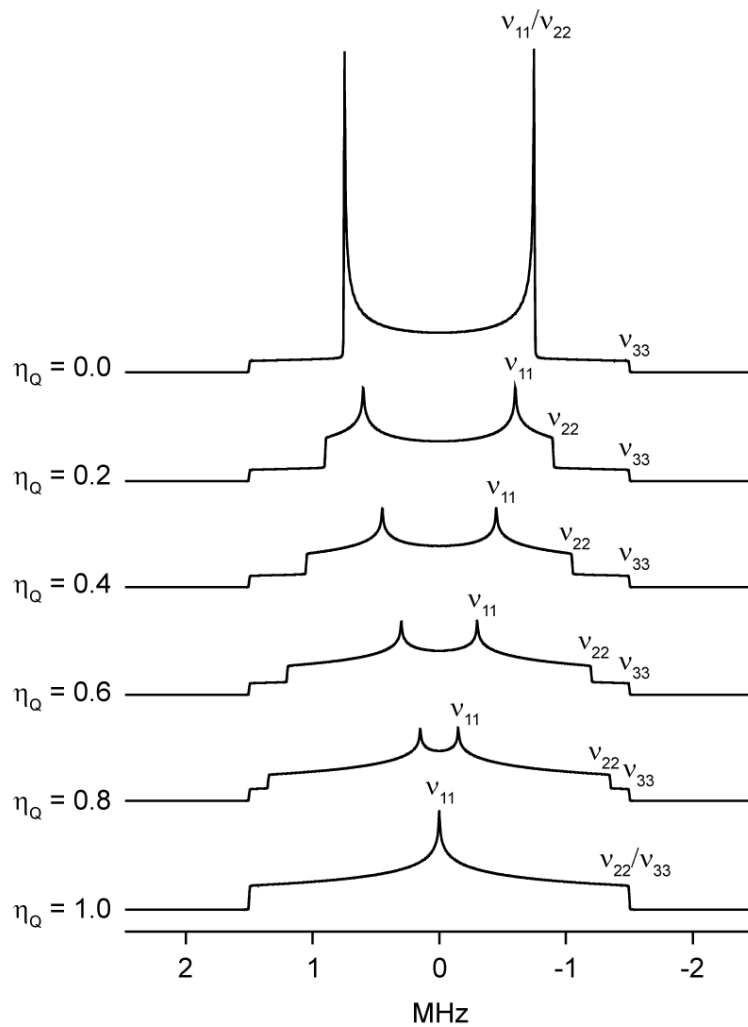


**Fig. 3.** Simulated first-order quadrupolar  $^{14}\text{N}$  lineshapes for a nitrogen site with  $C_Q = 2$  MHz and various asymmetry parameters as shown. The positions of the discontinuities are labeled in each case.

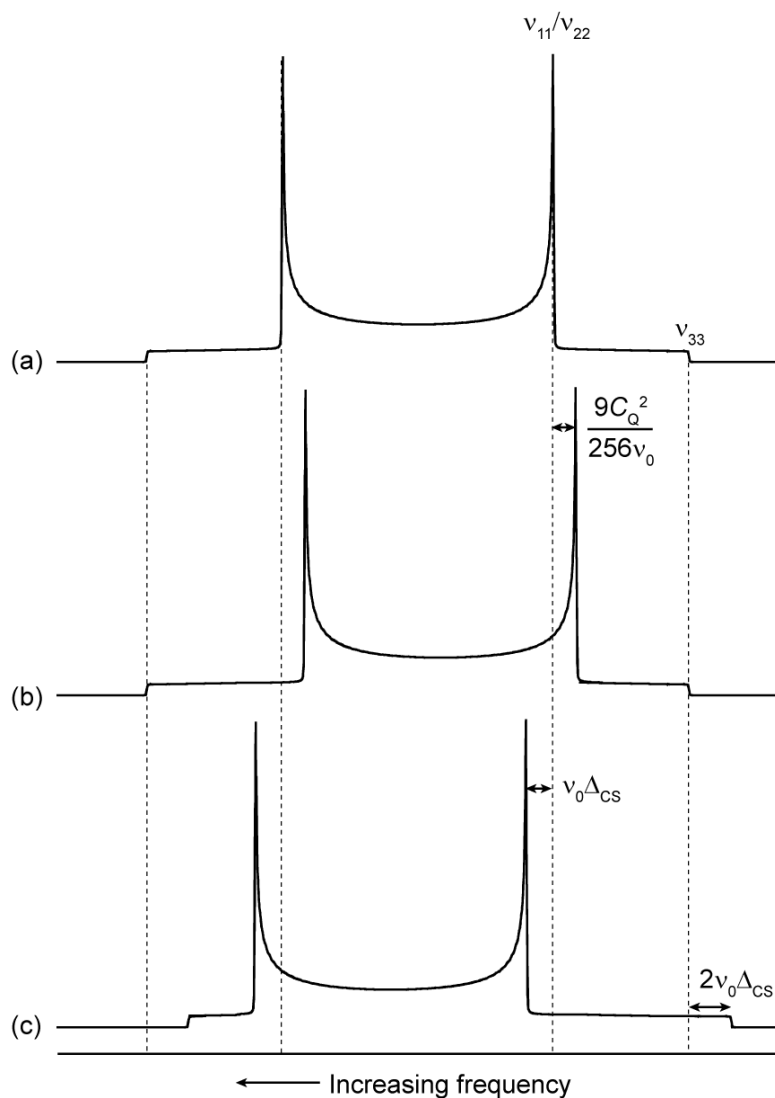


**Fig. 4.** (a) A first-order quadrupolar-broadened  $^{14}\text{N}$  powder pattern with  $\eta_Q = 0$ . The effects of the SOQI and CS on the positions of the discontinuities are shown in (b) and (c) respectively. The sizes of the perturbations are greatly exaggerated relative to the full pattern width. In (c), the CS tensor is assumed to be positive, axially symmetric and coincident with the EFG tensor, and the SOQI is absent.

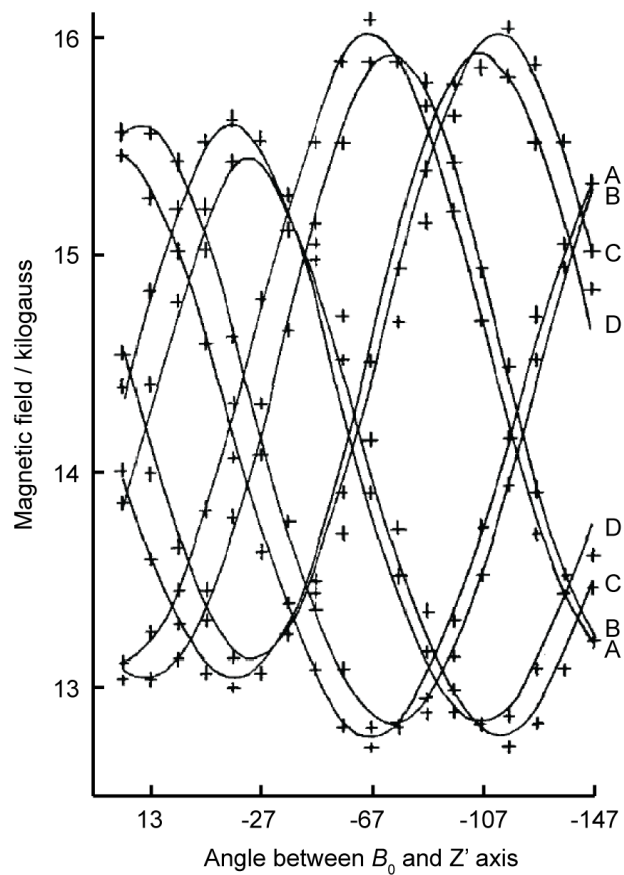


**Fig. 5.**  $^{14}\text{N}$  resonances plotted as a function of rotation angle for a single-crystal sample of uranyl nitrate hexahydrate. The four pairs of resonance lines (A, B, C and D) correspond to four magnetically distinct nitrogen sites in the crystal with  $C_Q$  values of *ca.* 600 kHz. Solid lines show curves fitted to each resonance from derived expressions [5]. The vertical scale represents a resonance frequency range of *ca.* 1.1 MHz. Reproduced with permission from reference [5]. Copyright 1969 Elsevier.

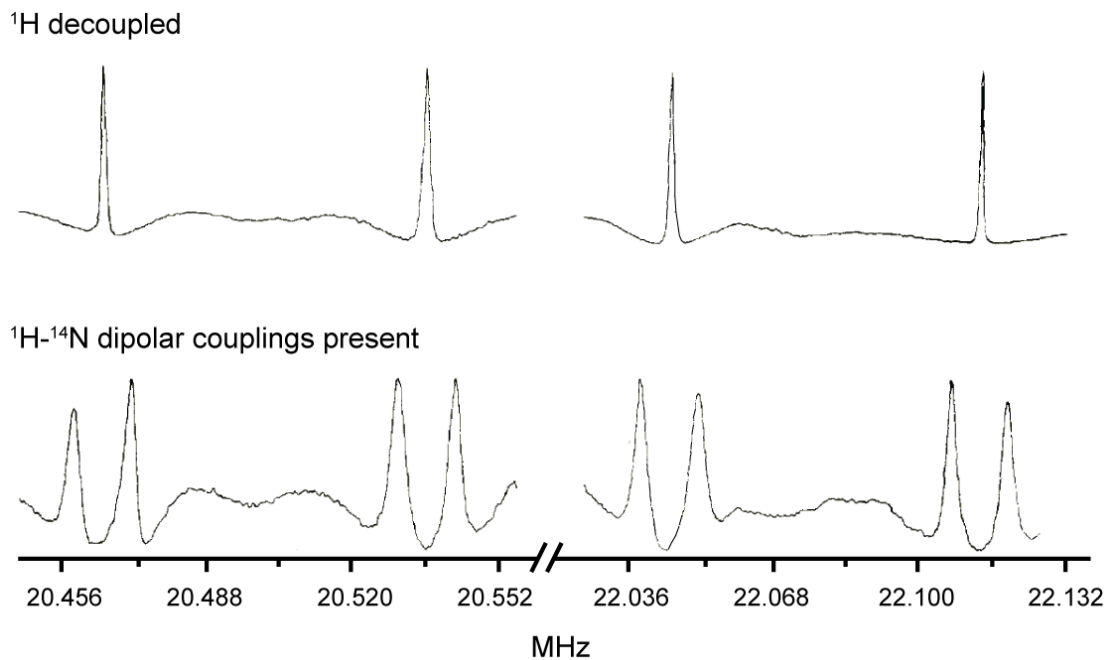


**Fig. 6.**  $^{14}\text{N}$  CP spectra obtained at 6.9 T from a single-crystal of *N*-acetylvaline (NAV) at the same orientation, with (top) and without (bottom)  $^1\text{H}$  decoupling applied. The  $^{14}\text{N}$  sites in NAV have  $C_Q = 3.21$  MHz and  $\eta_Q = 0.32$ . In the top spectra, the linewidths are approximately 1.5 kHz. In the bottom spectra, dipolar splittings of 12.5 kHz are resolved. Reproduced with permission from reference [9]. Copyright 1978 American Institute of Physics.

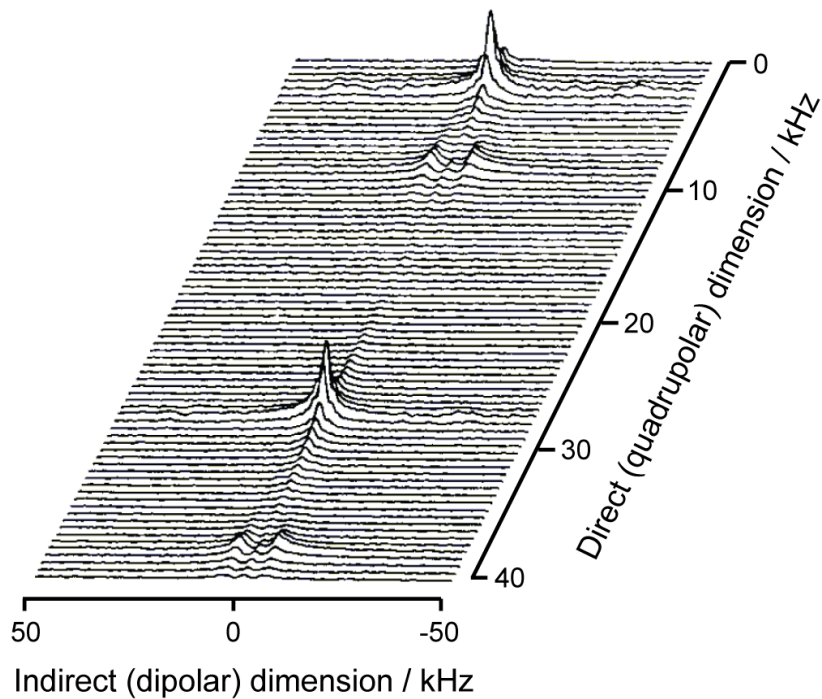


**Fig. 7.**  $^{14}\text{N}$  DISQUO spectrum obtained from a single crystal of L-histidine hydrochloride monohydrate at 6.9 T.  $^1\text{H}$ - $^{14}\text{N}$  dipolar splittings are resolved in the indirect dimension for two of the resonances. Reproduced with permission from reference [13]. Copyright

1979 Elsevier.

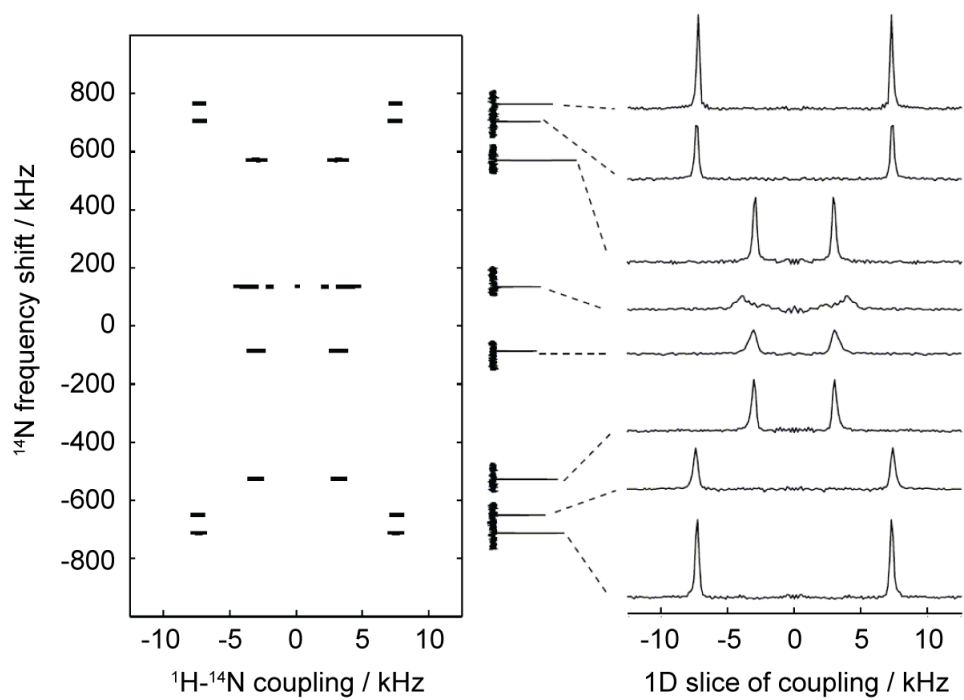


**Fig. 8.**  $^{14}\text{N}$ -PISEMA spectrum obtained from a single crystal of *N*-acetylvaline (NAV) at 14.1 T. Reproduced with permission from reference [15]. Copyright 2009 Elsevier.

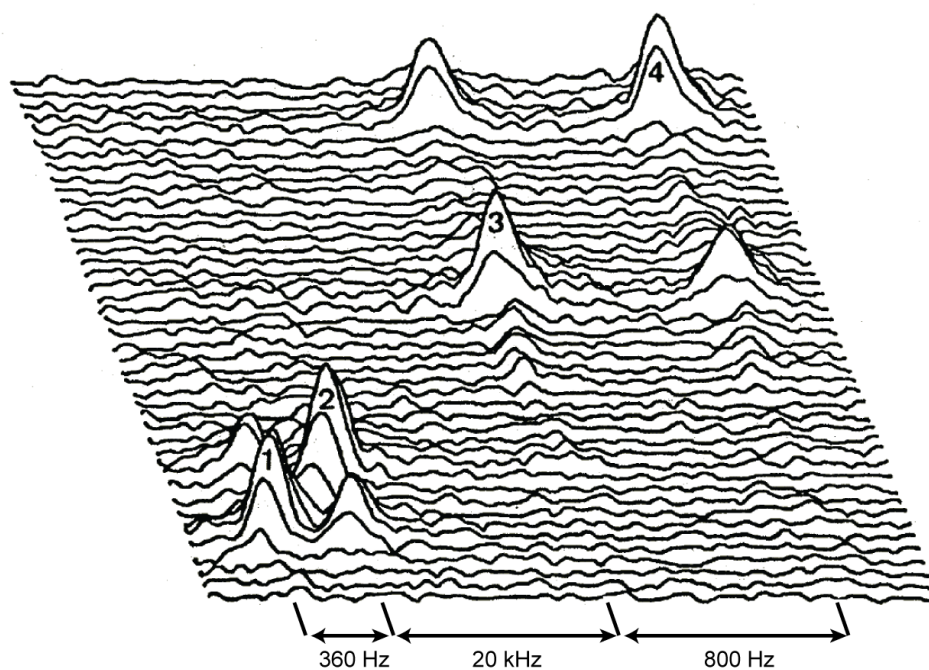


**Fig. 9.**  $^{14}\text{N}$  spin-diffusion spectrum obtained from a single-crystal of ammonium sulfate at 5.2 T. The spectrum has been compressed by frequency folding. Cross-peaks are visible between sites 1 and 2, and sites 3 and 4, indicating exchange of magnetization between these sites. Reproduced with permission from reference [17]. Copyright 1982

American Physical Society.

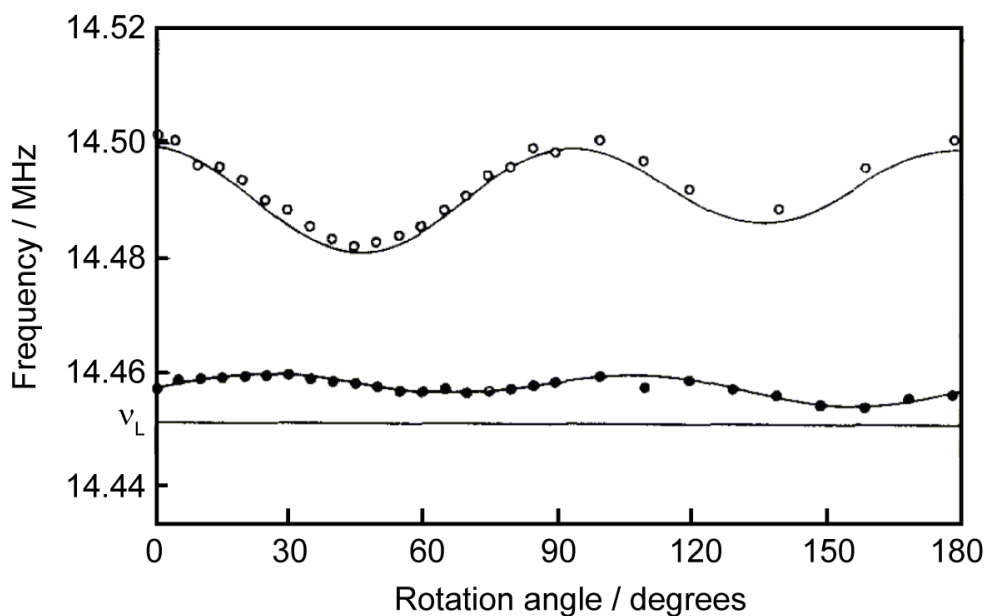


**Fig. 10.** Angular dependence of the average resonance frequency of the pairs of  $^{14}\text{N}$  resonance lines from a single crystal of L-asparagine monohydrate, rotated in the  $bc$  plane. Circles show experimental values ( $\text{N}_\delta$  site open circles and  $\text{N}_\alpha$  site closed circles), while solid lines correspond to simulations.  $\nu_L$  is the frequency obtained from ammonium chloride (4.7 T). Reproduced with permission from reference [20]. Copyright 1984

American Institute of Physics.

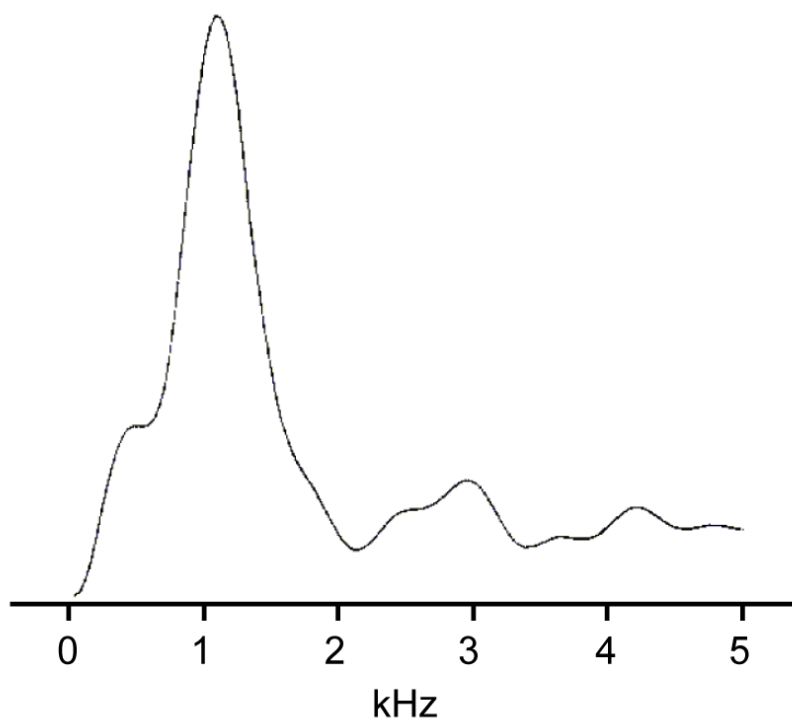


**Fig. 11.**  $^{14}\text{N}$  double-quantum NMR spectrum obtained from a powder sample of ammonium perchlorate ( $C_Q = 27$  kHz) at 3.6 T. The spectrum represents the Fourier transformation of a single-quantum spin-echo amplitude as a function of double-quantum evolution time. Reproduced with permission from reference [66]. Copyright 1997

Elsevier.

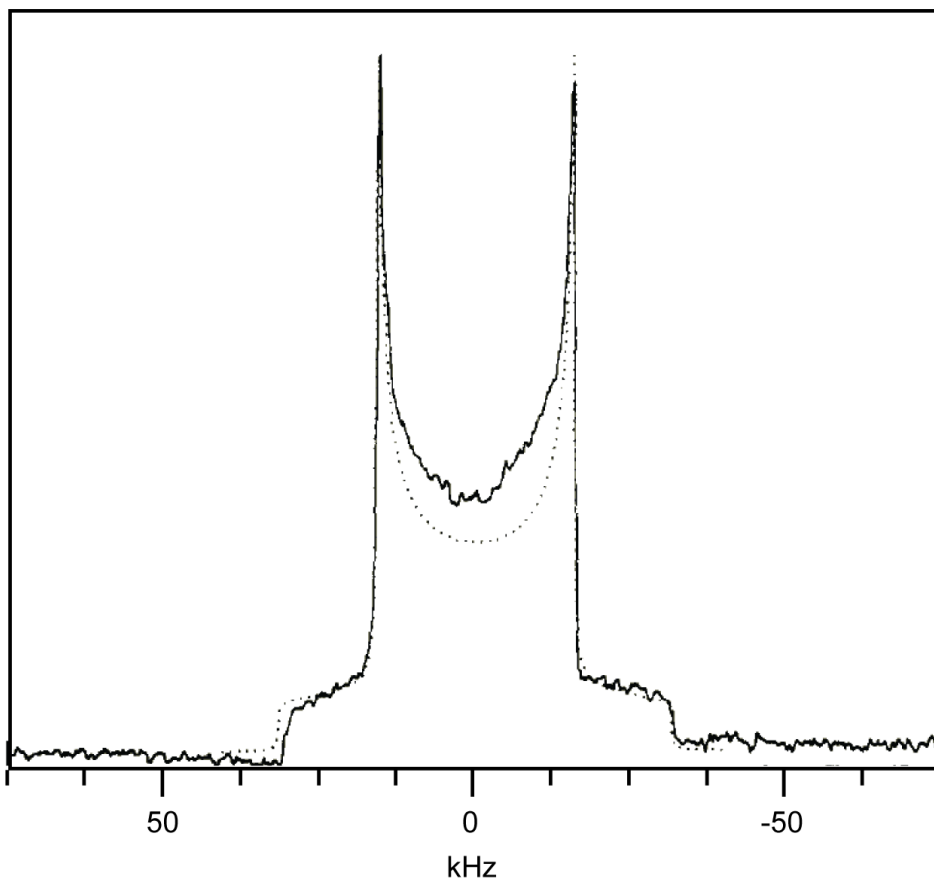


**Fig. 12.**  $^{14}\text{N}$  spectrum of tetraethylammonium iodide, obtained at 6.3 T using ADRF cross-polarization from  $^1\text{H}$  at  $-90^\circ\text{C}$  (10 ms mixing time and 26 kHz spin-lock field on  $^{14}\text{N}$ ). For further details see reference [69]. The dotted line shows a simulation made with  $C_Q = 42.3$  kHz and  $\eta_Q = 0$ . Reproduced with permission from reference [69].

Copyright 1983 Elsevier.

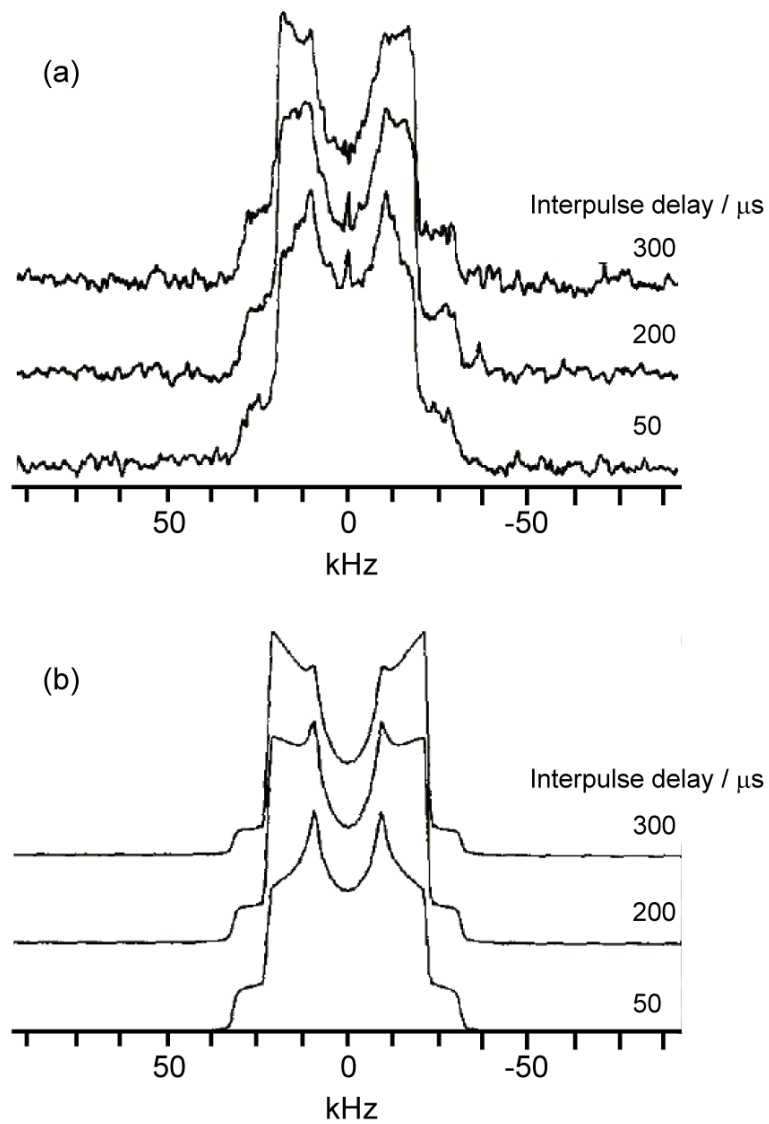


**Fig. 13.** (a)  $^{14}\text{N}$  quadrupole echo spectra obtained at 6.3 T from choline chloride at 48°C and with interpulse delays as shown. (b) Simulated lineshapes with  $C_Q = 57.3$  kHz,  $\eta_Q = 0.2$  and a two-site Markovian jump process with jump rate of  $3 \times 10^6$  Hz between two orientations. Reproduced with permission from reference [70]. Copyright 1989 Elsevier.

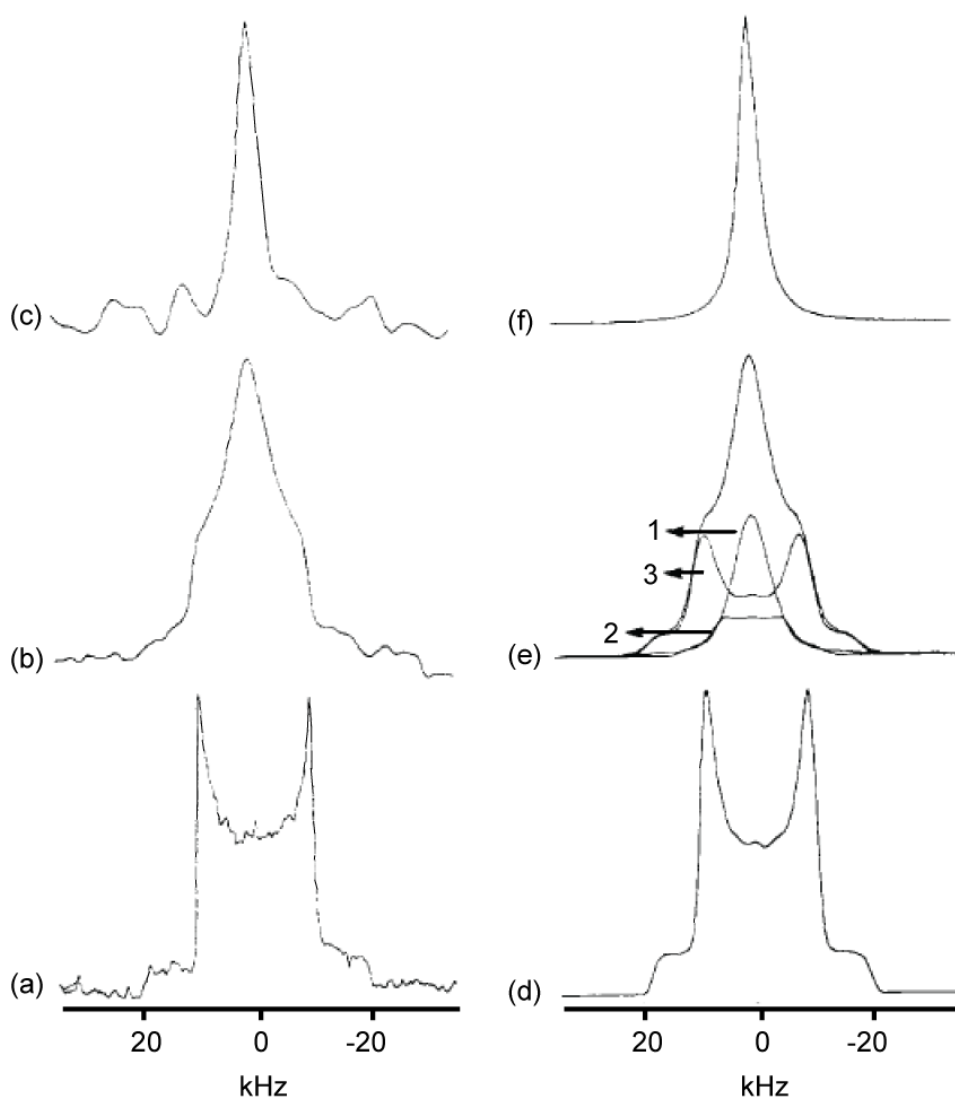


**Fig. 14.**  $^{14}\text{N}$  NMR spectra obtained at 7.05 T from (a) tetramethylammonium bromide, (b) tetramethylammonium in the zeolite ZK-4 and (c) tetraethylammonium in the zeolite ZSM-20. Simulations are shown in (d), (e) and (f). See text for the identity of components 1, 2 and 3. Reproduced from reference [75] by permission of The Royal Society of Chemistry.

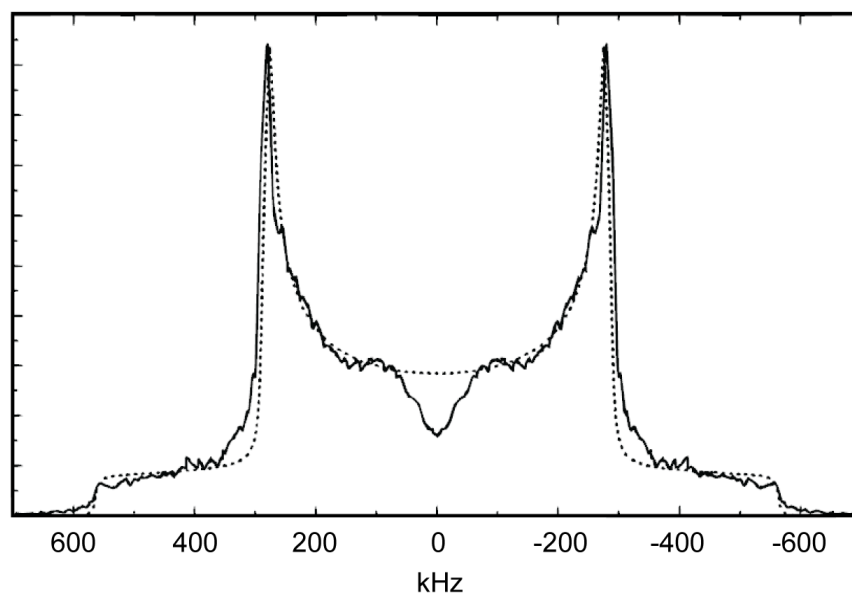


**Fig. 15.** The  $^{14}\text{N}$  powder pattern from potassium nitrate, obtained using a piecewise, frequency-stepped acquisition with QCPMG enhancement at 7.05 T. The dip in intensity in the centre is due to the inability to selectively excite single transitions in that region.

Adapted with permission from reference [78]. Copyright 1996 American Chemical Society.

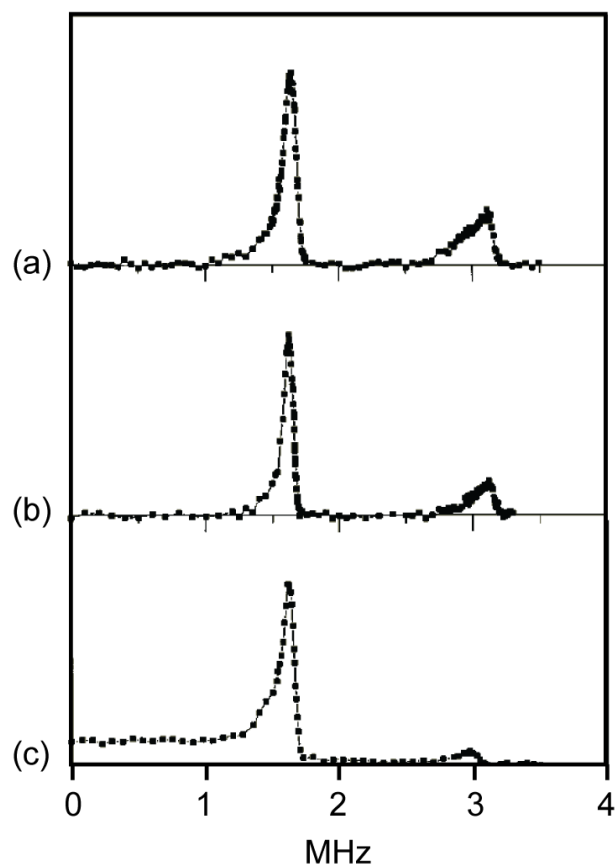


**Fig. 16.**  $^{14}\text{N}$  spectra obtained at 7.05 T from crystals of  $\text{Na}_{1-x}\text{K}_x\text{CN}$  ( $B_0 = 7$  T) at 20 K with (a)  $x = 0.19$  and  $[001]$  parallel to  $B_0$ , (b)  $x = 0.43$  and  $[001]$  parallel to  $B_0$ , and (c)  $x = 0.19$  and  $[011]$  parallel to  $B_0$ . Each point represents a single experiment. Reproduced with permission from reference [26]. Copyright 1997 American Physical Society.

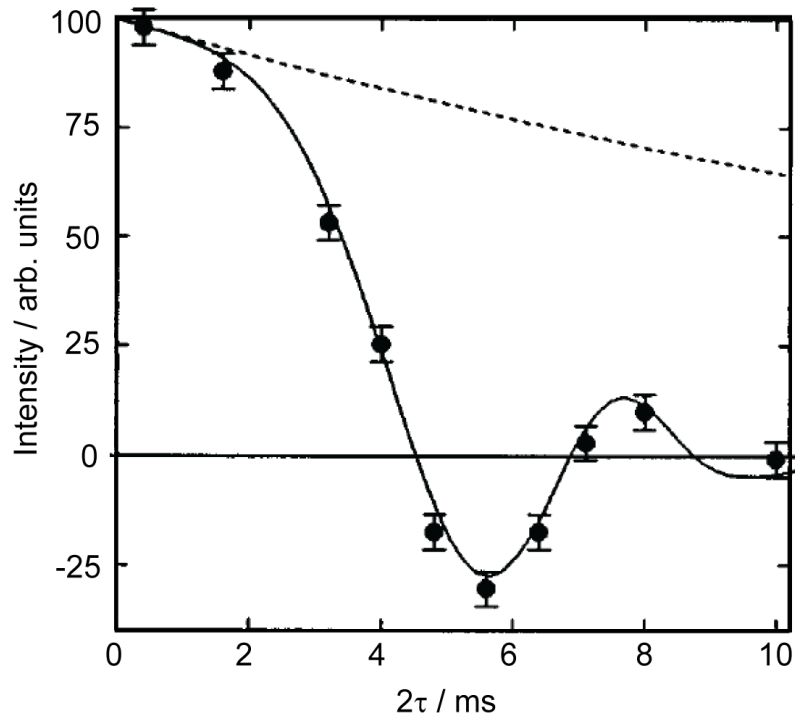


**Fig. 17.** Numerically simulated STEAMER dephasing curve for potassium nitrate at 7.05 T (solid line) and experimentally determined points (circles).  $\tau$  is the inter-pulse delay in the spin-echo experiment. Transverse relaxation in the absence of STEAMER effects is shown as a dashed line. Reproduced with permission from reference [82]. Copyright 1997 American Institute of Physics.

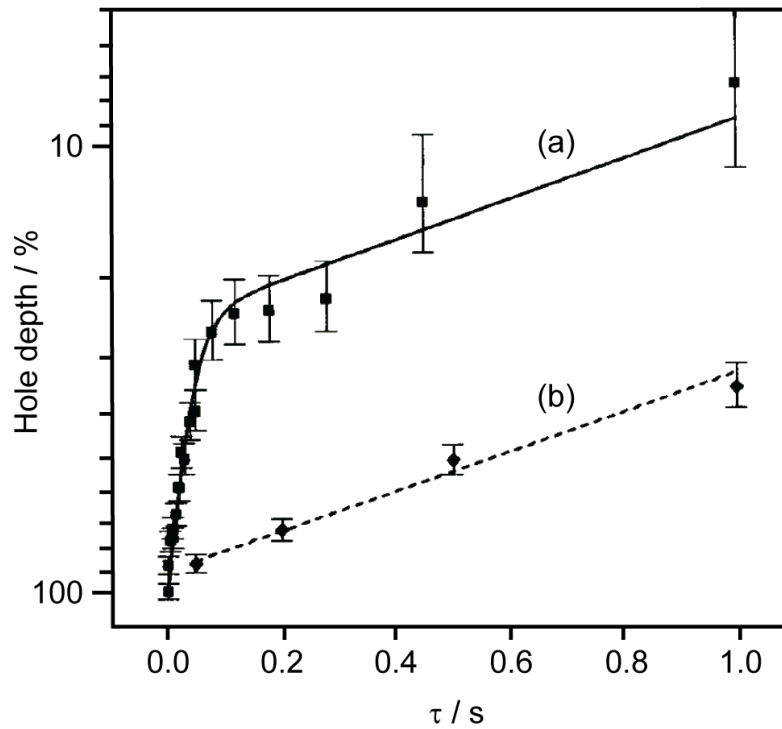


**Fig. 18.** Recovery of a narrow region of saturated  $^{14}\text{N}$  magnetization in hexamethylenetetramine at 7.05 T as a function of time after (a) a single DANTE saturation train and (b) 16 saturation trains. Solid and dotted lines show fits derived from numerical expressions. Reproduced with permission from reference [83]. Copyright 1997 American Institute of Physics.

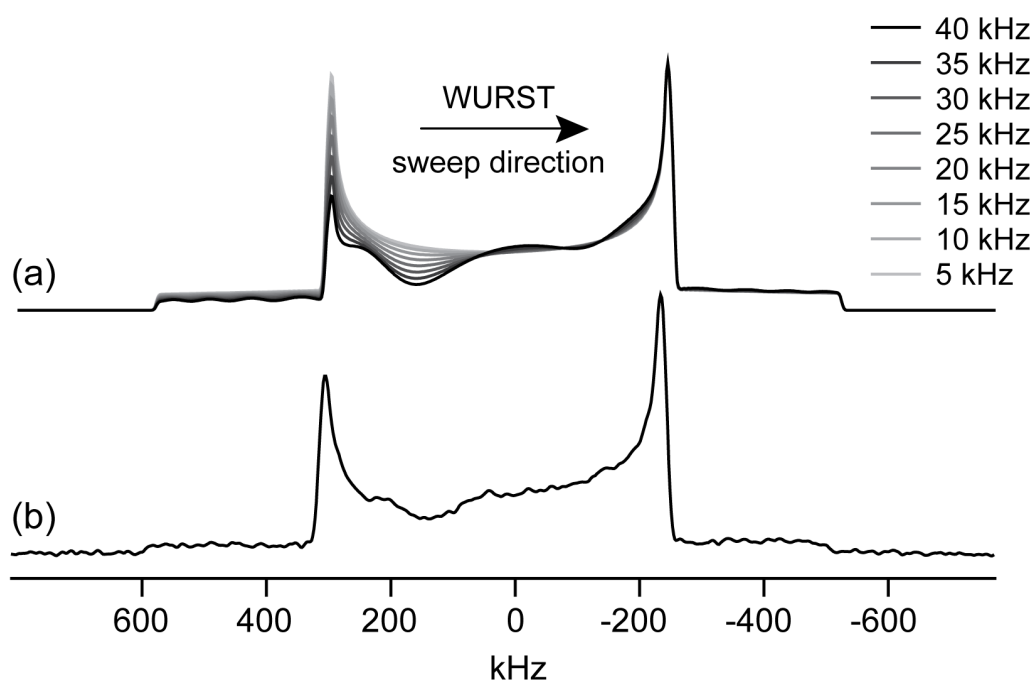


**Fig. 19.** (a) Simulated  $^{14}\text{N}$  WURST-echo powder spectra of potassium nitrate (with normalized amplitudes) with the frequency sweep direction and various RF powers as shown, (b) piecewise experimental spectrum obtained using the WURST-QCPMG pulse sequence at 9.4 T ( $\nu_1 = 30$  kHz). Adapted with permission from reference [88].

Copyright 2009 American Chemical Society.

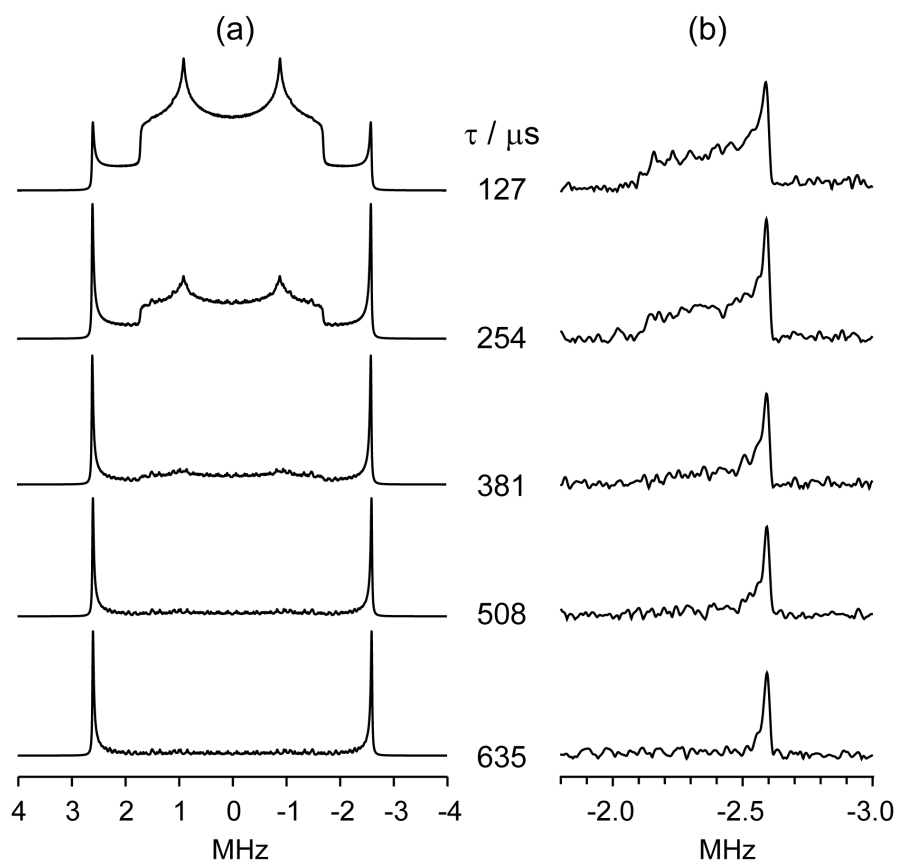


**Fig. 20.** (a) Simulated  $^{14}\text{N}$  quadrupolar-echo spectra of urea including the effects of the  $180^\circ$  flipping motion of the molecule around the carbonyl bond at a rate of  $7 \times 10^3 \text{ s}^{-1}$  and with inter-pulse delays  $\tau$  as shown. (b) Corresponding experimental spectra obtained at 21.1 T by individually processing the first five echoes from a WURST-QCPMG train.

Reproduced from reference [92] by permission of The Royal Society of Chemistry.

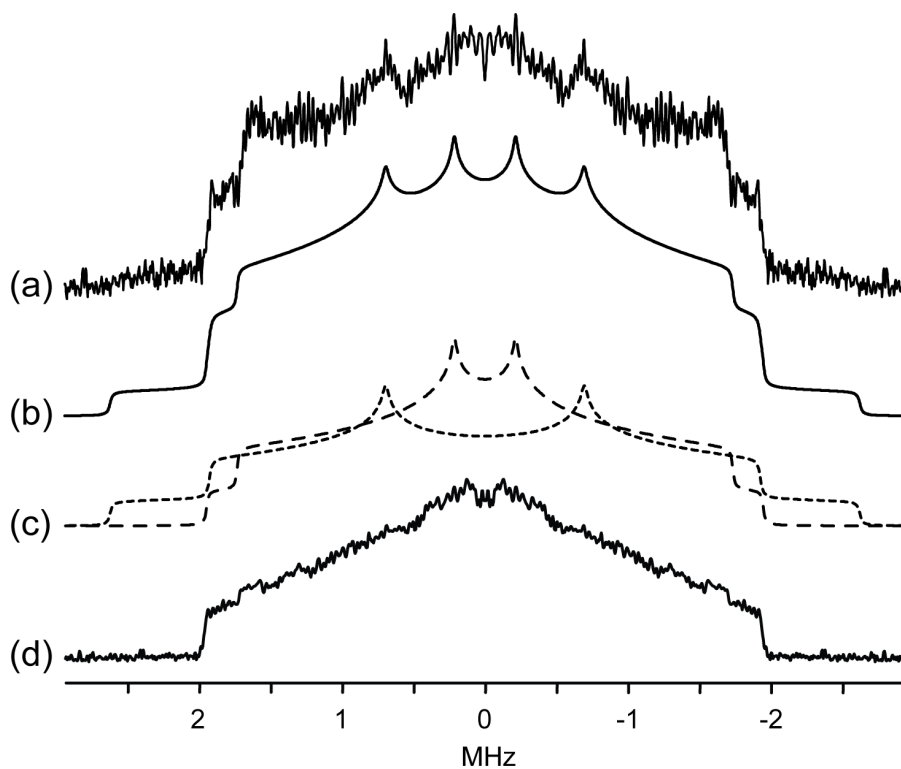


**Fig. 21.** (a)  $^{14}\text{N}$  WURST-echo spectrum obtained from melamine at 21.1 T, (b) fitted simulation with two powder patterns of equal intensity (shown in (c)) corresponding to the ring sites (dashed line,  $C_Q = 2.60$  MHz and  $\eta_Q = 0.78$ ) and amine sites (dotted line,  $C_Q = 3.50$  MHz and  $\eta_Q = 0.47$ ). (d) WURST-QCPMG spectrum. Adapted with permission from reference [94]. Copyright 2011 American Chemical Society.

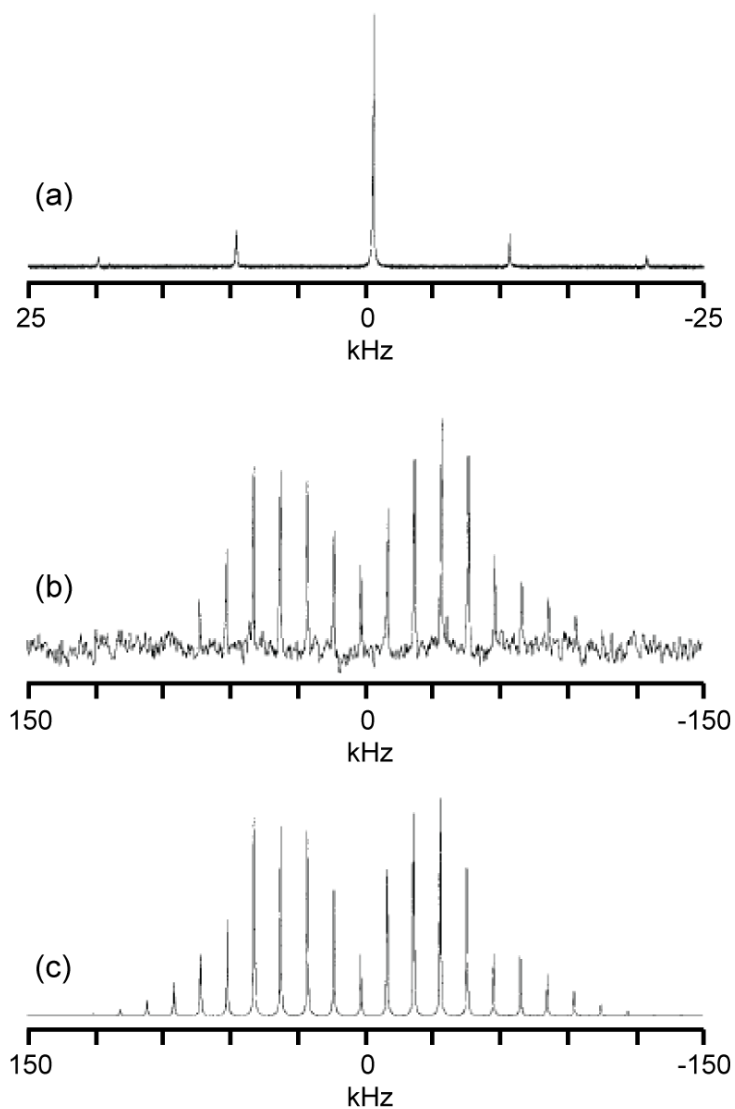


**Fig. 22.**  $^{14}\text{N}$  MAS NMR spectra of (a) cubic and (b) hexagonal boron nitride obtained at 9.4 T. (c) Simulation of the spectrum in (b) made using parameters  $\delta_{\text{iso}} = 63$  ppm,  $\Delta_{\text{CS}} = 160$  ppm,  $C_{\text{Q}} = 140$  kHz and  $\eta_{\text{Q}} = 0$ . Reproduced from reference [96]. Copyright Wiley-

VCH Verlag GmbH & Co. KGaA.

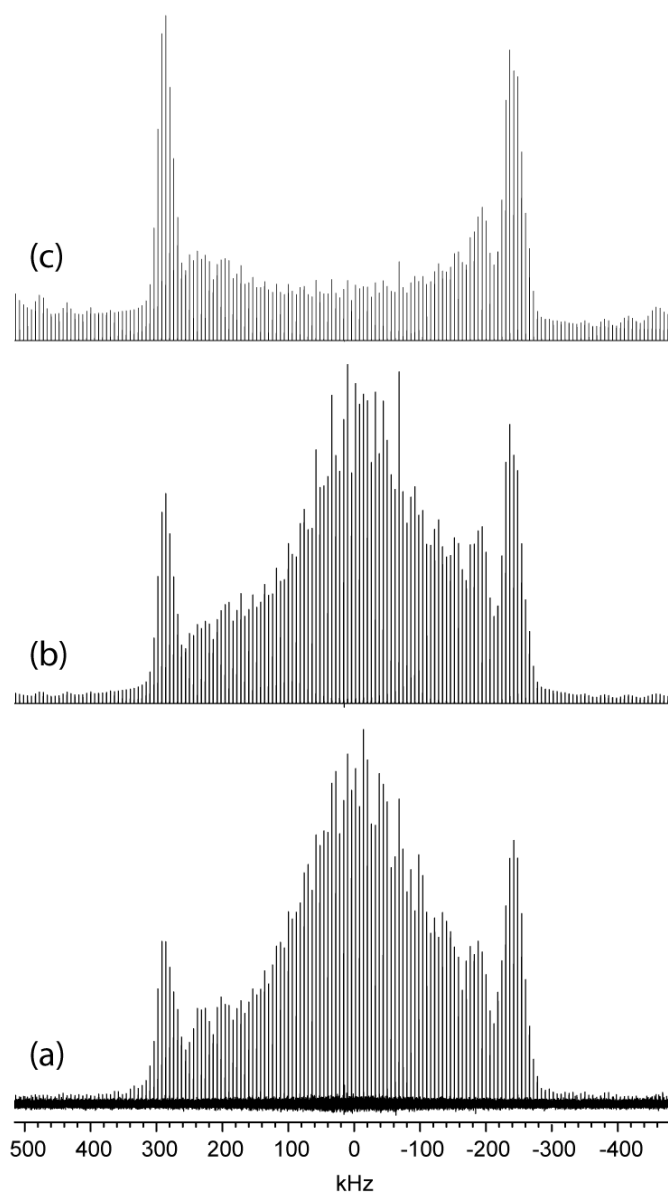


**Fig. 23.** (a)  $^{14}\text{N}$  NMR spectrum of potassium nitrate obtained at 14.1 T and 6 kHz MAS, (b) simulation taking into account experimental bandwidth limitations, and (c) simulation without experimental bandwidth limitations. Centrebands are marked with an asterisk. Reproduced with permission from reference [106]. Copyright 2001 American Chemical Society.

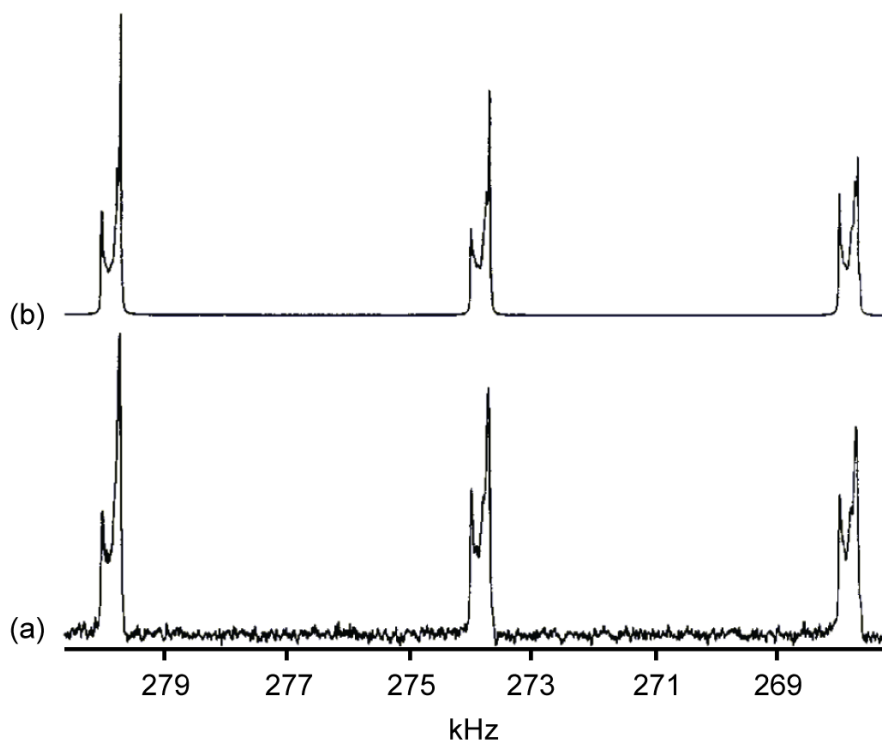


**Fig. 24.** (a) A section of the experimental  $^{14}\text{N}$  MAS NMR spectrum of potassium nitrate shown in Fig. 23, showing the spinning sideband lineshapes, and (b) a simulation taking into account the effects of the quadrupolar interaction, CSA, and various experimental factors (see text for discussion). Reproduced with permission from reference [106].

Copyright 2001 American Chemical Society.

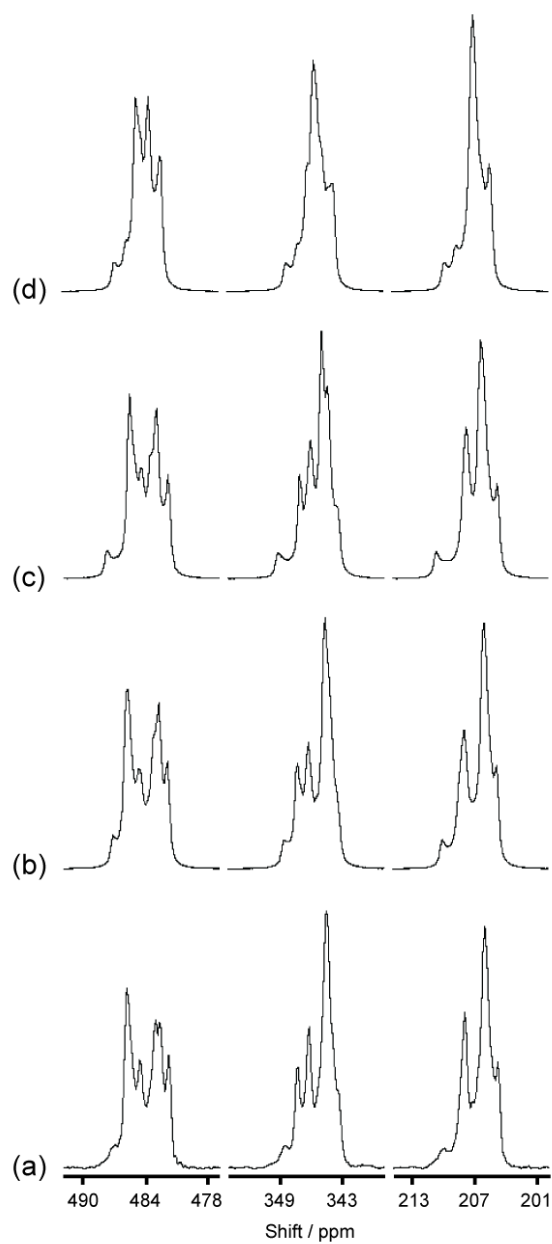


**Fig. 25.** (a) Sections of the experimental  $^{14}\text{N}$  MAS NMR spectrum of lead nitrate (14.1 T) with corresponding simulations including (b) a  $-0.002^\circ$  deviation from the magic angle and second-order quadrupolar-CSA cross terms, (c) only the second-order cross terms and (d) only the deviation from the magic angle. Reproduced with permission from reference [111]. Copyright 2003 Elsevier.

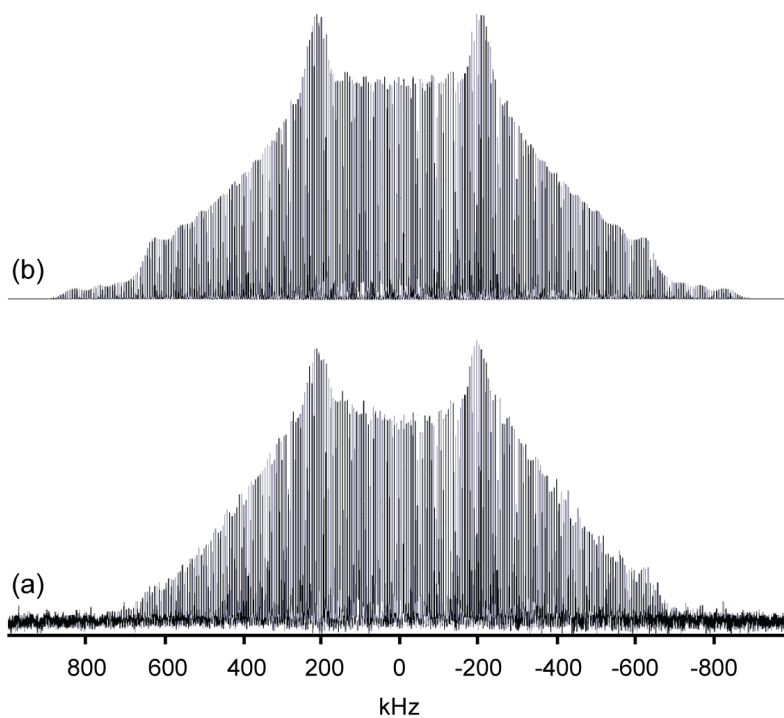


**Fig. 26.** (a) Experimental  $^{14}\text{N}$  MAS NMR spectrum of glycine, obtained at 14.1 T in 44 h with a 1  $\mu\text{s}$  excitation pulse and a MAS rate of 6 kHz, with (b) simulated spectrum.

Reproduced with permission from reference [112]. Copyright 2004 Elsevier.

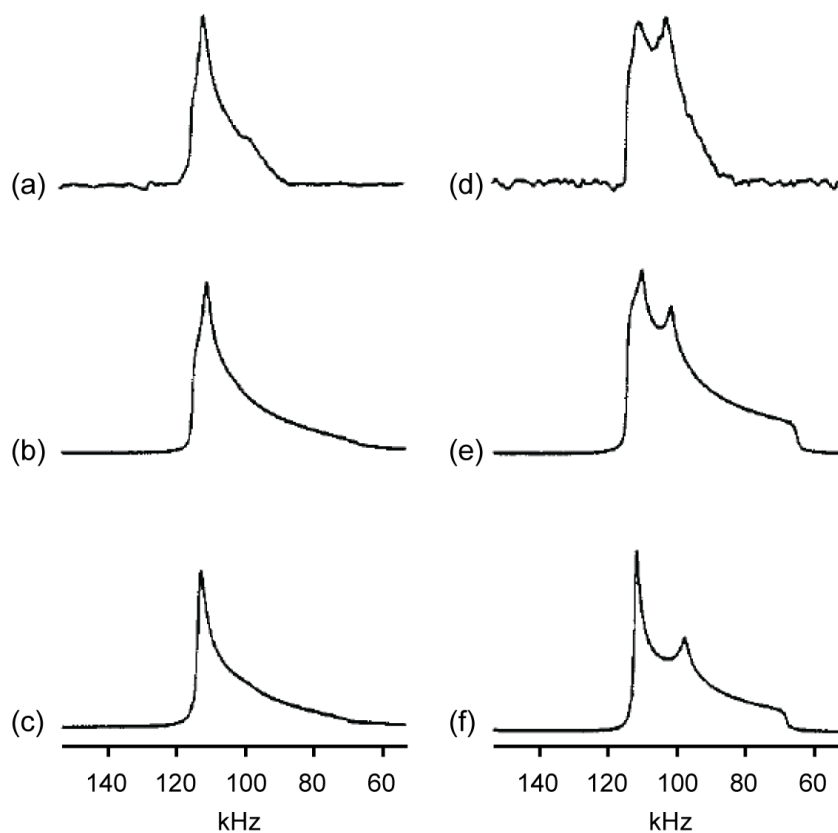


**Fig. 27.**  $^{14}\text{N}$  overtone NMR spectra obtained from a powder sample of *N*-acetylvaline at 11.7 T (*ca.* 8 hours each), with corresponding simulations, using a solenoid coil oriented (a-c) perpendicular to  $B_0$  and (d-f) parallel to  $B_0$ . Simulations (b) and (e) include the effects of both the SOQI and CSA, while (c) and (f) include just the SOQI. Reproduced with permission from reference [120]. Copyright 1986 American Chemical Society.

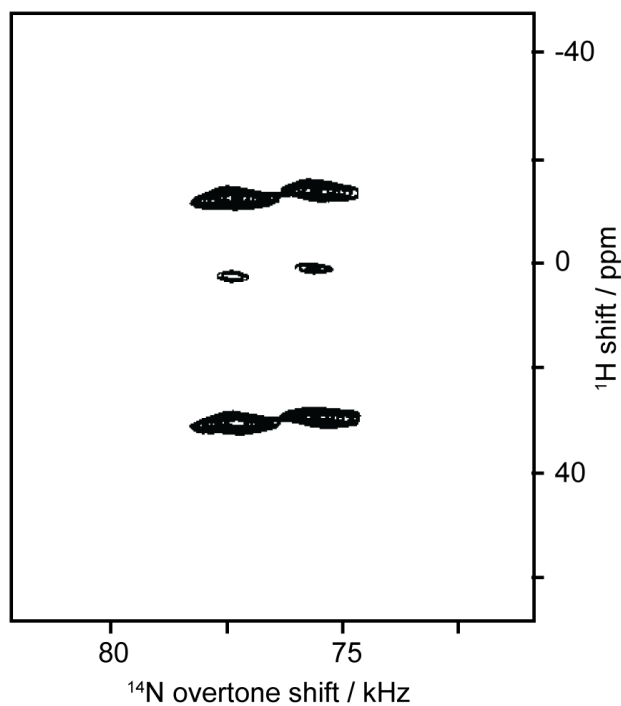


**Fig. 28.** A  $^1\text{H}$ - $^{14}\text{N}$  overtone heteronuclear correlation spectrum obtained from a single crystal of *N*-acetylvaline at 8.4 T. Asymmetric  $^1\text{H}$  triplets caused by  $^1\text{H}$ - $^{14}\text{N}$  dipolar couplings are correlated with the  $^{14}\text{N}$  overtone transition. Reproduced with permission from reference [130]. Copyright 1995 American Chemical Society.

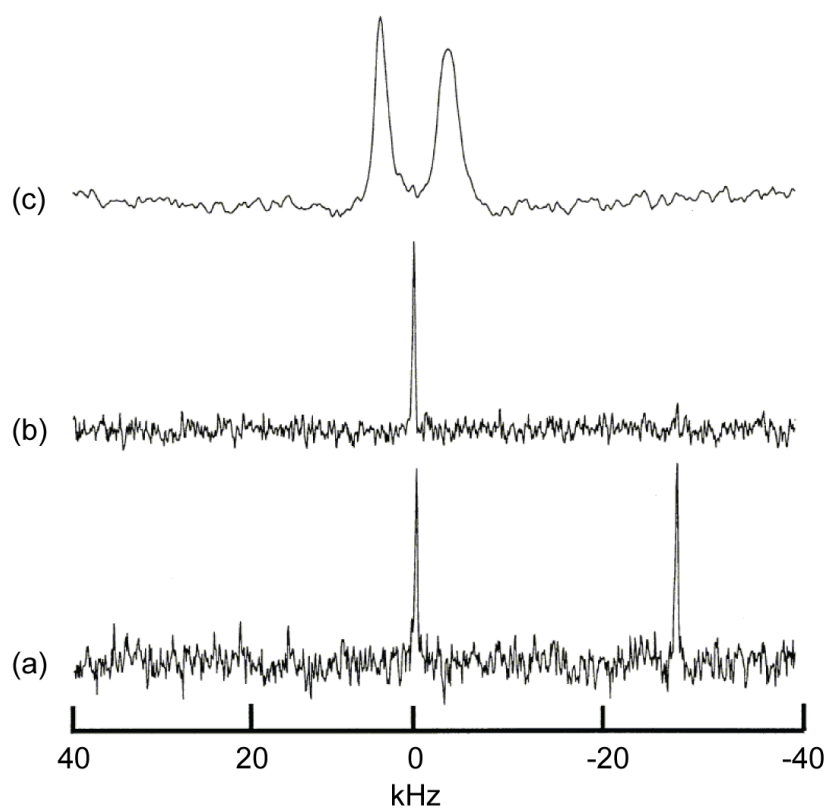


**Fig. 29.** (a)  $^{14}\text{N}$  CP overtone spectrum of a single-crystal of *N*-acetylvaline at 9.4 T with the  $^{14}\text{N}$  spin-lock frequency at the midpoint between the two resonances, (b) the same spectrum with the  $^{14}\text{N}$  spin-lock frequency moved by +10 kHz, resulting in selective cross-polarization to the resonance at 0 kHz, and (c) DIPOTSHIFT spectrum with Lee-Goldburg decoupling on the proton channel, which results in a scaled N-H dipolar coupling visible as a splitting of the  $^{14}\text{N}$  overtone resonance. Reproduced with permission from reference [134]. Copyright 1998 Elsevier.

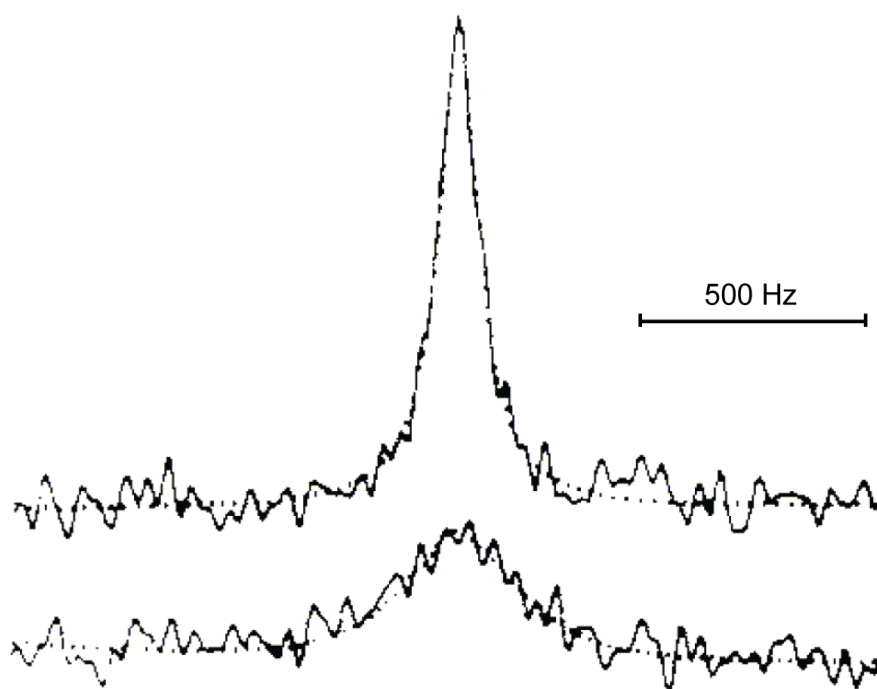


**Fig. 30.**  $^{14}\text{N}$  NMR spectra obtained at 2.4 T from sonicated dipalmitoyl phosphatidylcholine at 50°C (top) and 35°C (bottom). Reproduced with permission from reference [172]. Copyright 1980 American Chemical Society.

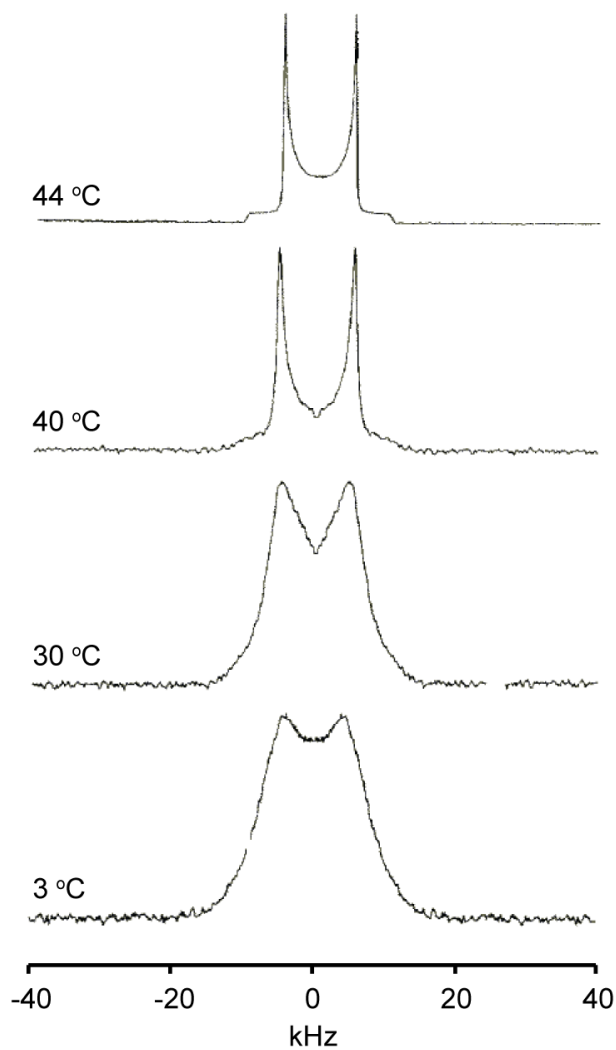


**Fig. 31.**  $^{14}\text{N}$  NMR spectra of unsonicated dipalmitoyl phosphatidylcholine at 6.3 T and at various temperatures as shown. Reproduced with permission from reference [45].

Copyright 1980 Elsevier.

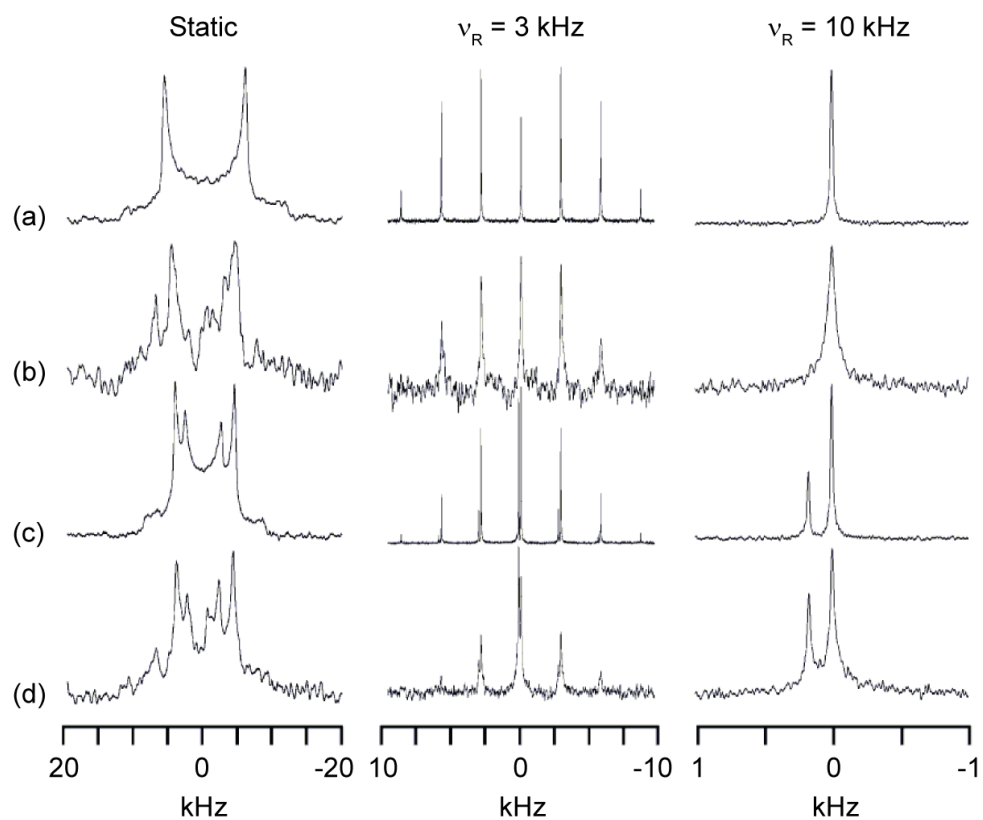


**Fig. 32.**  $^{14}\text{N}$  NMR spectra obtained at 9.4 T under static and MAS conditions from DMPC/DMPG (80/20 mol%) (a and b), and DMPC/DMPG/DDAB (60/20/20 mol%) (c and d). In (b) and (d), the amyloid- $\beta$  peptide is incorporated in a 30:1 lipid to peptide ratio. Reproduced from reference [212] by permission of the PCCP Owner Societies.